

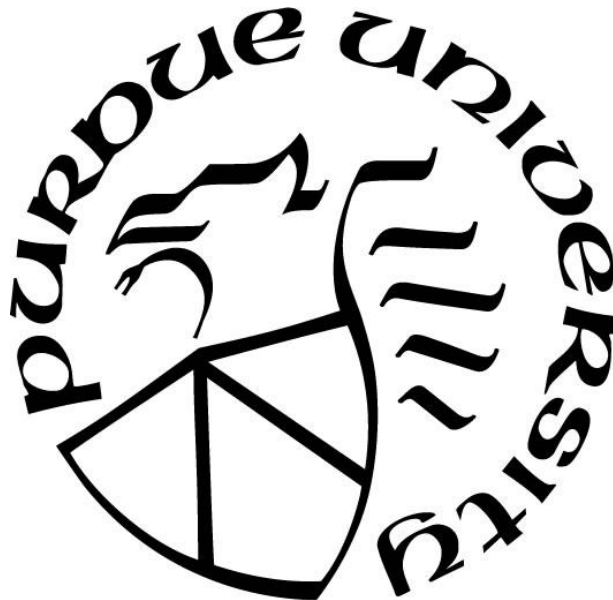
**REPRESENTATION OF DIFFERENTIAL MOLECULAR DIFFUSION BY
USING LAMINAR FLAMELET AND MODELING OF POOL FIRE BY
USING TRANSPORTED PDF METHOD**

by
Tianfang Xie

A Dissertation

*Submitted to the Faculty of Purdue University
In Partial Fulfillment of the Requirements for the degree of*

Doctor of Philosophy



School of Aeronautics and Astronautics
West Lafayette, Indiana
August 2022

**THE PURDUE UNIVERSITY GRADUATE SCHOOL
STATEMENT OF COMMITTEE APPROVAL**

Dr. Haifeng Wang, Chair
School of Aeronautics and Astronautics

Dr. Li Qiao
School of Aeronautics and Astronautics

Dr. Sally P. Bane
School of Aeronautics and Astronautics

Dr. Steven F. Son
School of Mechanical Engineering

Approved by:
Dr. Gregory A. Blaisdell

Dedicated to my respectful parents Sun, Ping, Xie, Dabiao, and my family for their silent love, endless support, and sacrifices for my growth.

ACKNOWLEDGMENTS

Words cannot express how grateful I am to my advisor and committee chair, Prof. Haifeng Wang. I am especially grateful for his patience and inculcation. The academic experience he shared has greatly enhanced my ability to work independently, allowing me to see the big picture and keep moving forward at all times. He has always inspired me to think critically and creatively about research. During the writing of my dissertation, I also received a lot of guidance from him, which benefited me a lot.

My doctoral studies would not have been possible without my defense committee, and I am very grateful for Prof. Li Qiao, Prof. Sally Bane, and Prof. Steven Son, who generously offered their insightful advice and detailed comments on my work. In addition, this dissertation would not have been possible without the support of ItAP Research Computing (RCAC) for providing the computational resources for my research.

I am also grateful to my laboratory partners at Purdue Computational Energy and Propulsion Lab (CEPL) for their daily discussions, frequent assistance, and moral supports. I truly cherished and enjoyed the time spent with Dr. Chao Han, Dr. Tejas Pant, Dr. Pei Zhang, Jie Tao, Utsav Jain, Zehao Lu, and Nianju Gu. I would also like to thank all my dear friends for their companionship and support in my life. During my doctoral studies, I have received much valuable help from Mengmeng Wang, Hao Lyu, Yanwen Chen, Albert Chang, Banghua Zhao, Puyuan Wu, Binghong Miao, Dr. Wenyan Du, and Xuesong Wang.

I am especially grateful to my best friends Xiaoka Xiang, Ang Li, and Dr. Han Luo, who have been an endless source of inspiration and encouragement. Their optimistic attitudes toward life and hard-working spirits gave me tremendous motivation, and their excellence is like a light that illuminates my way forward. They were my emotional support during my doctoral studies, and I cherish the time I spent with them.

Finally, I would like to express my deepest gratitude to my parents and family. Their endless love and unending support have made me who I am today, they have made it possible for me to receive an education at Purdue University, and there are no words to express my love for them.

TABLE OF CONTENTS

LIST OF TABLES	7
LIST OF FIGURES	8
NOMENCLATURE	12
ABBREVIATIONS	15
ABSTRACT.....	16
1. INTRODUCTION.....	1
1.1 Background of combustion research.....	1
1.2 Turbulent diffusion combustion.....	2
1.3 Models of turbulent combustion.....	3
1.4 Differential molecular diffusion	5
1.5 Flame instability and extinction limits.....	7
1.6 Open questions and challenges in turbulent combustion modeling.....	9
1.7 Objectives and outline of the dissertation.....	11
2. REPRESENTATIVITY OF DMD BY USING LAMINAR FLAMELET MODEL.....	13
2.1 Concept and governing equations of laminar flamelet model	13
2.2 Flamelet model implementations and simulations.....	15
2.2.1 Flamelet modeling of transitional diffusion flame	15
2.2.2 Quantitative presentation of DMD effect in the transitional diffusion flame.....	17
2.3 Representation of DMD by using two different conceptual burners	20
2.3.1 Laminar flamelet based on opposed jet burner.....	21
2.3.2 Laminar flamelet based on Tsuji burner.....	24
2.4 Comparison of the opposed jet burner and the Tsuji burner.....	26
2.4.1 The similarity of opposed jet and Tsuji burners	27
2.4.2 Difference between opposed jet and Tsuji burners.....	29
Non-reacting cases	29
Reacting cases of Tsuji burner	33
2.5 Analysis and parametric studies of the opposed jet mixing layer.....	36
2.5.1 Unconstrained opposed jet mixing layer	37
2.5.2 Constrained opposed jet mixing layer	40
2.6 Conclusions.....	44

3.	IMPLICATION TO FLAMLELET MODELING OF DMD	46
3.1	Pure mixing in the laminar jet flow	48
3.2	Pure mixing in the turbulent jet flow	50
3.3	Turbulent jet non-premixed flame	52
3.4	Conclusions.....	54
4.	TRANSPORTED PDF MODELING OF A POOL FIRE.....	56
4.1	Transported PDF model.....	56
4.2	Mixing models implemented in PDF.....	59
4.2.1	Interaction by Exchange with the Mean (IEM) model	60
4.2.2	Modified Curl mixing model.....	60
4.2.3	Euclidean Minimum Spanning Tree (EMST) model.....	61
4.3	NIST Fire Dynamics Simulator (FDS) code.....	62
4.4	Coupling method between FDS and HPDF	63
4.5	Introduction of UMD line burner.....	65
4.6	Conclusions.....	68
5.	INVESTIGATION OF UMD FIRE BY USING FDS AND HPDF	69
5.1	FDS results of UMD flame simulations.....	69
5.2	Validation of CH ₄ /Air flame simulation using the coupled FDS-HPDF model	73
5.3	Investigation of combustion efficiency and fire extinction limits by using coupled FDS-HPDF model	79
5.3.1	Calculation of heat release rate.....	79
5.3.2	Investigation of fire extinction limits prediction	81
5.4	Flame regime identification by using flame index	85
5.5	Summary	92
6.	CONCLUSION AND FUTURE WORK	93
	REFERENCES	96

LIST OF TABLES

Table 5.1. Lowest C_ϕ value to yield burning case for CH₄ flames in undiluted ambient air. 84

LIST OF FIGURES

Figure 1.1. Estimated global fossil energy share of total final energy consumption. The large gray-colored cube represents the usage percentage of fossil fuels. The red cube is the nuclear energy share. The brown cube shows the share of traditional biomass. The yellow cube corresponds to modern renewable energy. 1

Figure 2.1. Experimental setup of the hydrogen-air transitional diffusion flame; (a) camera-taken picture of the experimental facility captured from Robert’s paper [42], (b) schematic diagram of the experimental facility. 16

Figure 2.2. Front views show the fluctuations of the luminous zone in the hydrogen-air transitional diffusion flame captured from Robert’s paper [42] (up figures) and the corresponding simulation results (bottom contour plots). 17

Figure 2.3. The time-averaged temperatures at different axial locations ($x/D = 1, 2, 4, 5, 8,$ and 16) of the hydrogen-air transitional diffusion flame with (red line) and without (blue line) considering DMD effects. 18

Figure 2.4. The experimental data (red dots) and the calculated results (blue line) consider the DMD effects of the average temperature at different axial locations ($x/D = 1, 2, 4, 5, 8,$ and 16) of the hydrogen-air transitional diffusion flame. 19

Figure 2.5. Schematics of the opposed jet burner (left) and the Tsuji burner (right) and their computational domains. The diameters of the fuel and oxidizer jets for the opposed jet burner are all set as D_o , the distance between the two jet exits is H_o . The porous cylinder of the Tsuji burner has a diameter of D_T 21

Figure 2.6. Illustration of the profiles of mass fractions of fuel Y_{fuel} , oxidizer Y_{oxid} , and products Y_{prod} inside an opposed jet flame with inlet diffusion at both jet inlets (left) and without inlet diffusion (right). 23

Figure 2.7. Comparison of the profiles of temperature T , species mass fractions Y_{H_2} , Y_{CO_2} , Y_{OH} , scalar dissipation rate χ (based on ξ), and the DMD parameter z against the mixture fraction ξ in the laminar non-premixed flames established in the opposed jet burner (solid lines) and the Tsuji burner (dashed lines) at the same nominal strain rate $a_s = 80 \text{ s}^{-1}$ 28

Figure 2.8. Comparison of the profiles of z against the mixture fraction ξ in the laminar non-reacting Tsuji burner (first row) and non-reacting opposed jet burner (second row). The left plots show the comparison of the results with the experimental data under different strain rates a_s , and the right plots show the results under the same strain rate $= 80 \text{ s}^{-1}$ but with different R 31

Figure 2.9. Variation of the predicted $\xi_C|_{z=0}$ against the velocity ratio R in non-reacting opposed jet burners and Tsuji burners for two different strain rates $a_s = 40 \text{ s}^{-1}$ and 80 s^{-1} 33

Figure 2.10. Comparison of the profiles of z against the mixture fraction ξ in the reacting Tsuji burner (first row) and reacting opposed jet burner (second row). The left plots show the results under different strain rates a_s , and the right plots show the results under the same strain rate $a_s = 80 \text{ s}^{-1}$ but with different R	34
Figure 2.11. Variation of the predicted $\xi _{z=0}$ against the velocity ratio R in reacting opposed jet burners and Tsuji burners for two different strain rates $a_s = 40 \text{ s}^{-1}$ and 80 s^{-1}	36
Figure 2.12. An idealized laminar opposed jet mixing layer (left: infinitely distance of the two sources of jets; right: finite distance between the two sources of jets).	37
Figure 2.13. The profiles of z against ξ in the idealized laminar opposed jet mixing layer with $a_s = 40 \text{ s}^{-1}$; (a) unconstrained opposed jet mixing layer with an infinite distance between the two sources of jets (equivalent to the constrained opposed jet mixing layer with $\theta = \infty$), (b) constrained opposed jet mixing layer with a finite distance between the two sources of jets with $\theta = 5$, (c) constrained opposed jet mixing layer with a finite distance between the two sources of jets with $\theta = 1$	39
Figure 2.14. The variation of $\xi _{z=0}$ against R in the constrained opposed jet mixing layer with $\theta = 1$ and with different strain rates, $a_s = 40 \text{ s}^{-1}$, 80 s^{-1} , 120 s^{-1} , and 160 s^{-1}	43
Figure 2.15. the profiles of $\xi _{z=0}$ against R in the constrained opposed jet mixing layer with the different values of θ under the same strain rate $a_s = 40 \text{ s}^{-1}$	44
Figure 3.1. Schematic diagram of a jet flow or jet flame configuration.	47
Figure 3.2. Schematic diagram of H ₂ mass fractions distribution in the calculation region.	48
Figure 3.3. Comparison of the profiles of z against ξ at $x/D_j = 10$ in a laminar jet flow under different Reynolds numbers $\text{Re} = 2 \times 10^2$, 4×10^2 , 6×10^2 , and 8×10^2 with the laminar flamelet results obtained in the non-reacting opposed jet burner and the Tsuji burner with the same strain rate $a_s = 80 \text{ s}^{-1}$ and different ranges of R , $R \in [10^{-2}, 10^3]$ for the Tsuji burner and $R \in [0.2, 6.5]$ for the opposed jet burner. The circles are the simulation results in the laminar jet flow, and the differently shaded regions cover the considered laminar flamelet solutions from the different burners.	49
Figure 3.4. Comparison of the profiles of z against ξ at $x/D_j = 30$ in a turbulent jet flow [10] under different Reynolds numbers $\text{Re} = 1 \times 10^3$, 4×10^3 , 16×10^3 , and 64×10^3 with the laminar flamelet results obtained in the non-reacting opposed jet burner and the Tsuji burner with the same strain rate $a_s = 80 \text{ s}^{-1}$ and different ranges of R , $R \in [10^{-2}, 10^3]$ for the Tsuji burner and $R \in [0.2, 6.5]$ for the opposed jet burner. The circles are the experimental data in the turbulent jet flow [50], and the differently shaded regions cover the considered laminar flamelet solutions from the different burners.	51

Figure 3.5. Comparison of the profiles of z against ξ at $x/D_j = 30$ in a turbulent jet flame [11] under different Reynolds numbers $Re = 2 \times 10^3, 4 \times 10^3, 8 \times 10^3,$ and 16×10^3 with the laminar flamelet results obtained in the reacting opposed jet burner and the Tsuji burner with the same strain rate $a_s = 80 \text{ s}^{-1}$ and different ranges of $R, R \in [5 \times 10^{-2}, 10^3]$ for the Tsuji burner and $R \in [0.2, 4]$ for the opposed jet burner. The circles are the experimental data in the turbulent jet flame [10], and the differently shaded regions cover the considered steady laminar flamelet solutions from the different burners as well as the transient flamelet solutions in the Tsuji burner. 54

Figure 4.1. A plan-view schematic diagram of the experimental apparatus shows the burner’s size and the fuel and oxidizer ports..... 67

Figure 5.1. Schematic diagram of the numerical configuration; The coordinate of the calculation domain and its size are shown on the left plot. The grids of the inner refinement mesh and outside coarse mesh are shown on the right plot..... 71

Figure 5.2. Camera-taken simultaneous photos from the front and side view of the methane flame using the diluted air with 18% oxygen are captured from White’s paper [87] and shown on the left side. Simultaneous temperature contour plots of CH4 flame from the simulation are shown on the right side; the temperature range is 300 K to 2200 K..... 72

Figure 5.3. Calculated (blue line) and measured experimental data of the time-averaged temperature (squared dots) and O₂ mole fraction (circled dots) at different z locations above the fuel port; the oxidizer is the diluted air with 18% oxygen. The left plots are from $z = 12.5$ cm location, the right plots are at $z = 25.0$ cm..... 73

Figure 5.4. A schematic diagram of the simulation domain, the coordinate and boundary settings are shown on the left side; A plan-view of the fuel and oxidizer port surface is shown on the right side. 74

Figure 5.5. Schematic diagram of the numerical configuration; The coordinate of the calculation domain and its size are shown on the left plot. The grids of the mesh are shown on the right-hand side plot..... 75

Figure 5.6. Calculated and measured experimental data of the time-averaged temperature (squared dots) and O₂ mole fraction (circled dots) above the fuel port; the oxidizer is the diluted air with 18% oxygen. The solid blue line represents a 2.5 mm grid, the black dash-dotted line represents a 3.75 mm grid, and the red dashed line represents a 5 mm grid. 76

Figure 5.7. Calculated (blue line) and measured experimental data of the time-averaged temperature (squared dots) and O₂ mole fraction (circled dots) at different z locations above the fuel port; the oxidizer is the diluted air with 18% oxygen. The left plots are from $z = 12.5$ cm location, the right plots are at $z = 25.0$ cm..... 77

Figure 5.8. Camera-taken instantaneous distribution side-view of the experimental captured from White’s paper [54] and temperature contour plots in the simulation’s x - z plane. The camera-taken photo is on the left side, and a series of temperature contour plots generated by the coupled model are shown on the right side. 78

Figure 5.9. Calculated and measured experimental data of the combustion efficiency η_{comb} versus different oxygen levels $X_{O_2}^{ox}$ for the non-anchored flame; the oxidizer is the diluted air with oxygen from 10% to 21% in mole fraction. The black and blue lines are EMST model with C_ϕ equals 3.0 and 6.0; the purple and yellow lines are IEM model with C_ϕ equals 10 and 40; the green line is the Modified Curl Model with C_ϕ equals 15..... 82

Figure 5.10. Calculated and measured experimental data of the time-averaged temperature (squared dots) and O₂ mole fraction (circled dots) above the fuel port; the oxidizer is the diluted air with 18% oxygen. The solid blue line represents the EMST model, the solid red line represents the IEM model, and the solid green line represents the modified Cur model. 85

Figure 5.11. Schematic diagram of the flame index. The red solid vector represents the oxidizer gradient $\nabla \tilde{Y}_O$; the solid purple vector is the fuel gradient $\nabla \tilde{Y}_F$. The upper left plot shows the non-premixed mixing, the upper right plot demonstrates the premixed mixing, and the lower plot shows the partially premixed mixing phenomenon. 87

Figure 5.12. Simultaneous contour plot of CH₄ flame from the simulation; (upper left) temperature, (upper right) O₂ mass fraction, (lower left) CH₄ mass fraction, (lower right) flame index. 89

Figure 5.13. Interesting zone of flame index contour plot..... 90

Figure 5.14. Contour plot of the interesting zone; (upper) mass fraction of CH₄ and the yellow line fuel gradient, (middle) mass fraction of O₂ and the white line oxidizer gradient, (lower) flame index, and both gradients. 91

NOMENCLATURE

a_p	decay rate of the variance
a_s	strain rate
B_ν	edge coefficient of the ν th edge in the spanning-tree
C_ϕ	model constant for the mixing model
C_p	specific heat capacity
D_α	molecular diffusivity of the species α
D_ξ	molecular diffusivity of mixture fraction
D_J	jet diameter
f	probability density function
F_i	combination of advective and baroclinic terms
H_s	sensible enthalpy
h_{comb}	specific enthalpy of the combustion
$h_{s,\alpha}$	specific enthalpy of species α
$\Delta h_{f,k}^\circ$	standard enthalpy of formation of the k th species
k	thermal conductivity
Le	Lewis number
M	mixing term
\dot{m}_α'''	rate of mass production of species α per unit volume
$\dot{m}_{b,\alpha}'''$	rate of mass production of species α generated by evaporation of droplets per unit volume
P	pressure
\dot{Q}	heat release rate
$\dot{\mathbf{q}}''$	vector of heat flux
\dot{q}_r''	radiative heat flux

\dot{q}'''	heat release rate per unit volume
R	velocity ratio
Sc_t	turbulent Schmidt number
S_α	chemical reaction source term of species α
$S_\alpha(\phi)$	scalar source term generated by reaction
T	Temperature
T_k	characteristic thickness of the mixing layer
u	velocity in the axial direction
\mathbf{u}	velocity vector
U_C	co-flow air speed
U_J	bulk jet velocity
V_F	bulk fuel inflow velocity
V_O	bulk oxidizer inflow velocity
\mathbf{W}	standard isotropic Wiener process
W_α	molecular weight of species α
x	axial direction distance
X_α	mole fraction of species α
$X_{\alpha,0}$	initial mole fraction of species α
Y_α	mass fraction of species α
$Y_{\alpha,\text{FDS}}$	mass fraction of species α gets from FDS code
$Y_{\alpha,\text{PDF}}$	mass fraction of species α gets from transported PDF model
Z	differential diffusion variable
Z_α	difference between the mixture fraction ξ_α obtained from elements and the mixture fraction ξ in the flamelet model
α	thermal diffusivity
β	threshold value
χ	scalar dissipation rate

ϕ	scalar values
Γ	molecular diffusivity
Γ_t	turbulent eddy diffusivity
γ	specific heat ratio equals to 1.4
ν	kinematic viscosity
$\nu_{\alpha,i}$	stoichiometric coefficient for the α th species
δ	Kronecker delta
δ_t	time step size
η	phase space variables of mixture fraction
τ	time average window
τ_{mix}	characteristic mixing time
μ_t	turbulent viscosity
$\zeta(t)$	unmixed fraction of the mass
θ	phase space variables to stoichiometric scalar dissipation rate
ρ	mixture density
Ω	mixing frequency
ξ	mixture fraction
ξ_k	mixture fraction obtained from the elements
$\nabla \tilde{Y}_O$	gradient of mass fractions of oxidizer
$\nabla \tilde{Y}_F$	gradient of mass fractions of fuel
ξ_{st}	stoichiometric condition
erf	error function
$erfc^{-1}$	inverse complementary error function

ABBREVIATIONS

CFD	Computational Fluid Dynamics
CMC	Conditional Moment Closure
DMD	Differential Molecular Diffusion
DNS	Direct Numerical Simulation
EMST	Euclidean Minimum Spanning Trees
FDS	Fire Dynamics Simulator
FPV	Flamelet Progress Variable
FI	Flame Index
IEM	Interaction by Exchange with the Mean
LES	Large Eddy Simulation
MCurl	Modified Curl
PDF	Probability Density Function
RANS	Reynolds Averaged Navier-Stokes
SFM	Steady Flamelet Model

ABSTRACT

A combustion simulation involves various physiochemical processes, such as molecular and turbulent diffusion, smoke and soot formation, thermal radiation, chemical reaction mechanisms, and kinetics. In the last decade, computational fluid dynamics (CFD) has been increasingly used in combustion modeling. It is critically important to improve and enhance the predictive capabilities of combustion models. This work presents an analysis of two types of diffusion flames: the momentum-dominant jet flames and buoyancy-controlled pool fires. The gap between the existing knowledge of differential molecular diffusion in turbulent high momentum jet flow and the practical applications has been reduced. The importance of mixing modeling in pool fire simulations has been revealed, and enhancement for predicting fire extinction limits has been proposed.

Modeling differential molecular diffusion in turbulent non-premixed combustion remains a great challenge for flamelet models. The laminar flamelet is a key component of a flamelet model for turbulent combustion. One significant challenge that has not been well addressed is the representativity of laminar flamelet for the characteristics of differential molecular diffusion in turbulent combustion problems. Laminar flamelet is generated typically based on two conceptual burner configurations, the opposed jet burner, and the Tsuji burner. They are commonly considered equivalent when dealing with the description of laminar flamelet structures. A difference between them is revealed in this work for the first time when they are used to represent differential molecular diffusion. The traditionally opposed jet burner yields an almost fixed equal diffusion location in the mixture fraction space for the transport of different elements. The Tsuji burner can produce a continuous variation of the equal diffusion location in the mixture fraction space with a slight extension. This variation of the equal diffusion location is shown to be an essential characteristic of turbulent non-premixed combustion, as demonstrated in a laminar jet mixing layer problem, a turbulent jet mixing layer problem, and a turbulent jet non-premixed flame. The Tsuji burner is thus potentially a more suitable choice than the opposed jet burner for laminar flamelet generation that can be consequently used in flamelet modeling of differential molecular diffusion for turbulent non-premixed combustion.

Capturing fire extinction limits in simulations is essential for developing predictive capabilities for fire. In this work, the combined large-eddy simulation (LES) and transported

probability density function (PDF) methods are assessed for the predictions of fire extinction. The University of Maryland line burner is adopted as a validation test case. The NIST Fire Dynamics Simulator (FDS) code for LES is combined with an in-house PDF code called HPDF for the fire simulations. The simulation results were verified by using the available experimental data. The combustion efficiency under the different oxygen depletion levels in the oxidizer is analyzed. Fire extinction occurs when the oxygen depletion level reduces to a certain level. The model's capability to capture this extinction limit is assessed by using the experimental data. Different mixing models and model parameters are examined. It is found that the fire extinction limit is very sensitive to the different mixing models and mixing parameters. The level of sensitivity is higher than in momentum-driven turbulent flames, which suggests the importance of mixing modeling in fire simulations. The existing mixing models need further enhancement for predicting fire extinction.

1. INTRODUCTION

1.1 Background of combustion research

Combustion is a series of chemical reactions between the fuel and oxidizer; this procedure will always accompany luminous and heat generation. The usage of the combustion of humankind can be traced back tens of thousands of years ago. The development level of combustion technology can reveal humanity's ability to conquer nature and human society's development level. Combustion is a physical and chemical phenomenon that involves complex flow phenomena, chemical reactions, and heat and mass transfer; the basic combustion research from physical and chemical aspects can help people to get a better understanding of the details of these disciplines from the macro and micro perspective, the development of practical combustion technology has become an essential part of flame research and engineering practices.

As shown in Figure 1.1, burning fossil energy provides more than 75 percent of the world's energy supplement today [1]. There has been a severe conflict between the rapid fossil energy consumption and limited reserves. In the next several decades, using the combustion of fossil energy to provide power and heat sources will not change significantly. Therefore, the most crucial energy research directions are optimizing existing burners, developing new combustion technologies, and improving combustion efficiency.

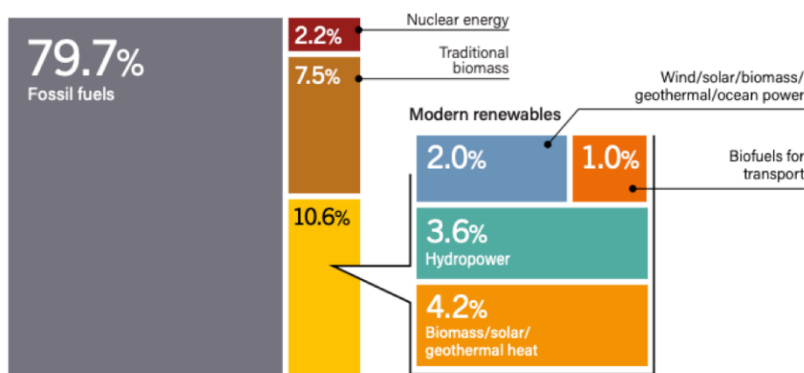


Figure 1.1. Estimated global fossil energy share of total final energy consumption. The large gray-colored cube represents the usage percentage of fossil fuels. The red cube is the nuclear energy share. The brown cube shows the share of traditional biomass. The yellow cube corresponds to modern renewable energy.

Besides, in the aviation and aerospace fields, the development of new generation aviation airplanes and the development of Hypersonic aircraft are dependent on core issues such as the unique design of aircraft, the aircraft's safe operation, and the development of advanced aviation fuel. They are all inseparable from improving essential combustion research topics such as fuel pyrolysis, low-temperature oxidation, high-temperature oxidation, and combustion numerical simulation.

In summary, pursuing more energy-efficient and less polluting fossil combustion methods or searching for more advanced and efficient chemical propulsion methods has inspired a continuous search for combustion physics. Various experiments and simulation models continue to advance our understanding of actual combustion processes. The current combustion research focuses on very complicated problems, and there is much development in modeling, simulation, and diagnostic technologies. However, combustion modeling is still inadequate; most models are highly simplified and cannot consider or capture detailed physics such as differential molecular diffusion. This work aims to reduce the gap between turbulent combustion modeling and actual physics. Section 1.2 will briefly introduce two different types of diffusion combustion that have been investigated in this work.

1.2 Turbulent diffusion combustion

Turbulent diffusion flames are common in industrial production and everyday life and are widely used in gasoline/diesel engines, rocket engines, gas turbines, industrial boilers, refineries, or oilfield flares. In the application of turbulent diffusion flame, the essential attributes are combustion efficiency, flame stability, flame extinguishing limit, flame heat release, pollutant emission, etc. Typically, there are two major types of turbulent diffusion combustion: momentum-dominant jet flames and buoyancy-controlled pool fires [2].

A jet flame is a particular type of flame with high-speed fuel. It occurs when high velocity, high-pressure combustible gas is released outward through a tiny opening in a pipe or valve. Typically, the inside pressure, the size or shape of the port, and the gas's molecular weight determine the ignited gas's mass flow rate. The turbulent jet flame is momentum dominated and has a cylindrical form [3]. At very low velocities, the jet flame is laminar, and the height of the laminar jet flame will increase as the jet speed increases. When the speed increases, the jet will change to the transitional stage. The laminar flame gradually changes to turbulence. The turbulence

zone starts to appear at the top of the flame and extends towards the burner nozzle as the speed increases. In the turbulent state, the flame height decreases as the flow rate increases until it reaches a constant value, at which point the flame is fully turbulent.

The pool fire is another kind of low-strain, buoyancy-controlled diffusion flame. Pool fires are common when igniting an accumulation of liquid on the ground, water, or other flammable liquids [4]. The pool fire can also be triggered by a collection of flammable gas or combustible solids [5]. The heat of the flames provides the evaporation of liquid or gas and stabilizes the burning fire above the horizontal pool. Three different zones exist in a pool fire: the continuous flame zone, the intermittent flame zone, and the plume zone [6]. The continuous flame zone locates above the combustion pool, the temperature in this region remains constant, and the flame is continuously visible. The intermittent flame zone is above the continuous flame zone, and intermittent flame pockets exist. The temperature in this zone gradually decreases as it moves away from the combustion pool. The flame becomes invisible in the plume zone, and the temperature drops continuously.

In summary, the situation of the pool fire is fundamentally different from the jet reaction flame. The jet reaction flame has a strong momentum of fuel and oxidizer flows, but buoyancy generated by the high-temperature region drives the flow field of the pool fire. The relatively low velocity of injected fuel and oxidizer causes much lower scalar dissipation rates and mixing rates; different mixing models and parameters must be considered for these two different diffusion combustions. Section 1.3 will introduce several turbulent combustion models used for turbulence predictions.

1.3 Models of turbulent combustion

The predictions of turbulence are essential to the modeling of turbulence combustion. The priority is to get an accurate model to predict turbulence evolution while generating an accurate model of turbulent combustion. There are three mainly used models to predict turbulence performance: the Reynolds averaged Navier-Stokes (RANS) model, the large-eddy simulations (LES) model, and the direct numerical simulations (DNS) model.

The DNS [7] model is relatively simple; it numerically solves the Navier–Stokes equations for the computational domain. The model resolves turbulence from the smallest dissipative scale (Kolmogorov scale). The spatial scales of turbulence will be solved using refinement mesh. The

temporal scales will also be resolved, and no turbulence model will be used. The DNS model is a handy tool in basic research on turbulence and turbulence model development. The only practical problem with this model is the high computational cost.

The RANS model uses the time-averaged values of variables for the steady-state or dynamic problems. This model cannot reveal the detailed physics in turbulent problems, but it is widely used in industrial problems because of the lower computational cost.

The LES model filters the Navier-Stokes equations for large-scale vortices; it neglects the small length scales to reduce computational costs. However, it can get detailed information about the time-dependent dynamics. It is a time and spatial averaging turbulence model between the DNS and RANS models.

After solving the predictions of turbulence performance, two basic combustion modeling strategies can be employed for dealing with turbulence combustion; the first method is to solve the transport equations of conserved scalars. The laminar flamelet model can be used during this process to get species mass fractions. The second method is to use the probability density function (PDF) model.

Forman A. Williams introduced the laminar flamelet model's basic ideas in a paper published in 1975 [8], then Norbert Peters provided detailed theoretical theories on this model in the 1980s [9]. The basic idea of this model is that the turbulent flame can be represented by using the one-dimensional non-premixed laminar flamelets. The turbulent flame's reactions can be seen as happening in a thin layer; the turbulence cannot cause much affection for them. The flamelets in the turbulent diffusion flame are commonly represented using counterflow diffusion flames. These counterflow diffusion flames will be calculated under different strain rates and scalar dissipation rates. The results obtained from the opposed diffusion flames are integrated using a presumed PDF function, and a look-up table is generated for the turbulent diffusion flame calculations. Two kinds of flamelet models are mainly used: the steady flamelet model (SFM) [10] and the unsteady flamelet model, such as the flamelet progress variable model (FPV) [11]. The SFM model neglects the differential molecular diffusion effects; the FPV model performs better when dealing with flame local extinction and reignition.

The probability density function (PDF) model is mainly about the transported probability density function [12]. The transported equations of the joint probability density functions of the interested thermodynamic variables and the turbulence will be solved in this model. The

transported PDF method has been proven can capture flame local extinction and reignition for the transient flame dynamics problems [13]. The PDF model is suitable to solve the closure problems that need to consider detailed chemical reaction source terms; it can be used to couple with other turbulent models. For example, the RANS-PDF coupling model has been developed; the PDF method has also been extended to the LES method by using a model called FDF [12]. This model has recently been widely used for simulating turbulent fluctuations; it is considered one of the most effective tools for solving chemical components in reaction streams [12].

To summarize, this section briefly introduces turbulent modeling and turbulent combustion modeling. Three turbulent models have been discussed: the DNS model, the RANS model, and the LES model. Two different turbulent combustion models have been reviewed: the flamelet model and the transported PDF model. The differential molecular diffusion (DMD) effect plays a significant role in the mixing. However, it is neglected in most flamelet model simulations; this work will improve that by investigating the representativity of DMD for the laminar flamelet model. The advantages of the transported PDF model will also be used to enhance fire research. In Section 1.4, the DMD effect will be introduced, and the benefits and challenges of applying this model will be investigated.

1.4 Differential molecular diffusion

Molecular diffusion mixes the fuel and oxidant molecules and transports product molecules; it is a crucial process in turbulent combustion. Differential molecular diffusion (DMD) is a widespread physical phenomenon in all turbulent combustion problems. Being able to capture DMD is an essential measure of the predictive capability of turbulent combustion models. The flamelet models are extensively used for turbulent non-premixed combustion modeling, and the representativity of DMD by using a laminar flamelet is thus a prerequisite for flamelet models to be capable of predicting DMD. However, in most models, equal molecular diffusion is usually assumed, and there is no comprehensive work to systematically study the performance of laminar flamelets to describe DMD in turbulent flames. The incorporation of DMD in flamelet models remains a significant challenge.

Recently, there has been some success in incorporating the effect of DMD on turbulent combustion models. In the transported PDF combined with the Lagrangian particle method, equal molecular diffusion is necessary to allow the widely used random walk model for treating

molecular diffusion [14]. McDermott and Pope [15] developed the mean shift (MS) model to replace the random walk model to deal with the differential molecular diffusion in the physical space. Zhang and Wang [16] introduced the variance consistent mean shift (VCMS) model to improve the MS model to yield consistent molecular transport of scalar variance under the effect of DMD. In the mixture-fraction-based turbulent combustion models such as flamelet models and CMC, the assumption of equal molecular diffusion is a fundamental requirement for rigorously defining the conserved scalar mixture fraction. Pitsch and Peters [17] introduced a new definition of the mixture fraction based on its conservation equation and the boundary conditions to present the effect of DMD in the laminar flamelet. The derived flamelet model with DMD, however, yields significant over-prediction of the impact of DMD in turbulent jet flames. Wang [18] analyzed the limiting behaviors of DMD at small and large Reynolds numbers and developed a class of DMD models called the linear differential diffusion (LDD) and non-linear differential diffusion (NDD) models for the flamelet models. The LDD and NDD flamelet models can reasonably represent DMD's effect compared with the experimental data from turbulent non-premixed jet flames [19]. Ma and Devaud [20] extended the CMC model by adding the differential diffusion effects for the species and enthalpy in the CMC models. The CMC formulation, including differential diffusion, can improve the NO prediction near the hydrogen-air flame nozzle. Despite these latest model advancements to add the effect of DMD to modeling turbulent non-premixed combustion, much more effort is desired to produce accurate and consistent DMD models. The second chapter of this work mainly concerns the representation of DMD for flamelet models.

The accuracy of the flamelet models largely depends on the representation of laminar flamelet for flames' physics in turbulence. In the past, many works have been done to examine the representativity of laminar flamelets for turbulent flames, e.g., the effect of turbulence straining, curvature, local extinction, radiation, etc. Cuenot and Poinso [21] found that several effects may limit the laminar flamelet assumption: when the flow time scale is much smaller than the chemical time scale, the unsteadiness effects will occur and lead the flame to lose its laminar flamelet structure; the curvature effects will increase the total reaction rate due to the lateral diffusion; the strain rate will become much larger than the value predicted in the flamelet library and cause the happening of local quenching, the subsequent strong unsteady effects will cause the flame to burn beyond the laminar critical Damköhler number. Bray and Peters [22] also found significant

differences between the laminar flamelet's radiation heat loss and the radiation heat loss in the actual flame.

The representation of DMD in turbulent flames using the laminar flamelet is vital to developing accurate flamelet models. However, there is no comprehensive work to systematically investigate the representation of laminar flamelet for describing DMD in turbulent flames. This work is presented to fill this gap by examining the DMD characteristics in turbulent flames and the necessary laminar flamelet conditions to reproduce these characteristics.

To summarize, this section introduced differential molecular diffusion and its importance in developing an accurate flamelet model. The work of extending turbulent combustion models to consider the effect of DMD and the representative of laminar flamelet for turbulent flames is briefly described. In Section 1.5, the phenomenon of flame instability and the study of flame extinction limits will be introduced, and the significance of capturing flame extinction limits will be discussed.

1.5 Flame instability and extinction limits

Studying flame instability can better understand the combustion process, guide the industrial combustion devices operating under proper conditions, enhance combustion efficiency, and reduce mechanical work vibration. The unstable behaviors of the hydrogen-air flames are usually investigated since hydrogen is much lighter than air and is easy to cause an unstable phenomenon during combustion. The flame instability significantly affects diffusion flames' dynamic behavior; thus, it is tightly related to the thermal transport properties, diffusion process, and the flame's wrinkled structures. The laminar-to-turbulent transition is one primary behavior caused by flame instabilities.

Flame instability and stabilization are critical for combustor design, especially for gas turbines, scramjets, or other devices [23, 24]. In the late 19th century, Smithells and Ingle [25] discussed their early discovery about flame front instability; the "polyhedral flame structure" now usually referred to as the "cellular flame structure [26]" was observed. S. Ishizuka et al. [27] studied the flame-front instability and used the functions to describe the relationship between the concentrations of reactants and the instability boundaries. Yule et al. [28] first investigate the transitional flame's inner and outer vortex structures. Roquemore et al. [29] also found this double vertex structure in their experiments. The smaller inner vortices in the shear layer of the flame are

generated by the Kelvin-Helmholtz instabilities, and the large-scale vortices in the outer region of the flame are buoyancy-driven. Their experiment also found that the flame's oscillation frequency remains as constant as 15 Hz. Davis et al. [30] used simulations to prove that buoyancy is the source of outside flame flicker; they showed that the flame would have no outer structures when gravity equals zero. Durao et al. [31] discovered that the frequency of flame oscillation could not be affected by the fuel type or the design method of the fuel nozzle; tests using a range of different fuel velocities proved that the flame oscillation frequency is also independent of fuel velocities. In their calculations, Katta et al. [32] revealed the coherent nature of internal structures; they found the inner structures can maintain self-coherence long distances. The buoyancy was found to play an essential role in this process. Shin & Ferziger [33] analyzed the linear instability of reacting mixing layers; they found several modes of instability in the outer region of the mixing layer. After Shin's work, Reynolds et al. [34] detailed evaluated these different modes; the effects of compressibility, the ratio of density, and velocity on instability characteristics are carefully examined for each mode. The flow instability characteristics have been further studied by examining the effects of reaction chemistry; Matthias Ihme et al. [35] found that the chemical mechanisms and the transport model can affect instability.

Capturing fire extinction limits in simulations is critical for developing predictive capabilities for combustion investigations; it is also important to developing and applying laminar flamelet concepts to turbulent flame propagation. Although many previous studies have investigated the extinction limits of flames [36 - 39], no one has provided detailed and comprehensive model validation results. Many experimental studies have explored extinction theory and the extinguishing limits for different kinds of fuels [40]. The extinguishing of flame is mainly manifested by flame-based detachment, lift-off from the burner, and the final blow-off. The weakening of the edge reaction kernel is responsible for this kind of flame instability [41]. Most previous experimental setups on flame extinction limits are too simple, and most of them are focused on laminar flames, and the corresponding numerical calculations are not well studied. The comparative conclusions obtained do not provide insight for model development and improvement. In this work, detailed testing of flame extinguishment limits with various mixing models and parameters was performed to support the development and improvement of predictive fires.

To summarize, many works have investigated flame instabilities and extinction limits. However, simplified experimental setups and reduced-order models were widely used in these

investigations; the flame behaviors cannot be accurately captured and observed. This work aims to provide a detailed investigation of the flame extinction phenomenon and find the source of the instabilities. Local flame extinctions investigations will better understand the transitional processes and buoyancy-driven instabilities, and the importance of mixing modeling in fire simulations will be revealed.

1.6 Open questions and challenges in turbulent combustion modeling

In this work, we investigate two different types of turbulent diffusion combustion: the momentum-dominant jet flames and buoyancy-controlled pool fires. For the momentum-dominant jet flames, we focus on using flamelet models to model turbulent non-premixed combustion. For the buoyancy-controlled pool fires, the critical work related to using the combined large-eddy simulation (LES) and transported probability density function (PDF) methods for the predictions of fire extinction.

The challenges are mainly from two aspects: the differential/preferential molecular diffusion (DMD) and capturing fire extinction limit for developing predictive capabilities.

- Predictive modeling of turbulent non-premixed combustion requires an accurate account of the underlying multi-scale multi-physicochemical processes such as turbulent transport, detailed chemical kinetics, and multi-component molecular diffusion. Molecular diffusion is a very important part of the mixing process at small scales in turbulent combustion; the fuel and oxidizer cannot mix and trigger a chemical reaction without molecular diffusion. The multi-component molecular diffusion in combustion is characterized by the differential molecular diffusion (DMD) caused by the different molecular diffusion coefficients of the various components (species and heat). Typically, DMD occurs at a length scale that is not resolved in practical modeling using Reynolds averaged Navier-Stokes (RANS) or large-eddy simulations (LES). The account of DMD in turbulent combustion simulations thus relies entirely on physical modeling, which remains a significant challenge.

The effect of DMD is commonly neglected in the past investigations of turbulent non-premixed combustion modeling; the equal molecular diffusivity or unit Lewis number are usually used, and the molecular transport is neglected based on the argument that turbulent transport dominates the diffusion transport in RANS or LES. The validity of

this assumption is highly questionable, and relaxing the assumptions is desired. However, it is not trivial to eliminate the equal molecular diffusion assumption because it is deeply rooted in many existing turbulent combustion models like the transported probability density function (PDF) method, the conditional moment closure (CMC) method, and the flamelet models.

- In most previous studies, either the experimental investigation or the numerical simulation, their conclusions may not be extrapolated to realistic conditions. Almost all studies used simple configurations, mostly limited to laminar flow flames. Excellent investigations should consider both the complexity of the actual flame (incorporating the necessary turbulence phenomenon and lift-off extinction) and the detailed diagnostic results (including comprehensive measurements of extinction performance) required for CFD model development and validation. The numerical simulation should focus on assessing and improving the ability of the current fire model to predict fire extinction behavior. However, compared to the lab-scale jet flames, the fire configurations have a relatively larger size of the flame region. The fuel port size of the fire case generally has an order of tens of centimeters, and the flame height of the fire has an order of meters. Due to the limitation of computer cost, the previous simulations generally used highly simplified chemical mechanisms such as the 1-step or 2-step combustion mechanism. These investigations also relied on low order or highly simplified turbulence and combustion models such as the eddy dissipation concept (EDC) or the eddy dissipation model (EDM) to simulate. These non-exhaustive research studies cannot provide insights for model development and improvement.

All the challenges mentioned above lead us to think about a better way to assess the representativity of DMD in turbulent flames and develop a predictive model for fire extinction. Since the flamelet models are extensively used for turbulent non-premixed combustion modeling, the representativity of DMD by using a laminar flamelet is thus a possible way to be capable of predicting DMD in turbulent combustion modeling. And using a high ordering model to perform detailed investigations of the flame instabilities and extinction limits with various mixing models and parameters might be helpful for further enhancement of extinction predicting.

1.7 Objectives and outline of the dissertation

This work aims to find possible solutions for the challenges summarized in Section 1.6 and provides implications for developing and improving predictive models for turbulent flames. The specific objectives include studying the representativity of differential molecular diffusion by using laminar flamelet for turbulent non-premixed combustion modeling and the transported probability density function modeling of fire extinction. The detailed objectives of this dissertation are listed below:

- **Representativity of differential molecular diffusion by using laminar flamelet**
 - 1) Examine the representativity of laminar flamelet using two different conceptual burners, the opposed jet burner, and the Tsuji burner. Find qualitatively different results for the effect of DMD in laminar flamelet between these two burners;
 - 2) Examine the effect of DMD in practically relevant flows and flames. Use a non-reacting laminar jet mixing and a turbulent jet mixing to show the representativity of the Tsuji burner laminar flamelet and the limitation of the opposed jet laminar flamelet.
- **Transported probability density function modeling of fire extinction**
 - 1) Generate combined large-eddy simulation (LES) and transported probability density function (PDF) methods for the predictions of fire extinction;
 - 2) Test the validation of the coupled model by using the experimental data;
 - 3) Use different mixing models and model parameters to capture fire extinction limits and compare them with the experimental data.

The remaining parts of this dissertation are as follows:

- **Chapter 2** focuses on the quantitative presentation of the differential molecular diffusion effect and the generation of laminar flamelets. The functions of flamelet models will be reviewed to provide basic modeling ideas. Then simulations will be used to reveal the importance of considering DMD in the flamelet model. After that, the method of using two different burners, the opposed jet burner and the Tsuji burner, to generate the laminar flamelets will be systematically introduced. Finally, the comparison between these two different burners will be presented, and the similarities and differences will be quantitatively compared.

- **Chapter 3** focuses on the practical relevance of the critical difference and the new finding between the opposed jet burner and the Tsuji burner. A non-reacting laminar jet mixing and a turbulent jet mixing will be used to show the representativity of the laminar flamelet. The gap between the existing knowledge of DMD in turbulent combustion and the practical applications will be reduced by these important findings in this chapter.
- **Chapter 4** focuses on coupling large-eddy simulation (LES) and transported probability density function (PDF) methods. The LES and transported PDF model will be introduced. A brief discussion about the governing equations of the NIST Fire Dynamics Simulator (FDS) code and an in-house PDF code called HPDF will be provided, and the coupled method of these two approaches will also be presented. The experimental setup of the University of Maryland line burner will be reported.
- **Chapter 5** focuses on capturing the fire extinction limit in simulations. The experimental data will validate the coupled model's simulation results. The combustion efficiency under the different oxygen depletion levels in the oxidizer will be analyzed. The coupled model's capability to capture the fire extinction limit is assessed by using the experimental data. The differences between the performance of different mixing models and parameters will be analyzed using the flame index concept.
- **Chapter 6** summarizes the dissertation's major conclusions and proposes potential future work.

2. REPRESENTATIVITY OF DMD BY USING LAMINAR FLAMELET MODEL

As described in Chapter 1, the flamelet models are widely used for turbulent non-premixed combustion modeling, and the representativity of DMD by using a laminar flamelet is thus a prerequisite for flamelet models to be capable of predicting DMD. Before systematically investigating the DMD effect, getting a rough idea about the laminar flamelet concept and implementation is critical. In this chapter, the introduction of the flamelet model governing equations will be presented. A quantitative presentation will show the DMD effect in a transitional flame. Finally, the use of two different burners, the opposed jet burner and the Tsuji burner, to produce laminar flames will be systematically described. Numerical simulations for both burners will be conducted to compare the laminar flamelet generated using the opposed jet burner and the Tsuji burner.

2.1 Concept and governing equations of laminar flamelet model

The flamelet concept represents the turbulent flame by using the one-dimensional non-premixed laminar flamelet structures [18], and these laminar flame structures can be represented using the mixture fractions, the strain rates, and the scalar dissipation rates. A presumed PDF will deal with the interactions between the chemical reactions and the turbulent flow field. The integrations will generate a pre-calculated look-up table, which will be used to simulate the turbulent flame. When doing the simulation, all thermochemical quantities can be obtained from this look-up table.

The conservation equation of the species mass fraction is shown below

$$\frac{\partial \rho Y_\alpha}{\partial t} + \frac{\partial \rho u Y_\alpha}{\partial x} = \frac{\partial}{\partial x} \left(D_\alpha \frac{\partial Y_\alpha}{\partial x} \right) + S_\alpha, \quad (2.1)$$

where Y_α represents the mass fraction of species α , x is the axial direction distance, ρ is the density of species, u represents the velocity in the axial direction, D_α means the molecular diffusivity of the species α in the gas mixture, S_α represents the chemical reaction source term of species α .

When applying the assumptions of equal diffusion and use of the Lewis number equals to one, the Equation (2.1) can be derived as

$$\frac{\partial \rho Y_\alpha}{\partial t} = \frac{\rho \chi}{2} \frac{\partial^2 Y_\alpha}{\partial \xi^2} + S_\alpha, \quad (2.2)$$

where χ represents the scalar dissipation rate, and the mixture fraction ξ has a definition as

$$\frac{\partial \rho \xi_k}{\partial t} + \nabla \cdot (\rho \mathbf{u} \xi) = \nabla \cdot (\rho \mathbf{D}_\xi \nabla \cdot \xi). \quad (2.3)$$

The scalar dissipation rate and the mixture fraction have a relationship [10] that can be written as

$$\chi = \chi_{st} \frac{\exp\left[-2\left(\text{erfc}^{-1}\left(2\xi\right)\right)^2\right]}{\exp\left[-2\left(\text{erfc}^{-1}\left(2\xi_{st}\right)\right)^2\right]}, \quad (2.4)$$

the ξ_{st} subscript means the stoichiometric condition, and the erfc^{-1} means the inverse complementary error function. By using these equations, a function of the stoichiometric scalar dissipation rate and the mixture fraction can parameterize the laminar flamelet; the scalars of the laminar flamelet can be expressed as

$$\phi = \phi(\xi, \chi_{st}). \quad (2.5)$$

The temperatures, mass fractions of different species, diffusivities of different species, viscosities of different species, and other scalars of the turbulent flame can be obtained from the flamelet table generated based on these two variables.

For the generation of pre-calculated flamelet tables, a presumed PDF will be used for the joint distribution of stoichiometric scalar dissipation rate and the mixture fraction. Commonly, the mixture fraction uses a β distribution PDF, and the stoichiometric scalar dissipation rate uses a δ function PDF. The flamelet table can be generated from

$$\phi(\xi, \xi_{st}, \chi_{st}) = \iint \phi(\eta, \theta) f_{\xi, \chi_{st}}(\eta, \theta) d\eta d\theta, \quad (2.6)$$

where $f_{\xi, \chi_{st}}(\eta, \theta)$ is the joint function of stoichiometric scalar dissipation rate and mixture fraction, η represents the phase space variables of mixture fraction, θ is the corresponding phase space variables to χ_{st} .

The flamelet model has several advantages and has been widely used for turbulent combustion simulations. Because of the pre-generated look-up table, the computational cost can be significantly reduced when applying the flamelet model; this model can reveal the interaction between molecular transport and the chemical reaction. In Section 2.2, a hydrogen-air jet diffusion flame will be used to show the flamelet model implementation in practically relevant flows and flames.

2.2 Flamelet model implementations and simulations

In this section, a laboratory-scale experiment is adopted as a validation test case, and the corresponding simulations and quantitative comparisons will be used to demonstrate the implementation of the flamelet model considering DMD in transitional non-premixed combustion. The practically relevant flows and flames can help us get a rough idea about the laminar flamelet model and an intuitive understanding of the DMD effect.

2.2.1 Flamelet modeling of transitional diffusion flame

A laboratory experiment of hydrogen-air transitional diffusion flame conducted by Robert et al. [42] is used to demonstrate the flamelet modeling of the transitional diffusion flame. The reason to choose this flame is that hydrogen is much lighter than air and is easy to cause unstable phenomena during combustion; the DMD effect becomes crucial since molecular diffusion coefficients of hydrogen and air have a huge difference. This flame also has transient structures, the flow near the nozzle is laminar, and increasing turbulence is observed downstream. The temperature fluctuations of this diffusion flame are caused by a buoyancy-driven instability called Kelvin-Helmholtz instability.

The camera-taken picture and the schematic diagram of the diffusion flame experimental setup are shown in Figure 2.1. In the experiment, the fuel nozzle's inner diameter is 5 mm, the hydrogen jet comes out of the fuel nozzle with 7.7 m/s, and the air co-flow velocity is 0.15 m/s. The fuel jet has a calculated Reynolds number of 347.

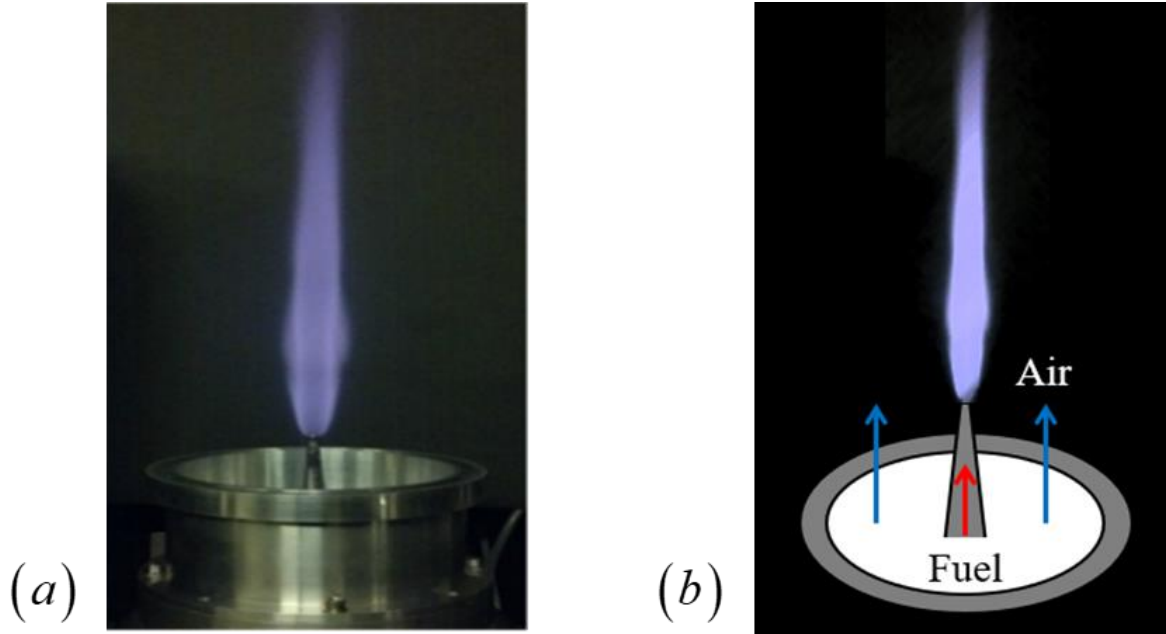


Figure 2.1. Experimental setup of the hydrogen-air transitional diffusion flame; (a) camera-taken picture of the experimental facility captured from Robert’s paper [42], (b) schematic diagram of the experimental facility.

The flame temperature is measured using the single-laser-shot femtosecond (fs) coherent anti-Stokes Raman scattering (CARS) technology. The statistic temperatures are the mean value of 4,000 laser pulse measurements; these data are obtained from various radial locations at six different elevations of the jet flame.

In the corresponding simulation, the jet of the hydrogen fuel locates in the center of the bottom boundary, and a cylindrical three-dimensional mesh is used for simulations with a size of $20 d \times 30 d \times 2\pi$, a small grid with a resolution of $108 \times 144 \times 48$ helps to get accurate results. The inlet velocity u_{inlet} is set as a constant 7.7 m/s; the co-flow velocity $u_{\text{co-flow}}$ is fixed as 0.15 m/s. According to the experimental setup, the computational domain’s initial conditions have a 300 K temperature and 101,325 Pa pressure. The standard value of 9.8066 m/s^2 is used for gravitational acceleration to consider the buoyancy effect. The open and passive flow boundaries are used for the top side, and on all four sides around the calculation domain, the background gas of the simulation is set as ambient air.

The compressible three-dimensional Navier–Stokes equations are used for the simulation, and all the mass, momentum, and scalars transport equations use cylindrical coordinates. The

second-order accuracy standard finite volume method (FVM) is employed in space and time. The mass and momentum conservation equations and the mixture fraction transport equation are solved, and a single laminar steady flamelet is used to calculate combustion.

Several high-speed camera-taken images of the hydrogen-air transitional diffusion flame captured from Robert's paper [42] and the corresponding calculated instantaneous temperature grayscale contour plots are shown in Figure 2.2. The luminous flame zone has regular fluctuations generated by buoyancy with 10 - 20 Hz oscillation frequency in the experiment. The calculated results share a similar oscillation frequency as the experiment; thus, the flamelet model is proven capable of capturing the flame instabilities. The flamelet model's validation for modeling transitional diffusion flames is also approved. Detailed quantitative comparisons of temperatures at different axial locations will be provided in Section 2.2.2 to get a clear picture of the effect of DMD.

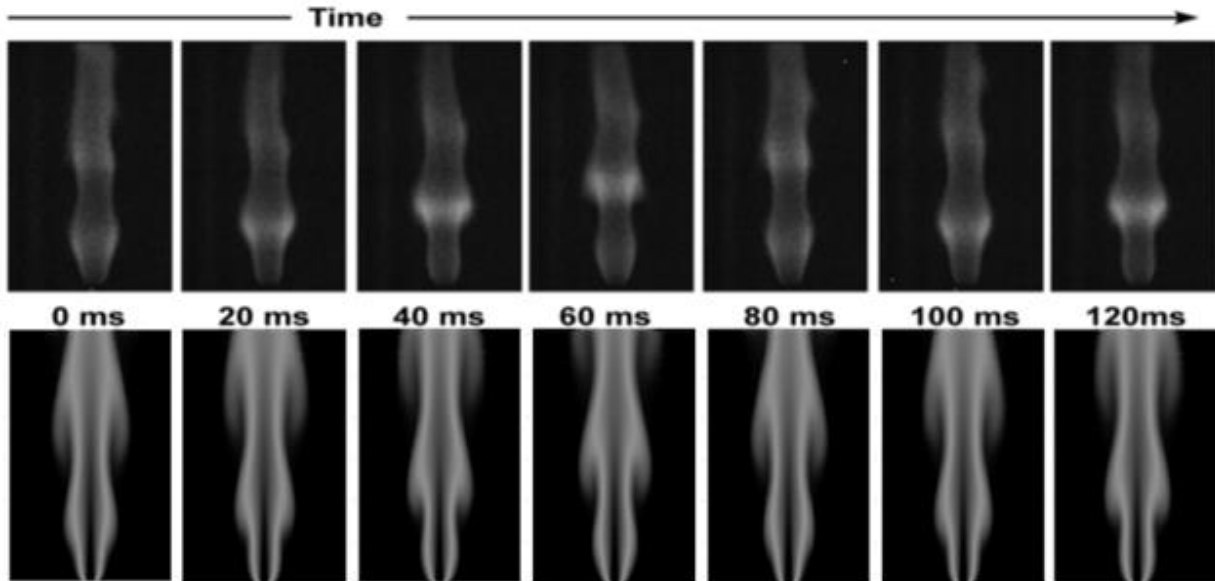


Figure 2.2. Front views show the fluctuations of the luminous zone in the hydrogen-air transitional diffusion flame captured from Robert's paper [42] (up figures) and the corresponding simulation results (bottom contour plots).

2.2.2 Quantitative presentation of DMD effect in the transitional diffusion flame

Comparisons between the simulations of previously introduced flame are used to study the DMD effect. These simulations use different types of pre-calculated flamelet look-up tables. In the

first simulation, a unity Lewis number equals one, and the equal molecular diffusion are assumed to calculate the flamelet look-up table. The DMD effect is considered when generating the look-up table for the second simulation.

The calculation results of two different simulations are shown in Figure 2.3. The average temperatures at different radial and axial locations are plotted. When considering the DMD effects, the temperature has a higher value than the equal diffusion and unity Lewis number assumption. The differential diffusion effects between different species increase the mixing speed and enhance the flame thermal diffusion [43]. The comparisons between the simulation considering DMD effects and the experimental data are shown in Figure 2.4.

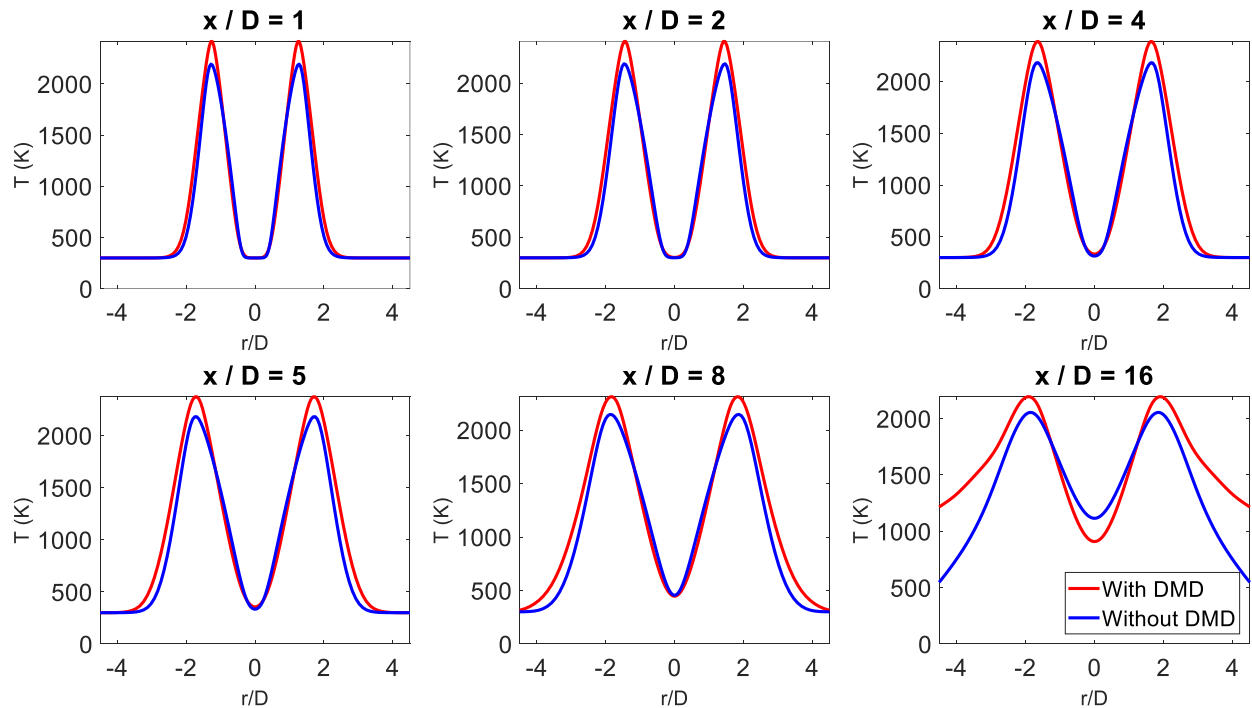


Figure 2.3. The time-averaged temperatures at different axial locations ($x/D = 1, 2, 4, 5, 8,$ and 16) of the hydrogen-air transitional diffusion flame with (red line) and without (blue line) considering DMD effects.

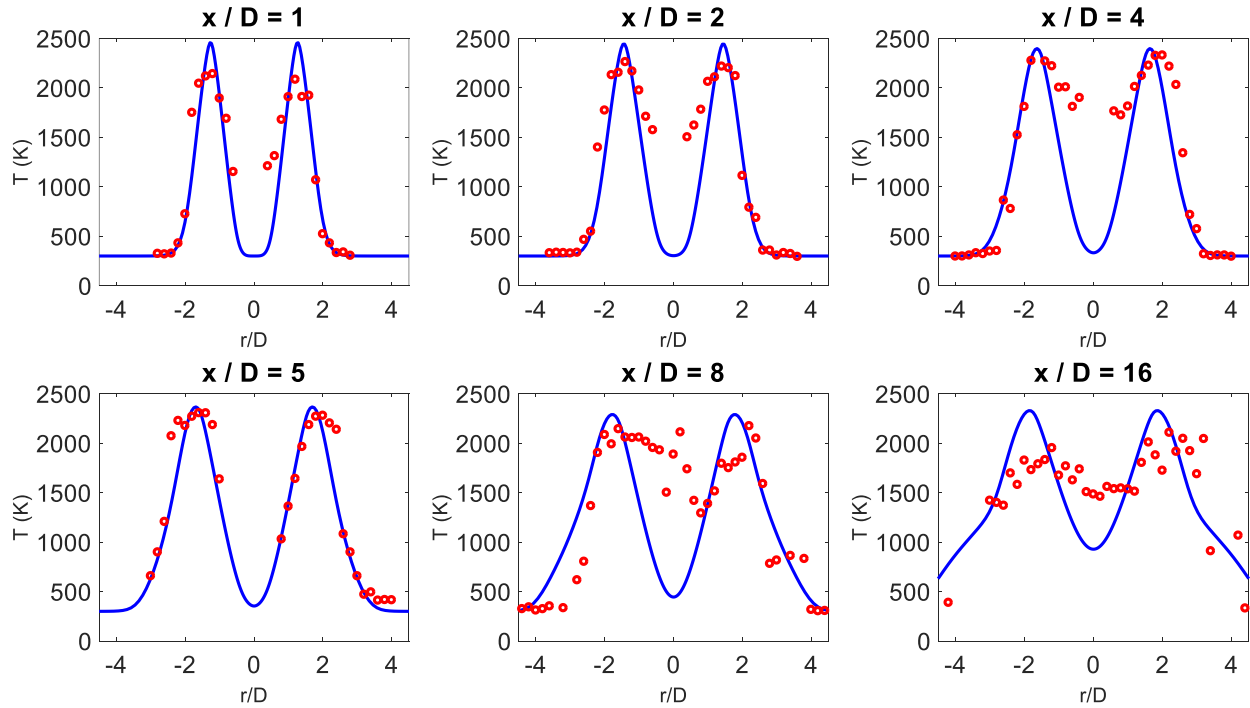


Figure 2.4. The experimental data (red dots) and the calculated results (blue line) consider the DMD effects of the average temperature at different axial locations ($x/D = 1, 2, 4, 5, 8,$ and 16) of the hydrogen-air transitional diffusion flame.

In the experiment, the nitrogen concentration at the centerline $r/d = 0$ is insufficient for the CARS signal generation. Thus the nitrogen concentration on the centerline for lower x/d locations cannot be measured. The calculation results are very close to the experimental data in the flame region between $x/d = 2$ and $x/d = 8$. According to the previous analysis, the DMD effects increase the average temperature values; thus, the flamelet model considering the DMD effect has higher accuracy. The hydrogen-air transitional diffusion flame calculation proves the importance of differential molecular diffusion in simulating transitional flames, especially for the flame with a considerable difference between the fuel and oxidizer's molecular diffusion coefficients.

This section shows the implementations of the flamelet model by using a practically relevant hydrogen-air transitional diffusion flame and quantitatively presents the DMD's effect by comparing simulation and experimental data. The temperature comparison between the calculation and experimental data shows that considering DMD in flamelet modeling can significantly improve the simulation results. The flamelet table generation using two different conceptual burner

configurations will be introduced in Section 2.3, and then the comparisons between these two methods will be examined.

2.3 Representation of DMD by using two different conceptual burners

There are mainly two canonical experimental setups for studying laminar non-premixed flamelet, the opposed jet burner [44] and the Tsuji burner [23]. Both burners are shown in Figure 2.5; they have been used widely for studying laminar non-premixed flamelets. The opposed jet burner can stabilize the laminar diffusion flame and provide a convenient way for its study. The flame strength and structure of opposed jets have been studied numerically and experimentally, and numerous opposed jet flames' local extinction and extinction limits have also been investigated. The Tsuji burner can establish a diffusion flame in the forward stagnation region [45], which is suitable for examining the detailed flame structure and reaction rates. The extinction limits, aerodynamic effects, and the temperature and species concentration distributions of Tsuji burner flame were studied in detail [23]. Despite the structural difference between the opposed jet burner and the Tsuji burner, they are generally considered identical for generating laminar flamelets. Both burners can be used to characterize the laminar flamelet to investigate the representativity of DMD.

To examine the representativity of the laminar flamelet for DMD, we choose two widely used experimental configurations based on the opposed jet burner and the Tsuji burner as the conceptual burners, as illustrated in Figure 2.5, to describe the laminar flamelet. The simulations are conducted in ANSYS FLUENT [46] commercial CFD code for these two different burner configurations. The simulation setups will be discussed in the following sections. A quick comparison of the simulation results is made in Section 3 to demonstrate the similarities and differences between the two burners' configurations for representing flamelets in terms of DMD. The primary purpose is to study the fundamental difference of laminar flamelets in terms of the effect of DMD and to investigate the representativity of the different laminar flamelets for DMD in turbulent flames.

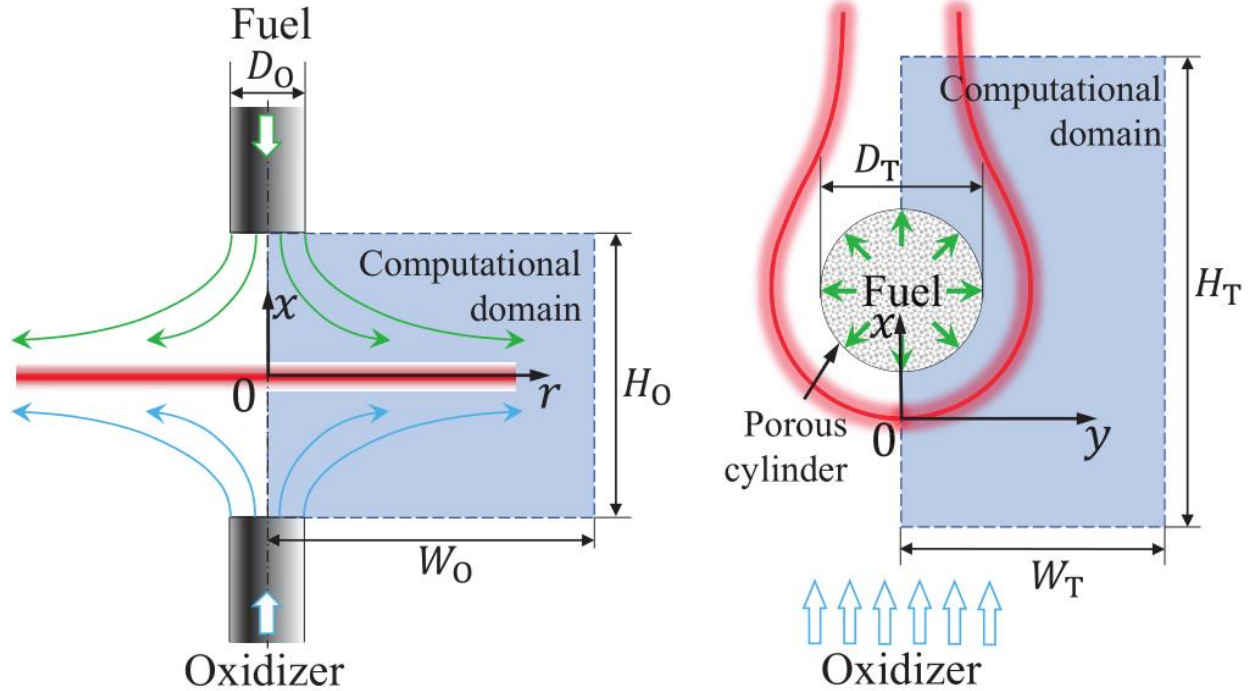


Figure 2.5. Schematics of the opposed jet burner (left) and the Tsuji burner (right) and their computational domains. The diameters of the fuel and oxidizer jets for the opposed jet burner are all set as D_O , the distance between the two jet exits is H_O . The porous cylinder of the Tsuji burner has a diameter of D_T .

2.3.1 Laminar flamelet based on opposed jet burner

The opposed jet burner was widely used for studying laminar flames numerically [47] and experimentally [48]. In the early simulation studies of opposed jet flames, a potential flow theory was used to prescribe the flow field based on two-point sources of potential flows placed infinitely apart. Lutz et al. [49] extended the potential flow theory to allow a more compact simulation setup similar to the experimental setup, as shown in Figure 2.5. Their approach has been the standard approach for CHEMKIN. The supplies of the two jets are not infinitely apart but with a distance H_O . Inlet diffusion boundary condition is prescribed at both jet boundaries for scalar transport to allow combustion products and energy to diffuse back into the jets when H_O is relatively small as illustrated in Figure 2.6. The profiles of the mass fractions of fuel Y_{fuel} , oxidizer Y_{oxid} , and product Y_{prod} are also demonstrated. The inlet diffusion boundary condition is generally written as

$$\begin{aligned}
V_O \phi_{k,O} &= \left(V_O \phi_k - D_k \frac{d\phi_k}{dx} \right)_{x=-L_O}, \\
V_F \phi_{k,F} &= \left(V_F \phi_k + D_k \frac{d\phi_k}{dx} \right)_{x=+L_F},
\end{aligned} \tag{2.7}$$

where $x = -L_O$ and $x = +L_F$ are the inlet boundaries of the oxidizer and fuel. V_F represents the bulk fuel inflow velocity, V_O represents the bulk oxidizer inflow velocity, D_k represents the molecular diffusivity of k th species, $\phi_{k,F}$ is the scalar values in the fuel, and $\phi_{k,O}$ is the scalar values of oxidizer.

The allowance of inlet diffusion essentially makes the distance H'_o between the two sources of jet supplies farther apart than H_o . The distance H'_o is loosely defined as the distance between locations where pure fuel and pure oxidizer are detected, as illustrated in Figure 2.6 (left plot). The inlet diffusion makes the fuel supplies and oxidizer freely approach each other, similar to the treatment based on the potential theory with the two jets infinitely apart. We refer to this traditionally opposed jet burner as an unconstrained opposed jet burner. The unconstrained opposed jet burner has been the standard approach for opposed jet flames. An embedded assumption in all the past studies is that the sources of the two jets are effectively far apart even though the two jets are separated by a finite distance H_o . This common assumption in opposed jet flames will be revisited in this work. We generalize the opposed jet burner in a conceptual design and introduce modifications to the burner. First, we enable the choice of inlet diffusion. We disable the inlet diffusion to produce a different setup, as illustrated in Figure 2.6 (right plot), so that the distance between the fuel and oxidizer is the same as the distance between the two jets. We refer to this generalized opposed jet burner as a constrained opposed jet burner. The inlet diffusion is disabled by setting the boundary condition in the computations as

$$\phi_k(x = -L_O) = \phi_{k,O}, \quad \phi_k(x = L_F) = \phi_{k,F}, \tag{2.8}$$

where ϕ_k is the k th scalar (energy or species mass fraction) in the system, $\phi_{k,F}$ and $\phi_{k,O}$ are the scalar values in the fuel and oxidizer, respectively. It is shown later that the DMD found in opposed jet flames with disabled or suppressed inlet diffusion is more representative of DMD in laminar jet flames and turbulent flames. Thus, it is of theoretical importance to study the generalized opposed jet flames without inlet diffusion. Modifying inlet diffusion can be readily done

computationally. It is also possible to at least suppress inlet diffusion in a laboratory, e.g., by replacing the tubes for the jet with porous media. This work focus on only a computational study. A second modification to the opposed jet burner is to use different inflow speeds from the two jets, which are often set to be the same in previous studies (or, more precisely, the momentum of both jets are set to be the same so that the flame front is near the center between the two jets).

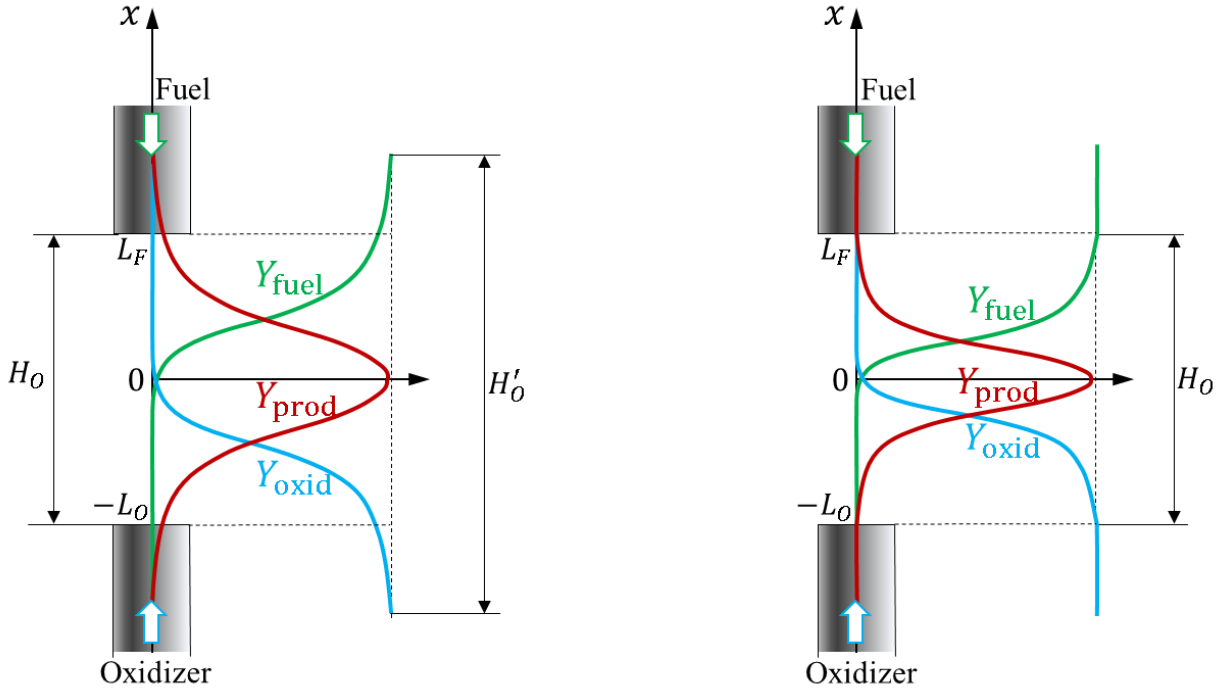


Figure 2.6. Illustration of the profiles of mass fractions of fuel Y_{fuel} , oxidizer Y_{oxid} , and products Y_{prod} inside an opposed jet flame with inlet diffusion at both jet inlets (left) and without inlet diffusion (right).

A velocity ratio of the fuel and the oxidizer jet in a generalized opposed jet burner is introduced to facilitate the discussion,

$$R = \frac{V_F}{V_O}, \quad (2.9)$$

the common setup for the traditionally opposed jet burner is $R=1$ to let the momentum of both jets be set to be the same and centralize the flame front in the burner.

Two-dimensional axisymmetric ANSYS FLUENT simulations of the opposed jet laminar flames are set up as follows. Steady-state simulations are considered in all of the discussions below. The computational domain is chosen as shown in Figure 2.5 with the jet diameter $D_o = 0.01$ m, $H_o / D_o = 2$, and $W_o / D_o = 10$. The fuel consists of 36% H₂ and 64% CO₂ by volume, and the oxidizer is air (21% O₂ and 79% N₂ by volume). The fuel composition is to follow the experimental conditions in [50, 51] for a turbulent jet mixing and jet flame, which will be used in the discussions in the following sections. The fuel and oxidizer temperatures are set to be 300 K. The fuel and air velocities are $V_F = 0.4$ m/s and $V_O = 0.4$ m/s by default, respectively, and these values will be tuned in later discussions. The fuel and oxidizer jets inlets are set as velocity inlets with uniform inflow, the adjacent boundaries are treated as adiabatic walls, the lateral boundary is a pressure outlet, and the axis is symmetric. Inlet diffusion is enabled for the transport of the species and energy. The total number of grid points is about 100,000, determined based on a grid convergence study. The mixture-averaged diffusion model [44] is used for molecular diffusion, and the GRI-Mech 3.0 mechanism [52] is used for chemical reactions. The nominal strain rate a_s for the opposed jet burner is commonly defined as [53]

$$a_s = \frac{2(-V_o)}{H_o} \left[1 + \frac{V_F}{(-V_o)} \sqrt{\frac{\rho_F}{\rho_o}} \right], \quad (2.10)$$

for this calculation, the momentum of both fuel and oxidizer jets are set to be the same; Equation (2.10) can be written as

$$a_s = \frac{2(V_F + V_o)}{H_o}, \quad (2.11)$$

the default strain rate for the opposed jet flame case is $a_s = 80 \text{ s}^{-1}$.

2.3.2 Laminar flamelet based on Tsuji burner

The Tsuji burner is a widely used alternative to the opposed jet burner for the study of laminar flames experimentally and numerically. The burner is illustrated in Figure 2.5 (right). A cylinder is placed in a free stream of the oxidizer. Fuel emerges from the surface of a cylinder made of porous media. A curved flame front is formed around the cylinder. The Tsuji burner is geometrically different from the opposed jet burner. However, it is generally considered that the

Tsuji burner is equivalent to the opposed jet burner in the literature for producing laminar flamelet structures in flamelet models for turbulent combustion. To our best knowledge, no work has been reported to discuss the difference between them comprehensively. This work is the first attempt to examine the difference between the two burners in describing the effect of DMD in laminar flamelets.

The ANSYS FLUENT simulations of the Tsuji burner are set up as follows. The two-dimensional computational domain is shown in Figure 2.5 (right) with the porous cylinder diameter $D_T = 0.05$ m, $H_T / D_T = 10$, and $W_T / D_T = 5$. The porous cylinder significantly reduces the molecular diffusion of the gas inside it [54 - 56]. The inlet diffusion is thus disabled at the fuel inlet in the Tsuji burner. That is the key difference between the opposed jet burner and the Tsuji burner since the opposed jet burner allows inlet diffusion. When a flame is close to the inlet boundary, this difference in the inlet treatment can produce significantly different results. The difference will be discussed in the following sections. The fuel used in the simulations of the Tsuji burner is the same as that in the opposed jet burner. The fuel velocity is $V_F = 0.1$ m/s, and the air inflow velocity is $V_O = 1.0$ m/s by default, and these values will be tuned in later discussions. The fuel and air-jet inlets are set as velocity inlets with uniform inflow. A symmetric boundary condition is set for the centerline; all the other boundaries are pressure outlets. The total grid points are about 200,000, determined based on a grid convergence study. The molecular transport model and chemical reaction mechanism used in the simulations are the same as those in the opposed jet burner.

As described above, the Tsuji burner usually operates with the fuel supplied from the porous media cylinder. This setup is probably for the convenience of experimental studies. Computationally, we can easily swap the fuel and oxidizer supplies in the Tsuji burner, i.e., the oxidizer is from the porous burner, and the fuel serves as the free stream. This kind of swapped Tsuji burner is useful for the current discussion. To facilitate the discussion, we introduce a generalized Tsuji burner with the configurations of the fuel and oxidizer based on the velocity ratio R in Equation (2.9). If $R < 1$ ($V_F < V_O$), the fuel is supplied from the cylinder, and the oxidizer is the free stream. Otherwise, the fuel is the free stream, and the oxidizer comes from the cylinder. In other words, the low-speed stream is always from the porous media cylinder in the Tsuji burner. A nominal strain rate for the generalized Tsuji burner is defined as [44]

$$a_s = \frac{4 \times \max(V_F, V_O)}{D_T}, \quad (2.12)$$

the default strain rate for the above Tsuji flame case is $a_s = 80 \text{ s}^{-1}$.

This section shows the method of laminar flamelet generation by using the opposed jet burner and the Tsuji burner; the schematic diagrams and the computational domains and settings of these two burners are shown. Section 2.4 will compare the opposed jet burner and the Tsuji burner to show their similarity and difference. Then it will provide a preview of the issue addressed in the dissertation.

2.4 Comparison of the opposed jet burner and the Tsuji burner

In this section, a quick comparison of the opposed jet burner and the Tsuji burner will be conducted to demonstrate their similarity and difference. The purpose of the quick comparison is to provide a preview of the issue addressed in this dissertation. Detailed analysis of each burner has been discussed in Section 2.3.1 and Section 2.3.2. To directly compare the two burners, it is necessary to consider the mixture fraction space. Mixture fraction is a crucial parameter for studying non-premixed laminar flamelets. In the past, there have been many different definitions of mixture fractions. One example definition is based on the mass fraction of an element, say the hydrogen element, and is written as

$$\xi_H = \frac{Y_H - Y_{H,O}}{Y_{H,F} - Y_{H,O}}, \quad (2.13)$$

where Y_k is the mass fraction of element k , $Y_{k,F}$ is the mass fraction of element k in the fuel, and $Y_{k,O}$ is the mass fraction of element k in the oxidizer. The mixture fraction based on other elements such as carbon ξ_C can be defined similarly. The difference of ξ_C and ξ_H is commonly used to quantify the degree of DMD, and the DMD parameter z is defined as

$$z = \xi_C - \xi_H. \quad (2.14)$$

The second example is Bilger's definition [57] can be written as

$$\xi_{\text{Bilger}} = \frac{\beta - \beta_O}{\beta_F - \beta_O}, \quad (2.15)$$

where

$$\beta = \frac{2 \times Y_C}{W_C} + \frac{Y_H}{2 \times W_H} - \frac{Y_O}{W_O}, \quad (2.16)$$

where W_α is the atomic weight of the element α . The advantage of this definition is that it preserves the value of the stoichiometric condition ξ_{st} [57]. The Bilger's definition will be used throughout the dissertation.

2.4.1 The similarity of opposed jet and Tsuji burners

For a fair comparison, we choose the same baseline nominal strain rate of $a_s = 80 \text{ s}^{-1}$ for both burners. We set up one simulation case for the opposed jet burner following Section 2.3.1 with $V_F = V_O = 0.4 \text{ m/s}$ ($R=1$) corresponding to the chosen nominal strain rate $a_s = 80 \text{ s}^{-1}$. The nominal strain rate a_s provides an overall measure of the effect of flow stretching. For the Tsuji burner, we setup simulation case following Section 2.3.2 with the default fuel velocity from the porous cylinder $V_F = 10 \text{ cm/s}$ with the oxidizer velocity $V_O = 1 \text{ m/s}$ corresponding to $a_s = 80 \text{ s}^{-1}$. The respective velocity ratio is $R = 0.1$. Because of the geometrical difference between the two burners, it is impossible to directly compare them in the physical space. We extract the centerline laminar flamelet results from both burners and compare them in the mixture fraction space, and the mixture fraction ξ in Equation (2.15) is used.

The simulation cases described above are conducted and compared in Figure 2.7, where the laminar flamelet profiles are shown in terms of the temperature T , the species mass fractions Y_{H_2} , Y_{CO_2} , Y_{OH} , the scalar dissipation rate χ (based on ξ), and the DMD parameter z against ξ . The scalar dissipation rate χ is defined as

$$\chi = 2 \times \alpha \times \nabla \xi \cdot \nabla \xi, \quad (2.17)$$

where α represents the thermal diffusivity.

The results from both burners are almost the same except χ . Due to the difference in the burner geometry, the same nominal strain rate a_s in the two burners does not yield the same stretching in the flame, and the Tsuji burner yields slightly higher stretching than the opposed jet burner. Despite the slight difference in the stretching, the two laminar flamelet profiles are seen to be very similar in terms of both the magnitudes of the results and the peak locations in the mixture

fraction space. The location of equal diffusion $z = 0$ in the mixture fraction space, $\xi|_{z=0}$, is an important parameter to characterize DMD in this dissertation. The implication of the importance of capturing the variation of $\xi|_{z=0}$ will be discussed in Section 3. Both burners yield very similar values close to $\xi|_{z=0} \approx 0.71$.

As a result, these two burners can be considered to be equivalent if they are tuned properly to produce the laminar flamelets with DMD. That is the general view in the combustion community so far. To the best of the authors' knowledge, no difference between the two burners has been reported in the past; their representation of laminar flamelet structures has always been viewed as identical.

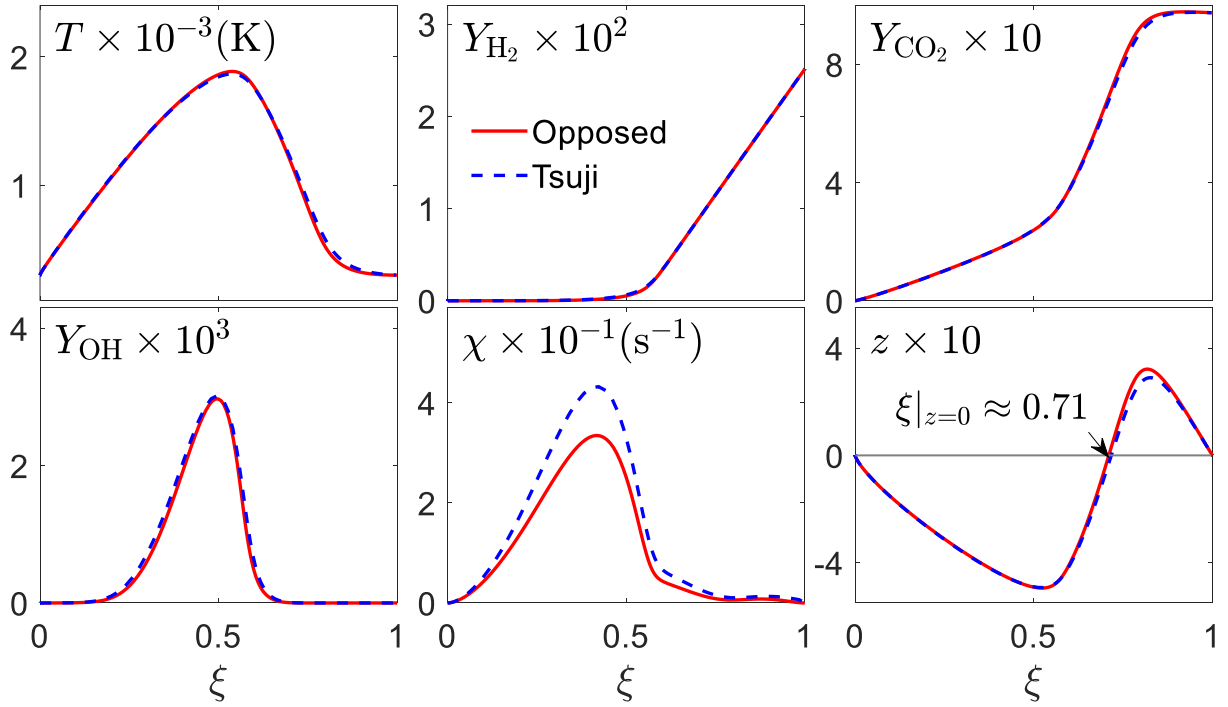


Figure 2.7. Comparison of the profiles of temperature T , species mass fractions Y_{H_2} , Y_{CO_2} , Y_{OH} , scalar dissipation rate χ (based on ξ), and the DMD parameter z against the mixture fraction ξ in the laminar non-premixed flames established in the opposed jet burner (solid lines) and the Tsuji burner (dashed lines) at the same nominal strain rate $a_s = 80 \text{ s}^{-1}$.

After presenting the similarities, Section 2.4.2 below presents a substantial difference between the two burners when representing the effect of DMD in laminar flamelet.

2.4.2 Difference between opposed jet and Tsuji burners

Non-reacting cases

A difference between the opposed jet burner and the Tsuji burner is that there is a free parameter, V_F , in the Tsuji burner that can be tuned without altering the free stream velocity V_O and hence the nominal strain rate a_s . The default value of V_F used in Figure 2.7 is $V_F = 0.1$ m/s. Numerical tests show that the predictions of z vary significantly when V_F is tuned even if the strain rate a_s is fixed in the Tsuji burner.

To examine this effect of V_F on the Tsuji burner predictions, we firstly consider a non-reacting case to isolate the effect of DMD from the chemical reaction. Figure 2.8 (a) shows the profiles of z against ξ in the non-reacting Tsuji burner for three different strain rates $a_s = 80 \text{ s}^{-1}$, 120 s^{-1} , and 160 s^{-1} . The values of V_F are chosen to be 0.04 m/s, 0.05 m/s, and 0.06 m/s for the three strain rates, respectively.

As shown in Figure 2.8 (a), the results closely agree with the experimental data [50]. The values of V_F are not reported in the experiment; hence, it is not known what the values V_F are corresponding to the experimental data. The good agreement of the predicted z with the experimental data provides some justification for the simulation results. In the simulations, the chosen values V_F are somewhat arbitrary. To quantify the effect V_F , we introduce a new parameter R , defined as the velocity ratio in Equation (2.9). In the Tsuji burner, the strain rate $a_s = 4V_O / D_T$ and R can be altered independently.

Figure 2.8 (b) shows the comparison of the z profiles in the non-reacting Tsuji burner under the same strain rate $a_s = 80 \text{ s}^{-1}$ but with different values of $R = 0.05$ and 0.1 . The results of z are highly sensitive to the values of R (or V_F). The equal diffusion location $\xi|_{z=0}$ varies from 0.5 to 0.77 when R decreases from 0.1 to 0.05. Further decreasing R can cause $\xi|_{z=0}$ to move towards one. The variation of $\xi|_{z=0}$ can also reach the region with $\xi|_{z=0} < 0.5$ to cover the whole mixture

fraction space if we choose $R > 1$ and swap the fuel and air inlets. In other words, when $R > 1$, we supply the fuel as the free stream in Figure 2.5 and let the air come from the porous cylinder. That is not easy to do in the experiment, but it is accessible in the simulations. The focus here is on a conceptual design of burners that are suitable for numerical generation of laminar flamelets for flamelet modeling of turbulent flames. We thus introduce a generalized Tsuji burner with two free parameters a_s and R . When $R < 1$, the fuel comes out of the porous cylinder as done in the traditional Tsuji burner; when $R > 1$, the oxidizer comes out of the porous cylinder as a conceptual alternative to the traditional Tsuji burner. The strain rate for the generalized burner is redefined as $a_s = 4 \times \max(V_F, V_O) / D_T$ in Equation (2.12). Thus, the variation of R can introduce a continuous variation of $\xi|_{z=0}$ in the whole mixture fraction space by using the generalized Tsuji burner without altering the strain rate, as shown in Figure 2.8 (b), which will be shown as the desired property for representative laminar flamelet with DMD. The detailed discussion about the desired property is delayed to Chapter 3. The results in Figure 2.8 (b) also indicate that the strain rate cannot fully parameterize steady laminar flamelet as previously thought [10]. A second parameter like R is needed. The actual choice of the second parameter that is feasible for flamelet modeling is another essential research task that is beyond the scope of this work and will be explored in our future study.

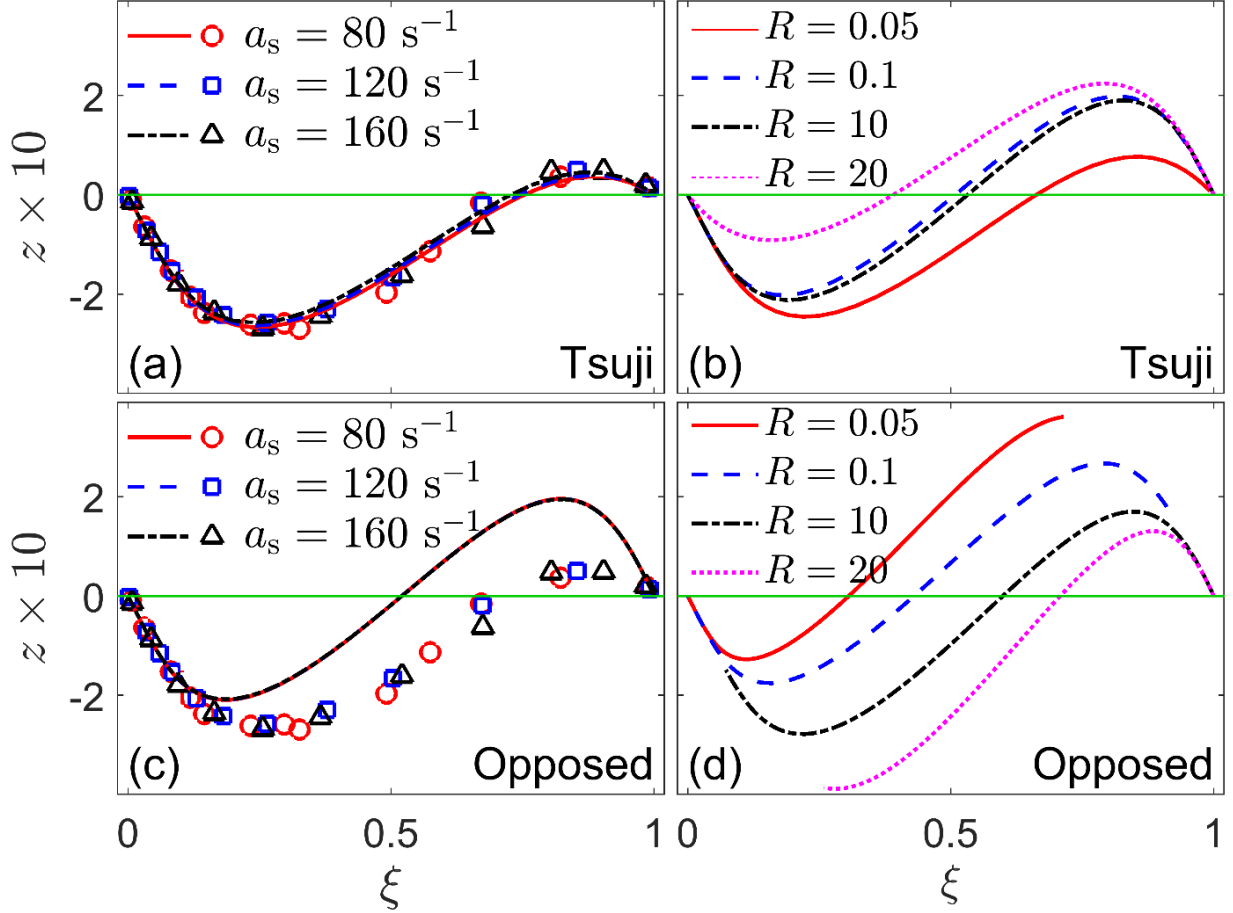


Figure 2.8. Comparison of the profiles of z against the mixture fraction ξ in the laminar non-reacting Tsuji burner (first row) and non-reacting opposed jet burner (second row). The left plots show the comparison of the results with the experimental data under different strain rates a_s , and the right plots show the results under the same strain rate $= 80 \text{ s}^{-1}$ but with different R .

In contrast, the non-reacting opposed jet burner yields substantially different results for z from the Tsuji burner. Figure 2.8 (c) compares the predictions of z in the opposed jet burner with the experimental data (obtained from the Tsuji burner [50]). In the results, R is specified to be $R = 1$, which is a typical choice for the opposed jet burner (or at least close to $R = 1$). The simulation results for the different strain rates are seen to be almost identical to each other. That is consistent with the theoretical results reported in Wang [18] for non-reacting opposed jet mixing layers. The predicted $\xi|_{z=0}$ is around 0.5, which is much lower than the measurement at $\xi|_{z=0} \approx 0.77$. We can vary R in the opposed jet burner too to examine its effect on z .

Figure 2.8 (d) compares the profiles of z in the non-reacting opposed jet burner under the same strain rate $a_s = 80 \text{ s}^{-1}$ but with different values of R . The change of R in the opposed jet burner can cause the change of $\xi|_{z=0}$ too. However, when R is too far away from unity (say $R > 10$ or $R < 0.1$), the integral structure of the produced laminar flamelet is lost, i.e., the flamelet does not cover the whole mixture fraction space, since the mixing layer is close to the boundary to cause the boundary values of the mixture fraction to move away from the pure fuel and oxidizer conditions because of inlet diffusion. The opposed jet burner thus cannot produce the entire laminar flamelets that feature a variation of $\xi|_{z=0}$ in the mixture fraction like the generalized Tsuji burner. To maintain the integral structure of the laminar flamelet, the variation of $\xi|_{z=0}$ is very limited in the opposed jet burner. That is considered to be the critical difference between the opposed jet burner and the Tsuji burner as conceptual burners for numerical generation of representative laminar flamelets for flamelet modeling of DMD in turbulent flames. To the best of the author's knowledge, this difference has not been reported in the past.

Figure 2.9 shows the predicted equal diffusion location $\xi|_{z=0}$ against R in both the non-reacting opposed jet burner and the non-reacting generalized Tsuji burner for two different strain rates $a_s = 40 \text{ s}^{-1}$ and 80 s^{-1} . For the Tsuji burner, the considered range of R is between $[3 \times 10^{-3}, 2.5 \times 10^2]$. For the opposed jet burner, the flamelet results from very large or small values of R containing only a flamelet segment and hence are discarded from the figure. Only those flamelet cases are retained with $\max(\xi) > 0.98$ and $\min(\xi) < 0.02$ in the opposed jet burner to cover almost the whole mixture fraction space. The range of R for the retained flamelet in the non-reacting opposed jet burner is between $[0.2, 6.5]$. For the Tsuji burner, we see that the predicted $\xi|_{z=0}$ is about 0.5 when R is around $0.1 < R < 10$. Further increasing R or decreasing R causes $\xi|_{z=0}$ to shift swiftly from 0.5 to the boundary at $\xi|_{z=0} = 1$ for $R < 1$ and at $\xi|_{z=0}$ for $R > 1$. When R is sufficiently small or large, $\xi|_{z=0}$ approaches its limit values $\lim_{R \rightarrow 0} \xi|_{z=0} = 1$ and $\lim_{R \rightarrow \infty} \xi|_{z=0} = 0$. When the strain rate a_s is decreased, the size of the region with $\xi|_{z=0} \approx 0.5$ shrinks and $\xi|_{z=0}$ reaches the boundary value at smaller R when $R > 1$ or at larger R when $R <$

1. The strain rate a_s is seen again to be unable to characterize the DMD in laminar flamelet since the strain rate a_s is kept constant in each case.

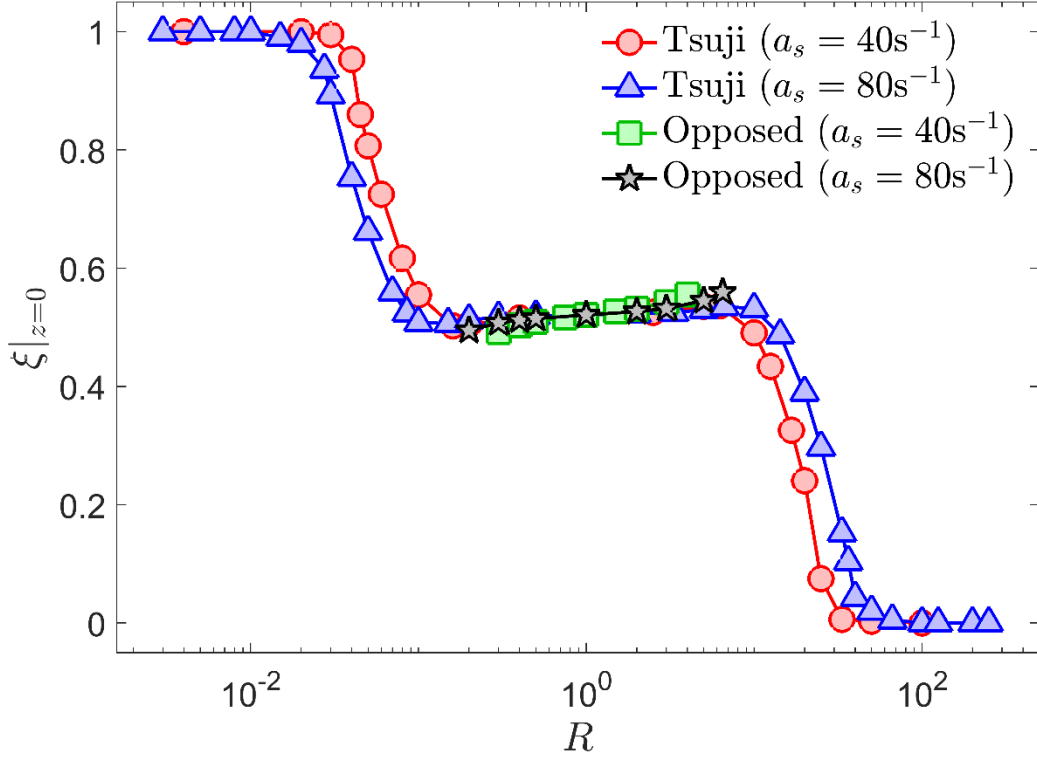


Figure 2.9. Variation of the predicted $\xi_c|_{z=0}$ against the velocity ratio R in non-reacting opposed jet burners and Tsuji burners for two different strain rates $a_s = 40 \text{ s}^{-1}$ and 80 s^{-1} .

Overall, the generalized non-reacting Tsuji burner can generate a smooth and continuous variation of $\xi|_{z=0}$ in the whole mixture fraction space. In contrast, in the non-reacting opposed jet burner cases in Figure 2.9, the variation of $\xi|_{z=0}$ is limited within a small range around 0.5, and the different strain rates do not yield different results of $\xi|_{z=0}$.

Reacting cases of Tsuji burner

Next, we consider reacting cases for the opposed jet burner and Tsuji burner to examine further the effect of the variation of R on the flamelet predictions. The predicted profiles of z in

the mixture fraction space in both burners in the reacting cases shown in Figure 2.10 are qualitatively similar to those in the non-reacting cases in Figure 2.8.

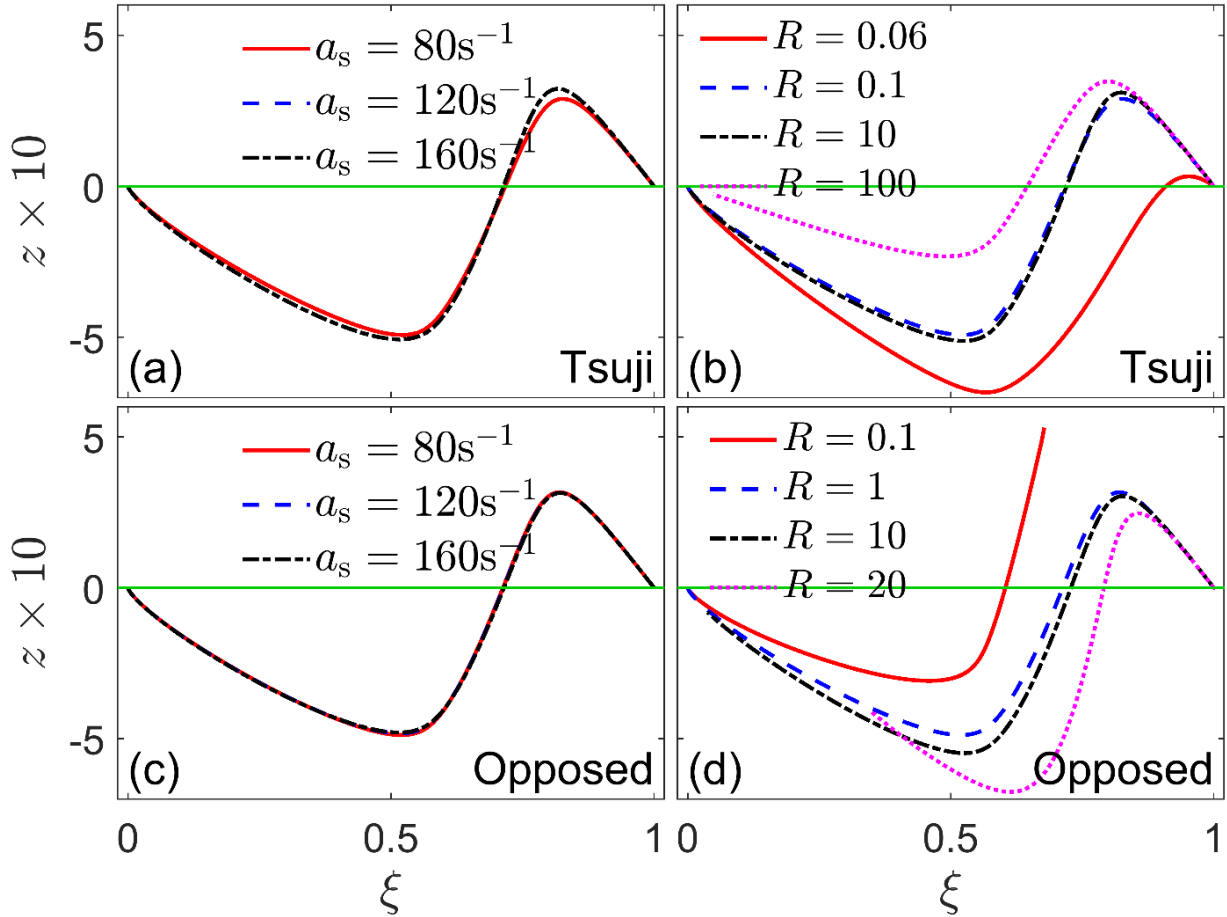


Figure 2.10. Comparison of the profiles of z against the mixture fraction ξ in the reacting Tsuji burner (first row) and reacting opposed jet burner (second row). The left plots show the results under different strain rates a_s , and the right plots show the results under the same strain rate $a_s = 80 \text{ s}^{-1}$ but with different R .

Figure 2.11 shows the predicted equal diffusion location $\xi|_{z=0}$ against R in both the reacting opposed jet burner and the reacting Tsuji burner for two different strain rates $a_s = 40 \text{ s}^{-1}$ and 80 s^{-1} . The wide variation of the location $\xi|_{z=0}$ observed in the non-reacting Tsuji burner in Figure 3.3 is generally also observed in the reacting Tsuji burner. The variation, however, is limited to $\xi|_{z=0} \in (0.6, 1]$ in the reacting Tsuji burner, with the lower bound around $\xi|_{z=0} = 0.6$ which is close

to the stoichiometric mixture fraction $\xi_{st} = 0.539$ for the considered H₂/CO₂/Air combustion. The flame front of the considered fuel is near the stoichiometric condition. When the flame is pushed towards the oxidizer side when $R > 1$, it becomes a barrier to allow $\xi|_{z=0}$ to decrease further since the flame front is always near ξ_{st} . In non-reacting Tsuji cases, there is no such barrier and $\xi|_{z=0}$ can decrease to zero when $R \gg 1$. When it is near $R = 1$, $\xi|_{z=0} \approx 0.7$ in the reacting Tsuji burner, and when $R > 10$ or $R < 0.1$, $\xi|_{z=0}$ starts to decrease or increase to the boundary value or the stoichiometric value. When the strain rate decreases, the size of the region where $\xi|_{z=0} \approx 0.7$ shrinks in the Tsuji burner. The reacting opposed jet burner cannot yield a significant variation of $\xi|_{z=0}$ in the mixture fraction space without disrupting the integrity of the produced laminar flamelet. The different strain rates do not lead to very different results of $\xi|_{z=0}$ for the reacting opposed jet burner cases.

In summary, a significant difference between the opposed jet burner and the Tsuji burner is discovered under significantly different fuel and oxidizer inflow velocities. The generalized Tsuji burner is able to yield a complete laminar flamelet structure with a continuous variation of the equal diffusion location $\xi|_{z=0}$ when the velocity ratio R changes. This variation of $\xi|_{z=0}$ covers the whole mixture fraction space in non-reacting cases. In the reacting cases, the stoichiometric condition at ξ_{st} puts a barrier to the variation of $\xi|_{z=0}$ in the mixture fraction space. The opposed jet burner yields a segment of laminar flamelet when R is far away from unity. To maintain a whole flamelet structure, the variation of R in the opposed jet burner is very limited. Hence, the variation of R is much smaller than that in the Tsuji burner. The wide variation of $\xi|_{z=0}$ observed in the Tsuji burner cannot be produced by solely varying the strain rate a_s , indicating the inadequacy of using a_s as the sole identifier for each flamelet with the effect of DMD. Another parameter like R is needed. The variation of $\xi|_{z=0}$ has been used as an important feature of laminar flamelet that can represent the effect of DMD. This feature is demonstrated to be relevant to practical flames, as discussed in Chapter 3 below.

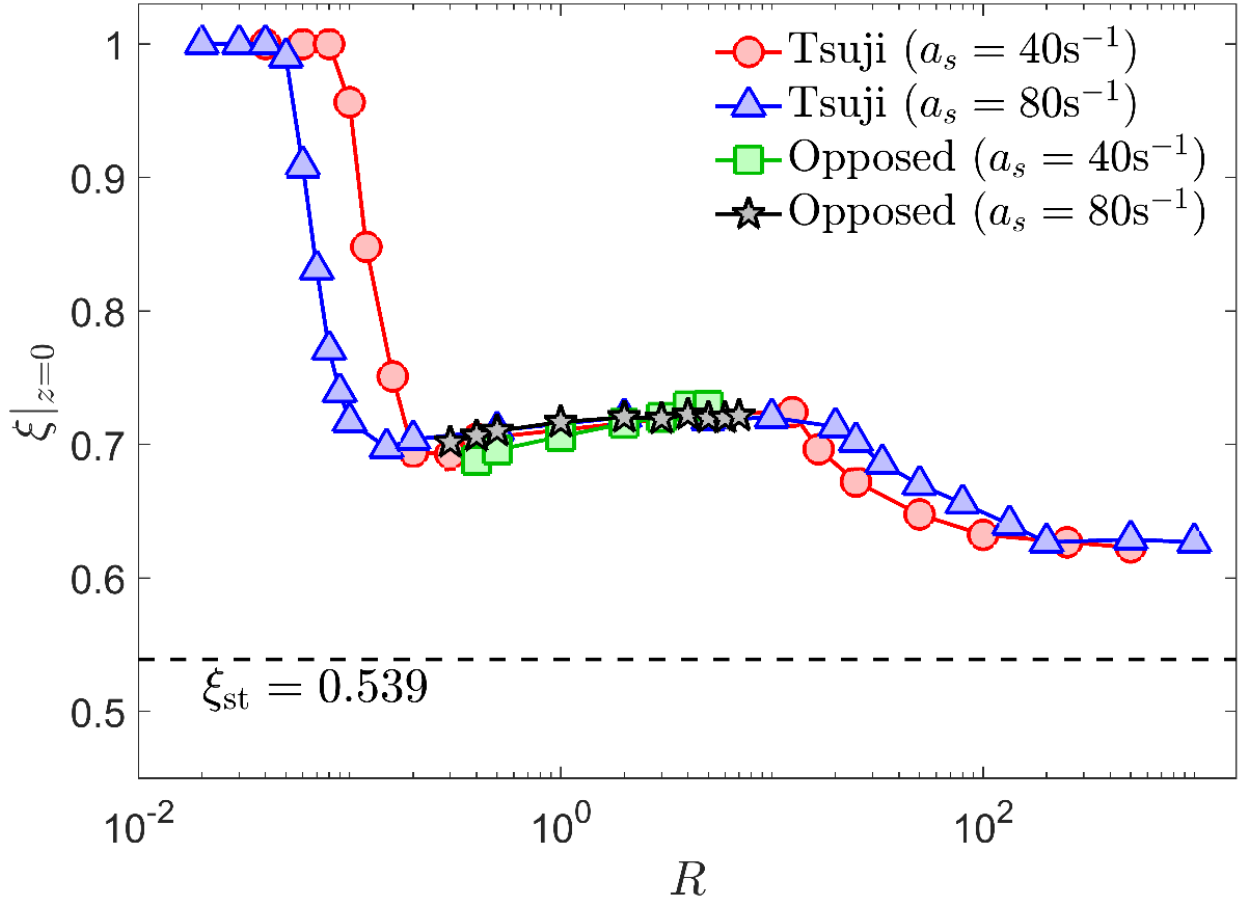


Figure 2.11. Variation of the predicted $\xi|_{z=0}$ against the velocity ratio R in reacting opposed jet burners and Tsuji burners for two different strain rates $a_s = 40 \text{ s}^{-1}$ and 80 s^{-1} .

2.5 Analysis and parametric studies of the opposed jet mixing layer

A detailed analysis of the opposed jet mixing layer is presented in this section. A significant observation of the difference between the opposed jet burner and the Tsuji burner made in Section 2.4 is that the Tsuji burner is able to yield a complete laminar flamelet structure with a continuous variation of the equal diffusion location $\xi|_{z=0}$ when the velocity ratio R changes. This shift of $\xi|_{z=0}$ can be done easily by tuning the velocity ratio R as demonstrated in Section 2.4. It is difficult to achieve variation of R in the traditionally opposed jet burner while maintaining a whole flamelet structure. We conduct an analysis to identify the source of this difficulty. Modifications are introduced to the opposed jet burner to reconcile these two different burners in their generalized

versions to achieve equivalent representativity of laminar flamelet for DMD. A theoretical analysis of an idealized opposed jet mixing layer is conducted first in Section 2.5.1.

2.5.1 Unconstrained opposed jet mixing layer

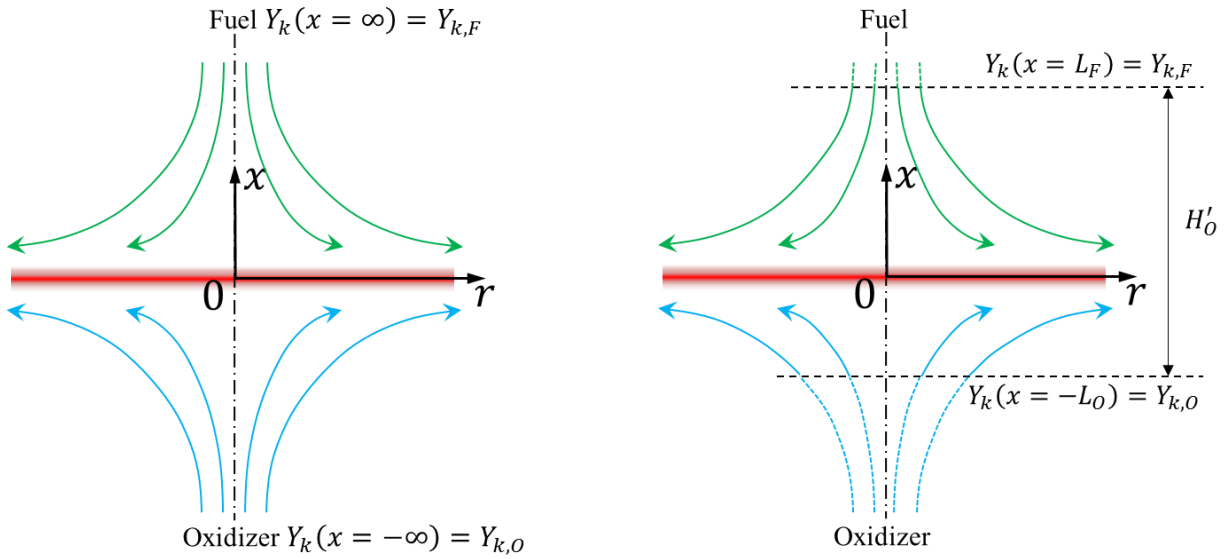


Figure 2.12. An idealized laminar opposed jet mixing layer (left: infinitely distance of the two sources of jets; right: finite distance between the two sources of jets).

An idealized opposed jet mixing layer is adopted here for theoretical analysis, as shown in Figure 2.12. The idealized case is a simplification of the more realistic case in Figure 2.6. The simplification allows an analytical solution to the problem, which helps the analysis. When assuming steady-state and constant properties, including density, based on the potential theory, the axial velocity $u(x)$ can be written analytically as

$$u(x) = -a_s x. \quad (2.18)$$

The governing equations for the species mass fractions Y_k ($k = 1, \dots, N_s$ where N_s is the number of species in the mixing layer) are

$$u(x) \frac{dY_k}{dx} = \Gamma_k \frac{d^2 Y_k}{dx^2}, \quad (2.19)$$

where Γ_k is the molecular diffusivity, which is assumed to be a constant. Substituting Equation (2.19) to Equation (2.18), we obtain

$$x \frac{dY_k}{dx} + \frac{T_k^2}{2} \frac{d^2Y_k}{dx^2} = 0, \quad (2.20)$$

where $T_k = \sqrt{2\Gamma_k / a_s}$ and is interpreted as a characteristic thickness of the mixing layer. With property boundary conditions, Equation (2.20) can be solved analytically. Two different boundary conditions are considered below.

The first boundary condition considers an unconstrained opposed jet burner with free mixing of the fuel and oxidizer placed infinitely apart, as illustrated in Figure 2.12 (left), and the pure fuel and oxidizer boundary conditions are observed only at $x = \pm\infty$ as

$$Y_k(x = -\infty) = Y_{k,O}, \quad Y_k(x = \infty) = Y_{k,F}, \quad (2.21)$$

which is similar to the boundary condition in Equation (2.8) with $L_F = L_O = \infty$. With this boundary condition, the analytical solution to Equation (2.20) is readily obtained as

$$Y_k(x) = \frac{Y_{k,F} - Y_{k,O}}{2} \left[1 + \operatorname{erf} \left(\frac{x}{T_k} \right) \right] + Y_{k,O}, \quad (2.22)$$

where $\operatorname{erf}(\cdot)$ is the error function.

To easily interpret the analytical solution, we specify the fuel and oxidizer in the idealized mixing layer case as the same as those in the opposed jet burner and Tsuji burner in Section 2.3, i.e., fuel with 36% H₂ and 64% CO₂ by volume and the air as the oxidizer with 21% O₂ and 79% N₂ by volume.

The molecular diffusivities of H₂, CO₂, O₂, and N₂ are specified as $\Gamma_{H_2} = 0.78 \times 10^{-4} \text{ m}^2 / \text{ s}$, $\Gamma_{CO_2} = 0.15 \times 10^{-4} \text{ m}^2 / \text{ s}$, $\Gamma_{O_2} = 0.21 \times 10^{-4} \text{ m}^2 / \text{ s}$, and $\Gamma_{N_2} = 0.20 \times 10^{-4} \text{ m}^2 / \text{ s}$. These values are approximated from a FLUENT simulation of a mixing layer with the same fuel and oxidizer. The exact values of the molecular diffusivity are not important for the current examination of the analytical solution in Equation (2.22) as long as they are different to yield DMD. The strain rate is chosen to be $a_s = 40 \text{ s}^{-1}$. The resulted values of the mixing layer thickness $T_k = \sqrt{2\Gamma_k / a_s}$ are $T_{H_2} = 0.0020 \text{ m}$, $T_{CO_2} = 8.6603 \times 10^{-4} \text{ m}$, $T_{O_2} = 0.0010 \text{ m}$, and $T_{N_2} = 0.0010 \text{ m}$. From the analytical solution in Equation (2.22), we can readily determine the mixing fractions ξ_H , ξ_C , and

ξ by following Equation (2.13) and Equation (2.15). The DMD parameter z is obtained based on its definition in Equation (2.14)

$$z = \xi_H - \xi_C = \frac{1}{2} \operatorname{erf} \left(\sqrt{\frac{\Gamma_{\text{CO}_2}}{\Gamma_{\text{H}_2}}} \operatorname{erf}^{-1}(2\xi_C - 1) \right) - \xi_C + \frac{1}{2}, \quad (2.23)$$

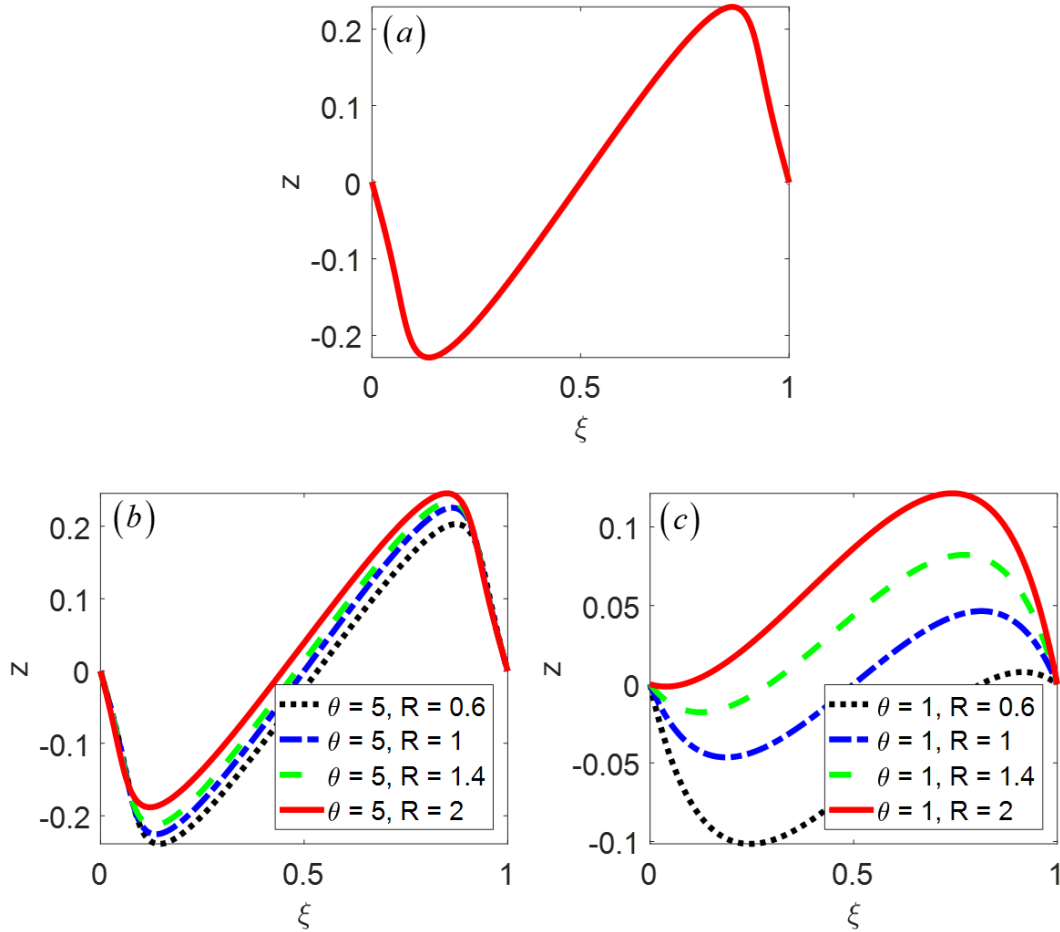


Figure 2.13. The profiles of z against ξ in the idealized laminar opposed jet mixing layer with $a_s = 40 \text{ s}^{-1}$; (a) unconstrained opposed jet mixing layer with an infinite distance between the two sources of jets (equivalent to the constrained opposed jet mixing layer with $\theta = \infty$), (b) constrained opposed jet mixing layer with a finite distance between the two sources of jets with $\theta = 5$, (c) constrained opposed jet mixing layer with a finite distance between the two sources of jets with $\theta = 1$.

The variation of z against ξ for the unconstrained opposed jet mixing layer with an infinite distance between the two sources of jets is depicted in Figure 2.13 (a). Two important observations are made from the analytical solution for z .

- First, the DMD parameter z is independent of the strain rate a_s . Although the result shown in Figure 2.13 (a) is for a specific strain rate $a_s = 40 \text{ s}^{-1}$, it is the same for any strain rate, which is consistent with the finding of Wang [58].
- Second, the location of $z = 0$ inside the idealized opposed jet mixing layer is always at $\xi|_{z=0} = 0.5$ according to the analytical solution for z . It does not shift when we change the strain rate a_s , which is the only free parameter to change in the idealized case above. It has been mentioned previously that being able to shift the location $\xi|_{z=0}$ is an important feature to seek while developing a representative laminar flamelet for modeling DMD in turbulent combustion. The idealized opposed jet burner is shown to be fundamentally limited to producing this desired feature. Realistic opposed jet burners are expected to have the same limitation because the assumptions and simplifications involved in the idealized opposed jet burner are not expected to alter the fundamental DMD behavior.

2.5.2 Constrained opposed jet mixing layer

The identified limitation of the opposed jet burner above creates a need to seek a new conceptual burner design to represent the laminar flamelet. It is found that a modification to the opposed jet burner can produce the desired result. Which is illustrated here by considering a constrained opposed jet burner with a boundary condition for the idealized opposed jet mixing layer described in Equation (2.20). As illustrated in Figure 2.12 (right), the boundary condition for the constrained opposed jet mixing layer is imposed as,

$$Y_k(x = -L_O) = Y_{k,O}, \quad Y_k(x = L_F) = Y_{k,F}. \quad (2.24)$$

In this case, the molecular diffusion is constrained within $x \in [-L_O, L_F]$ instead of unconstrained diffusion in the infinitely large domain $x \in [-\infty, \infty]$ in Figure 2.12 (left). Which is similar to the boundary condition in Equation (2.8) with $L_F = L_O \neq \infty$. It is important to note that

the new boundary condition in Equation (2.24) is not to alter the physics of molecular diffusion. Instead, it is a conceptual design to yield desired physical behaviors. It may even be possible to realize it in a lab by using porous media for the jet inlet. With this boundary condition, Equation (2.20) is solved analytically to yield,

$$Y_k(x) = (Y_{k,F} - Y_{k,O}) \frac{\operatorname{erf}\left(\frac{x}{T_k}\right) + \operatorname{erf}\left(\frac{L_O}{T_k}\right)}{\operatorname{erf}\left(\frac{L_F}{T_k}\right) + \operatorname{erf}\left(\frac{L_O}{T_k}\right)} + Y_{k,O}. \quad (2.25)$$

When $L_F = L_O = \infty$, the analytical solution above reduces to Equation (2.22). Thus, it can be viewed as a solution to a generalized version of the idealized opposed jet mixing layer (as shown in Figure 2.12, right plot). From the analytical solution in Equation (2.25), we can obtain the different mixture fractions ξ_H , ξ_C , and ξ (defined in Equation (2.13) and Equation (2.15)). The DMD parameter z is then obtained according to Equation (2.14).

To illustrate the results, we specify the distance of the two sources of jets to be

$$H'_0 = L_O + L_F = \theta \times \frac{T_{H_2} + T_{CO_2}}{2} \quad (2.26)$$

in Figure 2.12 (right plot), where θ is a modifiable factor. It is important to specify θ to be on the order of one, so that $H'_0 = L_O + L_F$ is comparable to the thickness of the mixing layer T_k to see the effect of the boundary condition in Equation (2.24). If both L_F and L_O are much greater than the mixing layer thickness, in that case, the molecular diffusion does not have much effect near the boundaries, and the results will be similar to the results based on the unconstrained opposed jet. A default value of $\theta = 1$ is used below if not stated. The effect of θ on DMD will be examined. It is worthwhile to point out that the mixing layer thickness T_k used here is the characteristic thickness of an unconstrained opposed jet mixing layer in Section 2.5.1. When a constrained opposed jet burner is used under the same strain rate, the mixing layer thickness can be shown to be smaller because of the constrained mixing. The strain rate is specified as $a_s = 40 \text{ s}^{-1}$. The velocity ratio R defined in Equation (2.9) is varied in the examination, and R is found to be related to L_F and L_O as

$$R = \frac{V_F}{V_O} = \frac{|u(L_F)|}{|u(-L_O)|} = \frac{|-a_s L_F|}{|-a_s (-L_O)|} = \frac{L_F}{L_O}, \quad (2.27)$$

in which Equation (2.18) is used.

The profiles of z with $\theta = 5$ and 1 under different values of R against ξ is depicted in Figure 2.13 (b) and Figure 2.13 (c). We can make several observations from the figure, including very distinct observations from the results in comparison with the unconstrained case in Figure 2.13 (a).

- First, the constrained opposed jet mixing layer simplifies to the unconstrained one when $\theta = \infty$. This can be seen from the analytical solutions since Equation (2.25) reduces to Equation (2.22) when $L_F = L_O = \infty$. The results under this condition are the same as the results shown in Figure 2.13 (a).
- Second, when θ is finite and decreases, the results for z deviate from each other when R varies. The smaller the value of θ , the larger the deviation of z from each other. This is seen in Figure 2.13 when comparing the results for $\theta = 5$ (Figure 2.13 (b)) and $\theta = 1$ (Figure 2.13 (c)).
- Third, the DMD parameter in the constrained mixing layer depends on the strain rate a_s , as shown that T_{H_2} and T_{CO_2} depends on a_s . This is clearly different from the unconstrained opposed jet case;
- Fourth, the location $\xi|_{z=0}$ inside the idealized opposed jet mixing layer is shifted from the center. This is clearly shown in Figures 2.13 (b) and 2.13 (c). The smaller the value of θ , the larger the shift of $\xi|_{z=0}$ from the center. The results from the constrained opposed jet mixing layer successfully replicate the trend observed in the Tsuji burner case and hence provide a plausible explanation for the differences observed in Section 3.2 between the opposed jet burner and the Tsuji burner when used to represent DMD in laminar flamelet.

It is mentioned above that for the constrained opposed jet mixing layer, z depends on the strain rate a_s , which is different from the unconstrained case in Section 2.5.1. Figure 2.14 further examines this dependence by showing $\xi|_{z=0}$ against R for a case with $\theta = 1$ and with different strain rates. Although z depends on a_s in the constrained mixing layer from the analytical

solution, such a dependence for $\xi|_{z=0}$ is weak since there is no visible difference of $\xi|_{z=0}$ when the different strain rates are used in Figure 2.14. This again shows the limitation of using the strain rate to parameterize laminar flamelet when DMD is concerned.

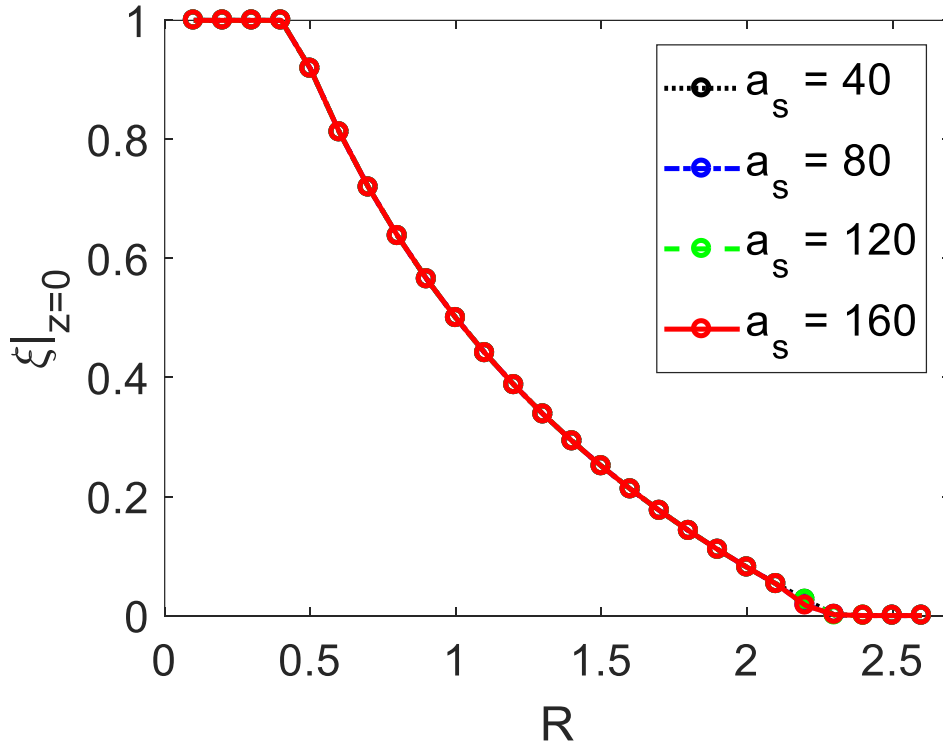


Figure 2.14. The variation of $\xi|_{z=0}$ against R in the constrained opposed jet mixing layer with $\theta = 1$ and with different strain rates, $a_s = 40 \text{ s}^{-1}$, 80 s^{-1} , 120 s^{-1} , and 160 s^{-1} .

The effect of θ (the distance of the two opposed jet sources) on DMD is further examined in Figure 2.15 where the profiles of $\xi|_{z=0}$ are shown against R in the constrained opposed jet mixing layer with different values of θ , 1, 3, 5, 10, and ∞ . The strain rate is fixed at $a_s = 40 \text{ s}^{-1}$. When $\theta \rightarrow \infty$, the constrained opposed jet reverts to the unconstrained one, and the equal diffusion location $\xi|_{z=0}$ is equal to 0.5 identically. When θ becomes a finite value, say $\theta = 10$, $\xi|_{z=0}$ is near 0.5 when R is close to one, e.g., $0.2 < R < 5$, and $\xi|_{z=0}$ deviates from 0.5 when R moves further away from one and eventually reaches the limit $\xi|_{z=0} = 0$ or 1. When the value of θ decreases, the

region of R shrinks for $\xi|_{z=0} \approx 0.5$. For $\theta = 1$, that region shrinks to almost zero. The effect of θ on DMD is clearly seen. The smaller the value of θ , and larger the effect on DMD.

The analysis here is based on a theoretical case that allows an analytical solution. Next, we consider more realistic cases in Chapter 3.

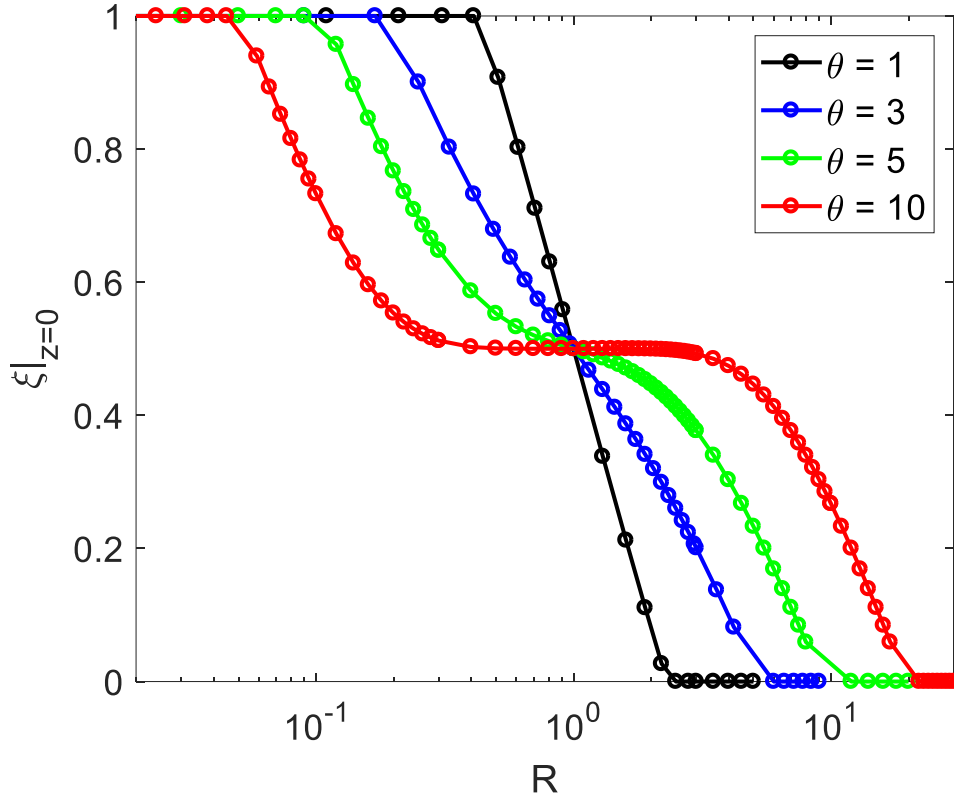


Figure 2.15. the profiles of $\xi|_{z=0}$ against R in the constrained opposed jet mixing layer with the different values of θ under the same strain rate $a_s = 40s^{-1}$.

2.6 Conclusions

In this chapter, the concept and the governing equations of the laminar flamelet model have been introduced. A laboratory-scale hydrogen-air transitional diffusion flame is adopted as a validation test case, and the quantitative presentation of the DMD effect in the diffusion flame has been studied. Two widely used experimental configurations based on the opposed jet burner and the Tsuji burner have been chosen to examine the laminar flamelet's representativity for the DMD

effect. A comparison between the opposed jet burner and the Tsuji burner has been conducted to demonstrate their similarity and difference. A detailed analysis of the constrained and unconstrained opposed jet mixing layer is presented. Based on the comparative study, the following conclusions were drawn:

- 1) Neglecting the DMD effect and assuming equal molecular diffusion coefficients for turbulent non-premixed combustion is inappropriate, considering the DMD effect in flamelet modeling can significantly improve the simulation results.
- 2) The opposed jet burner and the Tsuji burner can be considered equivalent if they are adequately tuned to produce the laminar flamelets with DMD, which fits the general view in the combustion community so far.
- 3) The strain rate a_s cannot fully parameterize the steady laminar flamelet. A second parameter like the fuel and oxidizer flow velocity ratio is needed. The significant difference between the opposed jet burner and the Tsuji burner can be discovered under significantly different fuel and oxidizer inflow velocities.
- 4) The key difference between the opposed jet burner and the Tsuji burner is that the opposed jet burner cannot produce the entire laminar flamelets that feature a variation of $\xi|_{z=0}$ in the mixture fraction like the Tsuji burner. The variation of $\xi|_{z=0}$ is very limited in the opposed jet burner to maintain the integral structure of the laminar flamelet.
- 5) This variation of $\xi|_{z=0}$ covers the whole mixture fraction space in non-reacting cases. However, in the reacting cases, the stoichiometric condition at ξ_{st} puts a barrier to the variation of $\xi|_{z=0}$ in the mixture fraction space.
- 6) The results from the constrained opposed jet mixing layer successfully replicate the trend observed in the Tsuji burner case and hence provide a plausible explanation for the differences observed between the opposed jet burner and the Tsuji burner when used to represent DMD in laminar flamelet.

3. IMPLICATION TO FLAMELET MODELING OF DMD

The studies in Chapter 2 revealed an exciting observation about DMD in laminar flamelets. The equal diffusion location in the mixture fraction space shifts continuously using the generalized Tsuji burner, or the generalized constrained opposed jet burner. That is an important finding of the characteristics of DMD in turbulent non-premixed flames. It is expected to have theoretical value, but is it still valuable practically? This chapter will answer the question by establishing the practical relevance of the above observation.

Several laboratory-scale jet flow and jet flame configurations will be explored to examine the DMD characteristics and the difference between them and those observed in laminar flamelet based on the Tsuji burner or the opposed jet burner. Canonical jet flows and flames illustrated in Figure 3.1 are an abstraction of many practical combustion problems like gas turbine or diesel engines.

In this chapter, we analyze three jet flow and flame configurations in terms of DMD to show an implication of the difference observed between the opposed jet burner and the Tsuji burner in Chapter 2 for the generation of representative laminar flamelet with the effect of DMD. Section 3.1 examines the DMD in a laminar round jet non-reacting mixing layer through a simulation study. Section 3.2 explores the DMD in a turbulent round jet non-reacting mixing layer by using the available experimental data. Section 3.3 studies the DMD in a turbulent round jet flame by using the available experimental data.

Different Reynolds numbers are considered for the detailed comparison. The Reynolds number for a jet flow or jet flame is defined as

$$\text{Re} = \frac{U_J D_J}{\nu}, \quad (3.1)$$

where ν is the kinematic viscosity, U_J is the bulk jet velocity (see Figure 4.1), and D_J is the jet diameter.

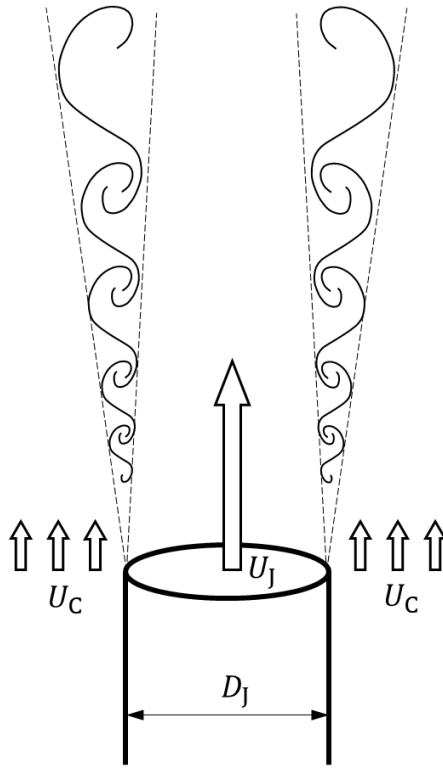


Figure 3.1. Schematic diagram of a jet flow or jet flame configuration.

A simple jet flow is used to study flamelet implementation in calculating differential diffusion effects. As shown in Figure 3.2, the round tube in the computational domain has a 7.7 mm inner diameter, and the fuel comes from it. The center of the fuel inlet locates at $y = 0$ in Figure 3.2. The simulations only calculate half the physical domain to reduce the computational cost. The calculations are performed on a two-dimensional mesh; the whole computational region is $10 D_J \times 35 D_J$, and rectangular grids are used in the numerical calculation region. Uniform inflow is imposed on both the fuel and co-flow oxidizer jets. The bottom side is a symmetric boundary, and the top and left sides are set as pressure outlets. A schematic diagram of H_2 mass fractions distribution is plotted in Figure 3.2.

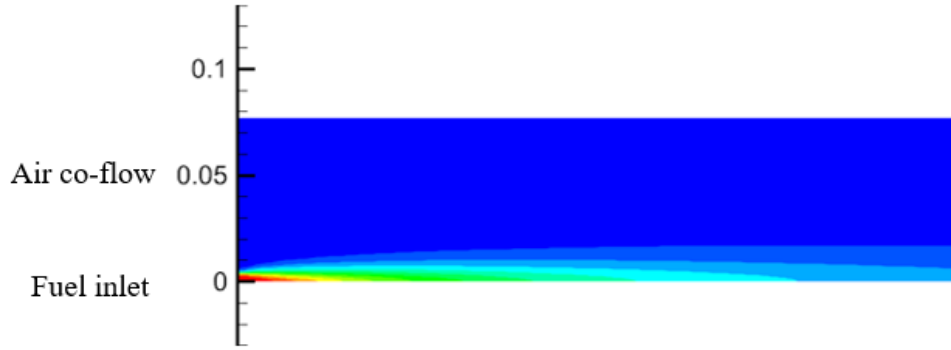


Figure 3.2. Schematic diagram of H₂ mass fractions distribution in the calculation region.

The concentration ratios of H₂ versus CO₂ in the jet center at three different axial locations, $5 D_j$, $15 D_j$, and $30 D_j$, are extracted from the simulation. These calculation data will be used to check the validation of different kinds of laminar flamelet models. As mentioned in Section 2.3, two approaches to generating the laminar flamelet model are used for generating the laminar flamelet. One integration uses the Tsuji burner that disables the inlet diffusion effect and has large velocity differences between the fuel and oxidizer flow; another integration uses the opposed jet burner with equal velocities for the fuel and air jets to stabilize the mixing layer in the center. These flamelet integration approaches will be tested by comparing them with the experimental data.

3.1 Pure mixing in the laminar jet flow

We first consider pure mixing (non-reacting) in a laminar round free jet flow. As mentioned above, the jet diameter $D_j = 7.7 \times 10^{-3}$ m, and the co-flow air speed is $U_c = 1 \times 10^{-2}$ m. The fuel is the same as in Section 2.3 (36% H₂ and 64% CO₂ by volume), and its velocity is adjusted to obtain different values of Re. Low Reynolds number flows with $Re = 2 \times 10^2$, 4×10^2 , 6×10^2 , and 8×10^2 are considered so that the flow remains laminar. Two-dimensional axisymmetric simulations are conducted with a domain size of $[0, 35 D_j] \times [0, 10 D_j]$ in the axial and radial directions, respectively. A total of 15,000 grid cells are used, and ANSYS FLUENT is used for the simulations.

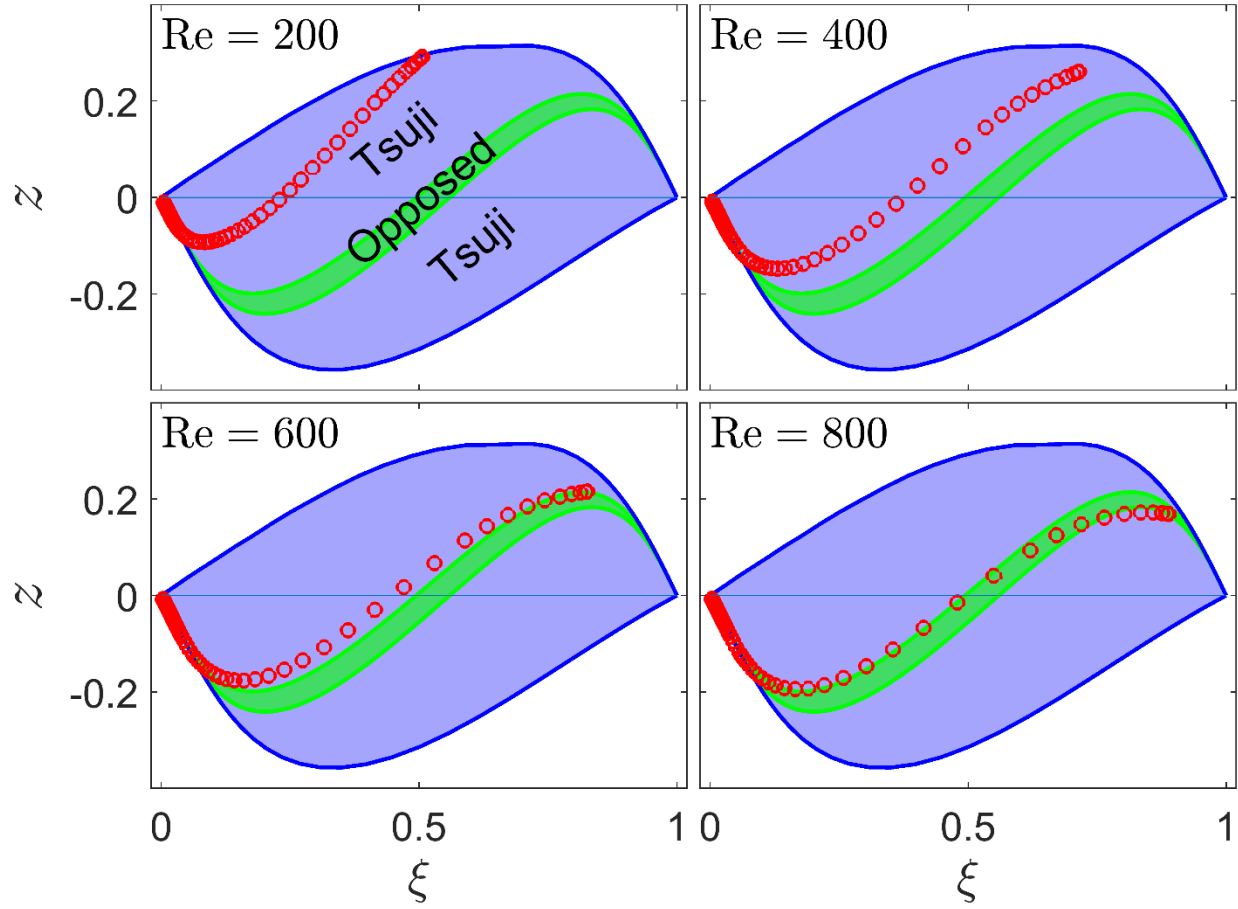


Figure 3.3. Comparison of the profiles of z against ξ at $x/D_j = 10$ in a laminar jet flow under different Reynolds numbers $Re = 2 \times 10^2$, 4×10^2 , 6×10^2 , and 8×10^2 with the laminar flamelet results obtained in the non-reacting opposed jet burner and the Tsuji burner with the same strain rate $a_s = 80 \text{ s}^{-1}$ and different ranges of R , $R \in [10^{-2}, 10^3]$ for the Tsuji burner and $R \in [0.2, 6.5]$ for the opposed jet burner. The circles are the simulation results in the laminar jet flow, and the differently shaded regions cover the considered laminar flamelet solutions from the different burners.

Figure 3.3 shows the comparison of the DMD parameter z against ξ at $x/D_j = 10$ in the laminar jet with the laminar flamelet results obtained from the opposed jet burner and the Tsuji burner. Although the case is non-reacting, we still call it flamelet since the underlying concept is the same. The laminar flamelet results are shown as shaded regions covering all the flamelet

profiles with the strain rate $a_s = 80 \text{ s}^{-1}$ and $R \in [10^{-2}, 10^3]$ for the Tsuji burner and $R \in [0.2, 6.5]$ for the opposed jet burner.

For the opposed jet burner, the flamelet profiles that do not cover the whole mixture fraction space are discarded. The variation of the equation diffusion location $\xi|_{z=0}$ in the opposed jet laminar flamelet is limited to a small range $\xi|_{z=0} \in [0.495, 0.559]$. In the generalized Tsuji burner, the variation of $\xi|_{z=0}$ covers the whole mixture fraction space. That is the main difference observed in Section 2.4 between the two burners.

In the laminar jet mixing layer in Figure 3.3, we see that the equal diffusion location $\xi|_{z=0}$ at $x/D_j = 10$ varies significantly between $\xi|_{z=0} = 0.29$ when $\text{Re} = 2 \times 10^2$ and $\xi|_{z=0} = 0.49$ when $\text{Re} = 8 \times 10^2$. This variation is similar to the laminar flamelet profiles obtained from the Tsuji burner. The results of the laminar jet in Figure 3.3 are indeed fully covered by the shaded area formed by the laminar flamelet results obtained from the Tsuji burner. That means the laminar flamelet profiles obtained from the Tsuji burner can qualitatively represent the effect of DMD in the jet flow mixing. On the other hand, the opposed jet burner produces flamelet profiles that fail to cover the jet flow results and thus cannot represent the effect of DMD in the jet flow mixing.

In summary, the continuous variation of the equal diffusion location $\xi|_{z=0}$ in the mixture fraction space is observed to be an important feature of DMD in pure mixing laminar jet flows. The findings of the difference between the opposed jet burner and the Tsuji burner in Section 2.4 thus have significance to practically relevant flows.

3.2 Pure mixing in the turbulent jet flow

Pure mixing in a turbulent jet flow is considered next, and the experimental data measured by Smith et al. [50] are used for the analysis. The turbulent jet experiment uses the same fuel and burner as in the laminar jet in Section 3.1. The jet bulk velocity U_j varies from 1.7 m/s to 108 m/s to yield four different cases with $\text{Re} = 1 \times 10^3$, 4×10^3 , 16×10^3 , and 64×10^3 . The co-flow air velocity is $U_c = 1.5 \text{ m/s}$.

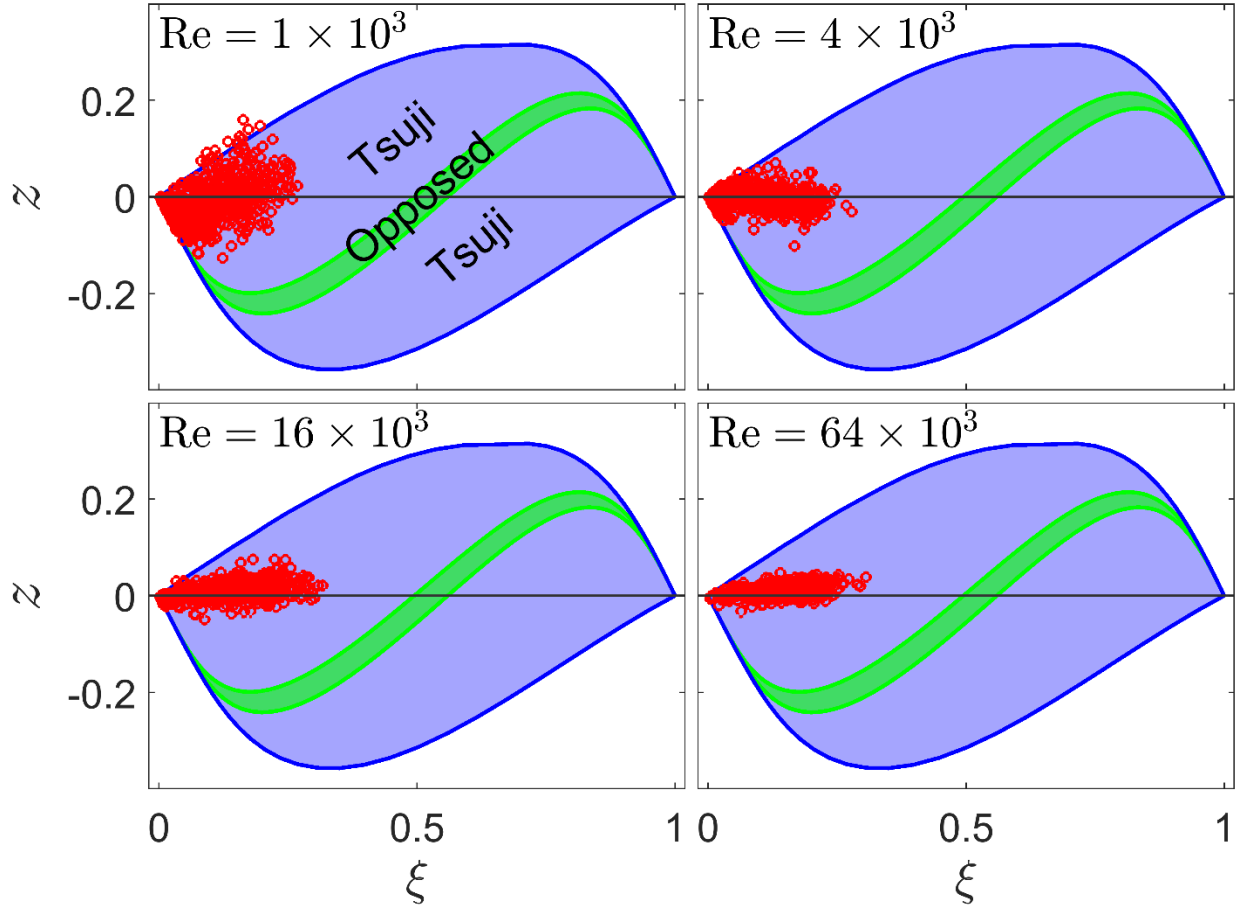


Figure 3.4. Comparison of the profiles of z against ξ at $x/D_j = 30$ in a turbulent jet flow [10] under different Reynolds numbers $Re = 1 \times 10^3$, 4×10^3 , 16×10^3 , and 64×10^3 with the laminar flamelet results obtained in the non-reacting opposed jet burner and the Tsuji burner with the same strain rate $a_s = 80 \text{ s}^{-1}$ and different ranges of R , $R \in [10^{-2}, 10^3]$ for the Tsuji burner and $R \in [0.2, 6.5]$ for the opposed jet burner. The circles are the experimental data in the turbulent jet flow [50], and the differently shaded regions cover the considered laminar flamelet solutions from the different burners.

Figure 3.4 shows the comparison of the measured instantaneous z against ξ at $x/D_j = 30$ in the turbulent jet [50] with the laminar flamelet results obtained from the opposed jet burner and the Tsuji burner. The flamelet results shown in the figure are the same as those in Figure 3.3. The measured results of z in the different turbulent jet flows with the different Reynolds numbers are clustered near the oxidizer side with $\xi < 0.35$. The magnitude of the measured z decreases as Re increases, which is consistent with the theoretical results [18]. The measurement results are mainly

outside the shaded area covered by the opposed jet laminar flamelet results, while they are almost entirely covered by the Tsuji burner laminar flamelet results. The limitation of the opposed jet burner for laminar flamelet generation to represent DMD in a laminar jet in Section 3.1 is also observed here in the pure mixing in a turbulent jet flow. The Tsuji burner is expected to be able to yield a representative laminar flamelet that can potentially characterize the DMD effect in a turbulent jet mixing case.

3.3 Turbulent jet non-premixed flame

A turbulent jet non-premixed flame is considered to examine further the similarity and difference of the effect of DMD in a turbulent flame and in the laminar flamelet results produced in the opposed jet burner and the Tsuji burner. The experimental data measured by Smith et al. [51] are used for the analysis.

The jet configuration in the turbulent jet flame case is the same as that in the turbulent jet flow case in Section 3.2, like the fuel composition, jet diameter, and co-flow velocity. Simultaneous point measurements of the concentrations of major species, N₂, O₂, H₂, H₂O, CO₂, and CO, are made in the experiment to calculate ξ and z . Four Reynolds number cases with $Re = 2 \times 10^3, 4 \times 10^3, 8 \times 10^3, \text{ and } 16 \times 10^3$ are considered.

Figure 3.5 shows the comparison of the measured instantaneous z against ξ at $x/D_j = 30$ in the turbulent jet flame [51] with the laminar flamelet results obtained from the opposed jet burner and the Tsuji burner. The laminar flamelet results are shown as shaded regions covering all the flamelet profiles with the strain rate $a_s = 80 \text{ s}^{-1}$ and $R \in [5 \times 10^{-2}, 10^3]$ for the Tsuji burner and $R \in [0.2, 4]$ for the opposed jet burner.

For the opposed jet burner, the flamelet profiles that do not cover the whole mixture fraction space are discarded. The variation of the equation diffusion location $\xi|_{z=0}$ in the opposed jet laminar flamelet is limited to a narrow range $\xi|_{z=0} \in [0.681, 0.697]$. In the generalized Tsuji burner, the variation of $\xi|_{z=0}$ covers the range $\xi|_{z=0} \in (0.6, 1]$. That is the main difference observed in Section 2.4 between the two burners. In the turbulent jet flame case, we see that the experimental data are outside of both shaded regions covered by the flamelet results from both burners. This

observation is inconsistent with those in the pure mixing cases in Sections 3.1 and 3.2. Two possible reasons can explain the discrepancy.

The first reason is the experimental uncertainty involved in the measurement data. The experiment data were obtained in the 1990s, and the accuracy in the measurement of species concentrations is generally expected to be limited. New experiments with higher measurement accuracy are needed to confirm the existing measurement data. The second possibility is the limitation of the used laminar flamelet. Two important assumptions are involved in the flamelet results discussed above: steady-state and no flame extinction. Both assumptions are highly questionable in turbulent flames, especially those with high Re and low Damköhler numbers. Chao and Wang [59] showed the importance of the unsteady effect on DMD modeling. Local extinction in turbulent non-premixed jet flame is generally expected.

To examine the effect of the two assumptions, we purposely extinguish the laminar flamelet in the Tsuji burner (by disabling the chemical reaction) and conduct transient simulations to collect the flamelet results during the extinction process. The steady flamelet solution with $R = 10^3$ and $a_s = 80 \text{ s}^{-1}$ is used as the initial condition. The transient laminar flamelet results are shown in Figure 3.5 as the shaded region labeled as “Transient”. A fundamental difference in the added flamelet results is that the equal diffusion location $\xi|_{z=0}$ can now move to the oxidizer side, which is impossible for the steady burning flamelet. The measured z is now mostly covered by the flamelet results obtained in the Tsuji burner after the unsteadiness and extinction are taken into consideration. For the opposed jet burner, the consideration of unsteadiness and extinction does not extend the existing region covered by the burning flamelet much (results not shown), and hence the measured z is still outside of the region. The chemical reaction is seen to complicate the effect of DMD in turbulent flames. Hence, additional considerations are needed to generate a representative flamelet for modeling DMD in turbulent non-premixed flames. Using the Tsuji burner and considering unsteadiness and extinction seems promising to reproduce the characteristics of DMD in turbulent non-premixed flames. The opposed jet burner is on the other hand limited in that regard.

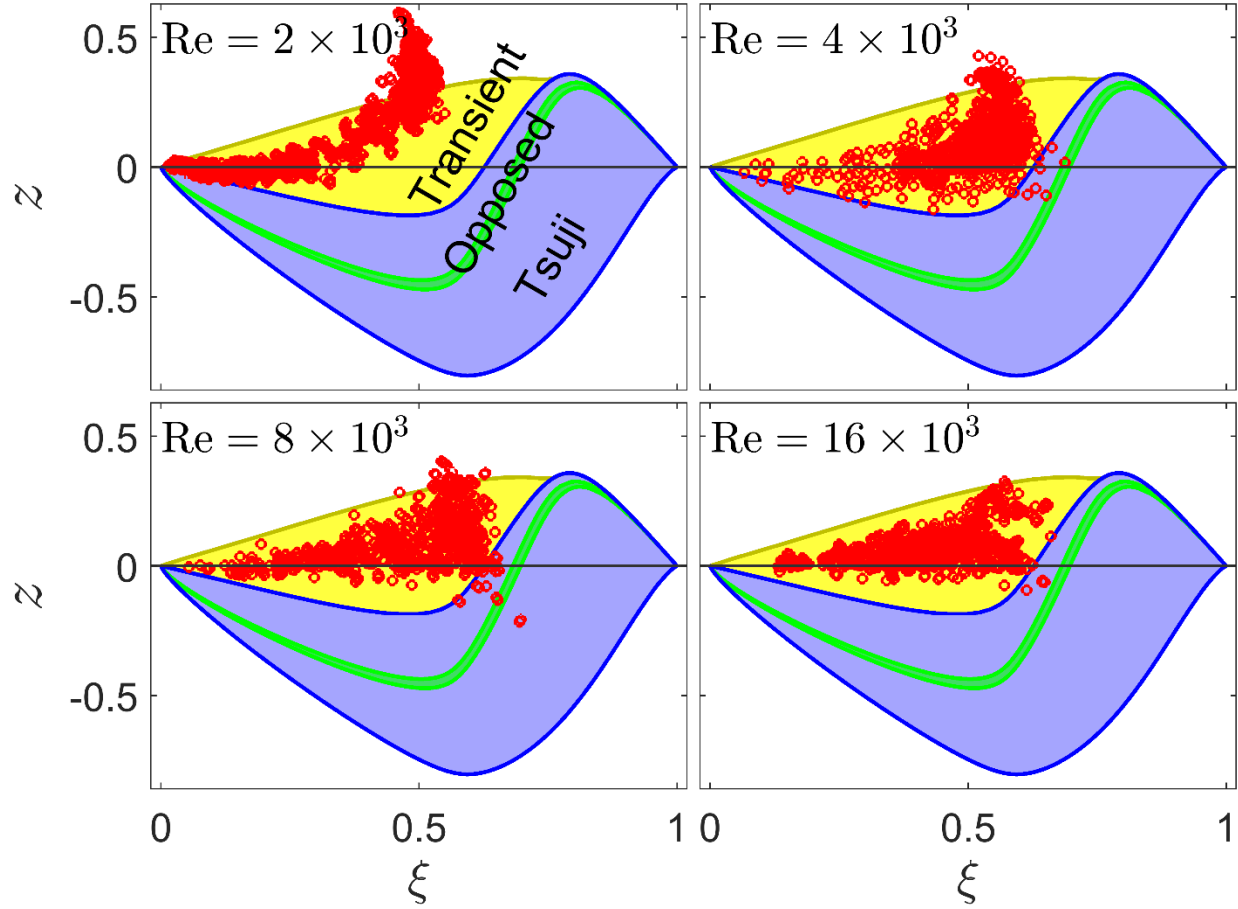


Figure 3.5. Comparison of the profiles of z against ξ at $x/D_j = 30$ in a turbulent jet flame [11] under different Reynolds numbers $Re = 2 \times 10^3$, 4×10^3 , 8×10^3 , and 16×10^3 with the laminar flamelet results obtained in the reacting opposed jet burner and the Tsuji burner with the same strain rate $a_s = 80 \text{ s}^{-1}$ and different ranges of R , $R \in [5 \times 10^{-2}, 10^3]$ for the Tsuji burner and $R \in [0.2, 4]$ for the opposed jet burner. The circles are the experimental data in the turbulent jet flame [10], and the differently shaded regions cover the considered steady laminar flamelet solutions from the different burners as well as the transient flamelet solutions in the Tsuji burner.

3.4 Conclusions

In this chapter, a laminar round jet non-reacting mixing layer, a turbulent round jet non-reacting mixing layer, and a turbulent round jet flame with available experimental data have been used to demonstrate further the representativity of the Tsuji burner laminar flamelet as well as the

limitation of the opposed jet laminar flamelet. Based on the comparative study, the following conclusions were drawn:

- 1) For the pure mixing in the laminar jet flow, the laminar flamelet profiles obtained from the Tsuji burner can qualitatively represent the effect of DMD. In contrast, the opposed jet burner produces flamelet profiles that cannot represent the effect of DMD in the jet flow mixing.
- 2) For the pure mixing in a turbulent jet flow, the limitation of the opposed jet burner for laminar flamelet generation to represent DMD is also observed. The Tsuji burner has a much greater potential to yield a representative laminar flamelet that can potentially characterize the DMD effect in a turbulent jet mixing case.
- 3) For the turbulent jet flame, additional considerations like the effect of unsteadiness and extinction are found to be needed to accompany the Tsuji burner to produce a representative flamelet for the effect of DMD. These findings are important to developing flamelet models that predict DMD in turbulent non-premixed flames.

4. TRANSPORTED PDF MODELING OF A POOL FIRE

Chapter 2 and Chapter 3 focus on the representativity of laminar flamelet for jet mixing layers and jet flows. These jet flames are basically momentum dominated and have a cylindrical form. On the other hand, the pool fire is another kind of low-strain, buoyancy-controlled diffusion flame. The size of a pool fire usually has tens of centimeters of fuel port, and the flame height has an order of meters; the pool fire's flame region is relatively larger than lab-scale jet flames.

Due to the limitation of computer power, the previous investigations generally used highly simplified chemical mechanisms such as the 1-step or 2-step combustion mechanism. They also used low order or highly simplified turbulence and combustion models such as the eddy dissipation concept (EDC) or the eddy dissipation model (EDM). Thus, developing and enhancing the predictive capabilities of fire models is critical.

Capturing fire extinction limits in simulations is important for developing models for fire. In this chapter, The NIST Fire Dynamics Simulator (FDS) code for LES is combined with an in-house PDF code called HPDF for the fire simulations. The University of Maryland line burner is adopted as a validation test case, and the simulation results are compared and validated by using the experimental data. The pool fire has been studied mostly using highly simplified models; the detailed physics cannot be accurately captured. The transported PDF model is a high ordering model and is suitable to solve the problems that need to consider detailed chemical reactions; it has a significant advantage for resolving chemical composition in reacting flows and can couple with other models.

4.1 Transported PDF model

An in-house high-performance PDF code, called HPDF [60], has been developed to combine with an existing LES code. The HPDF model has been used to study the DLR Flame A, which uses CH₄/H₂/N₂ as fuel and generates a turbulent jet flame. A comparison with the experimental measurement proved the validation of the LES/PDF model.

For the composition PDF method, a composition space $\Phi = f(\phi_1, \phi_2, \dots, \phi_n)$ has been defined for n components; the scalar ϕ contains the enthalpy of the combustion fields and the mass fractions of all species. Then the sample space variable distribution at the spatial location x

and the time t has been shown by using the function $f(\psi; \mathbf{x}, t)$; the variable ψ in the function means the sample space variable corresponding to the composition scalar $\phi(\psi = (\psi_1, \psi_2, \dots, \psi_n))$, and the function $f(\psi; \mathbf{x}, t)$ also called the filtered density function or FDF.

When considering a reactive flow system contains a multi-component gas phase with n_ϕ mass fractions, the conservation equation can be derived as

$$\frac{\partial \rho \phi_\alpha}{\partial t} + \nabla \cdot (\rho \mathbf{u} \phi_\alpha) = \nabla \cdot (\rho \Gamma_\alpha \nabla \phi_\alpha) + \rho S_\alpha + C_\alpha, \quad (4.1)$$

where ϕ_α ($\alpha = 1, 2, \dots, n_\phi$) is the mass fraction, Γ_α represents the molecular diffusivity of species α , and S_α is the chemical reaction source term of species α .

The transport equation of the joint composition $f(\psi; \mathbf{x}, t)$ has the following form [63] derived from Equation (4.1)

$$\begin{aligned} \frac{\partial \bar{\rho} f}{\partial t} + \frac{\partial}{\partial x_j} (\bar{\rho} u_j f) + \frac{\partial}{\partial \psi_\alpha} [\bar{\rho} f S_\alpha(\psi)] - \frac{\partial}{\partial x_j} \left(\bar{\rho} \Gamma \frac{\partial f}{\partial x_j} \right) = \\ - \frac{\partial}{\partial x_j} (\bar{\rho} f u_j'' | \psi) - \frac{\partial^2}{\partial \psi_\alpha \psi_\beta} \left[f \left(\overline{\rho \Gamma \frac{\partial \phi_\alpha}{\partial x_j} \frac{\partial \phi_\beta}{\partial x_j} | \psi} \right) \right], \end{aligned} \quad (4.2)$$

where u_j is the velocity, Γ represents the scalar diffusivity, which can be seen as the molecular diffusivity, and S_α represents the chemical reaction source term of species α . When considering equal molecular diffusivity, the Γ can be calculated as

$$\Gamma = \Gamma_0 \left(\frac{\tilde{T}}{T_0} \right)^\alpha, \quad (4.3)$$

the default values are $T_0 = 300 \text{ k}$, $\Gamma_0 = 2.293 \times 10^{-5} \text{ m}^2/\text{s}$ and $\alpha = 1.660$.

The left side of Equation (4.2) has four terms, all of which are closed. These closed chemical reaction terms are the remarkable advantage of the transported PDF model [64]. For the right side of the equation, the first un-closed term represents the scalar flux due to the residual velocity; the gradient diffusion model [7] can be used to deal with it; this term can be transferred as follows

$$- \frac{\partial}{\partial x_j} (\bar{\rho} f u_j'' | \psi) = \frac{\partial}{\partial x_j} \left(\bar{\rho} \Gamma_i \frac{\partial f}{\partial x_j} \right), \quad (4.4)$$

where Γ_t is the turbulent eddy diffusivity, it can be calculated as

$$\overline{\rho}\Gamma_t = \frac{\mu_t}{Sc_t}, \quad (4.5)$$

where μ_t presents the turbulent viscosity, Sc_t is a constant, which represents the turbulent Schmidt number, and the default value of Sc_t equals 0.4.

On the right side of Equation (4.2), the second term is the conditional dissipation term which is un-closed; several mixing models can be used for its closure. That includes the mean mixing (IEM) model [65], the modified Curl model [66], and the EMST model [67]. This study will discuss the comparison between different mixing models in the following sections.

The Lagrangian Monte Carlo particle method [68] is used to resolve the PDF equation shown in Equation (4.2). That's because the traditional finite-volume methods are applicable for solving the equation. The Monte Carlo particle method uses nominal particles for PDF representation. Every particle has various properties, and these properties include the physical location $\mathbf{X}^*(t)$, the compositions of scalar values $\phi^*(t)$, the mass m^* , and other properties such as the diffusivities Γ^* , the velocities $\tilde{u}^*(t)$, and the mixing frequencies Ω^* . The following SDEs (stochastic differential equations) can calculate these properties

$$d\mathbf{X}^*(t) = \left[u_{(x,t)} + \frac{\nabla \left[\overline{\rho} \left(\Gamma_{(x,t)} + \Gamma_{t(x,t)} \right) \right]}{\overline{\rho}} \right] dt + \left[2 \left(\Gamma_{(x,t)} + \Gamma_{t(x,t)} \right) \right]^{\frac{1}{2}} d\mathbf{W}, \quad (4.6)$$

$$\frac{d\phi^*(t)}{dt} = \mathbf{M} \left(\phi^*(t), \Omega_{(x,t)}^* \right) dt + \mathbf{S} \left(\phi^*(t) \right) dt, \quad (4.7)$$

where the superscript “*” represents the parameter at the particle location given by $d\mathbf{X}^*(t)$.

The $d\mathbf{W}$ represents the standard isotropic Wiener process, \mathbf{M} means the mixing term, \mathbf{S} is the chemical reaction source term, and the mixing frequency Ω is calculated as

$$\Omega = \frac{C_\phi (\Gamma + \Gamma_t)}{2\Delta^2}, \quad (4.8)$$

the mixing frequency can be obtained from the interpolation of the data, and the default value of C_ϕ is 3.0. The value of C_ϕ controls the intensity and strength of mixing; the tested results showed

that using the 3.0 default value of C_ϕ having the best agreement with experimental data of flame L [69].

The different values of C_ϕ with different mixing models can cause different extinction limitations of the fire when doing the simulation, and the different values of C_ϕ will be further examined in the following sections. The n th moment in a given cell can be obtained as

$$\tilde{\phi}^n = \frac{\sum_{i=1}^{N_{pc}} m_i^* \phi_i^*}{\sum_{i=1}^{N_{pc}} m_i^*}, \quad (4.9)$$

where N_{pc} represents the number of particles in the given cell, and the ϕ_i^* is the composition value, the m_i^* is i th particle's mass.

4.2 Mixing models implemented in PDF

The in-house HPDF code contains three different mixing models: the IEM model [65], the Modified Curl Model (MCurl model) [66], and the EMST model [67]. A detailed comparison between these three models will be assessed by evaluating these models' capability to capture fire extinction limit in the following sections. The non-premixed and premixed combustion regimes will be used to explain the differences between different models.

As mentioned in Equation (4.7) and Equation (4.8), the mixing for particles in the PDF model is controlled in the term $M(\phi^*(t), \Omega_{(x_i, t)}^*)$, and the mixing frequency Ω determines the mixing intensity. It is important to choose a suitable mixing model that adequately simulates the interaction of turbulence and chemical reaction processes. A stochastic model of turbulent mixing for Reynolds Averaged Navier-Stokes (RANS) based simulations has been developed by Flagan and Appleton [70], and this model is often considered to be the original particle-based turbulent combustion mixing model. With the increased computational power, the hybrid Eulerian/Lagrangian model based on the LES/PDF formulation has now become the preferred choice for turbulence modeling.

4.2.1 Interaction by Exchange with the Mean (IEM) model

The IEM model is the most widely used and simplest model in hybrid Eulerian/Lagrangian simulations. It is also known as Linear Mean Square Estimation (LMSE) model and was developed by Villermaux and Devillon [71]. When applying the IEM model, the composition change of one particle is mainly independent of other particles, and the scalar values of the i th particle can be obtained from the following equation

$$\frac{d\phi^{(i)}}{dt} = -\frac{1}{2} \frac{C_\phi}{\tau} (\phi^{(i)} - \tilde{\phi}), \quad (4.10)$$

where τ is the turbulence time scale, $\phi^{(i)}$ represents the scalar of i th particle, and $\tilde{\phi}$ is the mean (Favre averaged) of ϕ . Generally, the chosen value of C_ϕ may vary with different characteristic length scales of the scalar field. The IEM model may not be suitable for modeling turbulent flames with local extinction, that is because the IEM model uses the mean of particles in a cell and has a shortcoming of non-localness in a mixing [67,72].

4.2.2 Modified Curl mixing model

The Curl's Coalescence and Dispersion (CD) model [73] was originally used to describe the interaction of liquid droplets in a two-liquid phase chemical reactor. Its key idea is that the interaction with other particles can change the composition of particles. When considering a pair of unequally weighted mixing particles i th particle and j th particle, the mass conservation equation from time t to $t+1$ can be written as

$$\phi^{(i),t+1} = \phi^{(j),t+1} = \frac{w^{(i)}\phi^{(i),t} + w^{(j)}\phi^{(j),t}}{w^{(i)} + w^{(j)}}, \quad (4.11)$$

where the w represents the weights of particles.

To compensate for some of the significant shortcomings of the original model, Janicka et al. [74] developed the Modified Coalescence and Dispersion (Modified Curl) model; they introduced a parameter to control the degree of mixing for every mixing particle. Equation (4.11) will be modified as

$$\phi^{(i),t+1} = \phi^{(i),t} + h \left(\frac{w^{(i)}\phi^{(i),t} + w^{(j)}\phi^{(j),t}}{w^{(i)} + w^{(j)}} - \phi^{(i),t} \right), \quad (4.12)$$

$$\phi^{(j),t+1} = \phi^{(j),t} + h \left(\frac{w^{(i)} \phi^{(i),t} + w^{(j)} \phi^{(j),t}}{w^{(i)} + w^{(j)}} - \phi^{(j),t} \right). \quad (4.13)$$

Here the value of h is between 0 and 1. h equals to 0 means no mixing happens, and h equals to 1 makes Equation (4.12) and Equation (4.13) become Equation (4.11).

Similar to the IEM model, the Curl model and Modified Curl model are also not prioritized for PDF simulation of reaction streams; In the composition space, these models are all considered non-local, and the additional random parameter h causes discontinuous jumps in particle composition.

4.2.3 Euclidean Minimum Spanning Tree (EMST) model

As discussed in Sections 4.2.1 and 4.2.2, the IEM model and Modified Curl model are non-local in the composition space. When doing transported PDF simulations or dealing with high Damköhler numbers reacting flows, these models are unsuitable. Subramaniam and Pope [75] proposed a particle-interaction model to solve this problem. When dealing with particle pair mixing, this model introduces bias; In this model, particles closer together in composition space are considered to have a greater chance of mixing than particles farther apart. The EMST model selects subsets of particles in scalar space to generate a Euclidean minimum spanning tree, and this kind of selection is based on the particle weights and the edge weights. When considering a composition space that has $N_s + 1$ dimensions and N_p particles $\phi_\alpha^{(i)}$ ($\alpha = 1, 2, \dots, N_s + 1$), the mixing of particles can be written as

$$\frac{d\phi_\alpha^{(i)}}{dt} = -\frac{1}{w^{(i)}} M_{ij} \phi_\alpha^{(j)}, \quad i = 1, \dots, N'_p \quad (N'_p \leq N_p), \quad (4.14)$$

where M_{ij} is the interaction matrix, which can be obtained as

$$M_{ij} = -\alpha_p \sum_{v=1}^{N'_p-1} B_v \left(\delta_{im_v} \delta_{jn_v} + \delta_{jm_v} \delta_{in_v} \right), \quad i \neq j, \quad (4.15)$$

$$M_{(i)(i)} = \alpha_p \sum_{j=1}^{N'_p} \sum_{v=1}^{N'_p-1} B_v \left(\delta_{im_v} \delta_{jn_v} + \delta_{jm_v} \delta_{in_v} \right). \quad (4.16)$$

In the interaction matrix, α_p controls the decay rate of the variance of the control scalar edge, B_v is the edge coefficient of the v th spanning-tree edge that connects m_v and n_v particles, and δ is the Kronecker delta; the EMST model focuses on maintaining localness, which can yield burning flames without any difficulty.

4.3 NIST Fire Dynamics Simulator (FDS) code

Fire Dynamics Simulator (FDS) is created by NIST [76] for CFD simulations of low-speed flows; it is suitable for solving the heat transfer problems of fire and smoke propagations [77]. It can use the large eddy simulation (LES) model or the direct numerical simulation (DNS) model to do the calculation. However, the commonly used Reynolds averaged Navier–Stokes (RANS) model is not considered. The FDS code and the other four fire models have been verified and validated by NRC [78]. The governing equations of FDS are shown below

The continuity equation is

$$\frac{\partial \rho}{\partial t} + \frac{\partial \rho u_i}{\partial x_i} = 0. \quad (4.17)$$

The species concentration (mass fraction) equation is

$$\frac{\partial \rho Y_\alpha}{\partial t} + \frac{\partial \rho u_i Y_\alpha}{\partial x_i} = \frac{\partial}{\partial x_i} \left(\rho D_\alpha \frac{\partial Y_\alpha}{\partial x_i} \right) + \dot{m}_\alpha''', \quad (4.18)$$

Where Y_α is the mass fraction of species α , D_α is the diffusion coefficient of species α , and \dot{m}_α''' means the rate of mass production of species α per unit volume due to chemical reactions.

The momentum (finite-difference approximation) equations can be written as

$$\left\{ \begin{array}{l} \frac{\partial u_i}{\partial t} + F_i + \frac{\partial H}{\partial x_i} = 0 \\ H = \frac{|\mathbf{u}|^2}{2} + \frac{p}{\rho} \\ \nabla^2 H = - \left[\frac{\partial}{\partial t} \left(\frac{\partial u_i}{\partial x_i} \right) + \frac{\partial F_i}{\partial x_i} \right] \end{array} \right. , \quad (4.19)$$

where F_i is the combination of advective and baroclinic terms.

The energy (sensible enthalpy) equations are

$$\begin{cases} \frac{\partial u_i}{\partial x_i} = \frac{1}{\rho h_s} \left[-\frac{\partial \rho h_s}{\partial t} - u_i \frac{\partial \rho h_s}{\partial x_i} + \frac{D\bar{P}}{Dt} + \dot{q}''' - \nabla \cdot \dot{\mathbf{q}}'' \right], \\ \dot{\mathbf{q}}'' = -k\nabla T - \sum_{\alpha} h_{s,\alpha} \rho D_{\alpha} \nabla Y_{\alpha} + \dot{\mathbf{q}}_r'' \end{cases}, \quad (4.20)$$

where \dot{q}''' means heat release rate per unit volume, $h_{s,\alpha}$ is the specific enthalpy of species α , $\dot{\mathbf{q}}''$ is the heat flux vector, and $\dot{\mathbf{q}}_r''$ is the radiative heat flux.

The ideal gas equation of state is

$$T = \frac{\bar{P}}{\rho R_m} = \frac{\overline{P\bar{W}}}{\rho R}. \quad (4.21)$$

All these equations shown above are solved explicitly in time, and the predictor-corrector scheme is used. In the FDS code, firstly, the scalar and continuity equations are solved to get the density ρ and scalars Y_{α} of species α . The code estimates the scalars using an explicit Euler step. Secondly, the temperature T is obtained from the ideal gas equation; the code calculates the temperature from the equation of state. Thirdly, the velocity divergence is calculated from the energy equation and used in the pressure solver, and the code computes the velocity convergence ($\nabla \cdot \mathbf{u}$). Fourthly, the Poisson equation is solved by the code for getting pressure. Fifthly, the momentum equation is solved for getting velocity \mathbf{u} . Finally, the time step size for numerical stability is checked to see if the time step size δt satisfies the numerical stability. If the δt is too large, the calculation will reduce the time step size and repeat previous steps. Otherwise, the code will go to the final corrector step.

In the final corrector step, the code estimates the species from n th quantities and gets density ρ^{n+1} and scalars Y_{α}^{n+1} of species α , calculates the temperature from the equation of state and get T^{n+1} , and calculates and stores the source terms for both predictor and corrector in the next step, and the calculation includes dealing with heat release rate, radiation, mass source, etc. The code will also compute the velocity convergence, solve the Poisson equation, and correct velocity by solving the momentum equation to get \mathbf{u}^{n+1} .

4.4 Coupling method between FDS and HPDF

Solve Equation (4.2) of the transported PDF model requires information about the simulation mesh grids, velocity fields, and transport properties. There is a possibility to couple these two

methods together since all the information can get from the FDS code. The coupling between these two methods may bring some potential improvements. The HPDF code has more advantages in solving chemical reaction terms; it gets a more accurate result of temperatures in the combustion region. It also has better capability to deal with flame local extinction problems and study flame instabilities. Besides, only equal diffusivity is assumed in the transported PDF model, but the different molecular diffusivities for different species can be considered in the FDS code.

In this work, a simple implementation of these two models is conducted. The pressure is assumed constant and uniform in the gas phase region, which is the whole calculation space; the specific heat capacity will also be treated as constant and uniform in space; it can be calculated as

$$C_{p,\alpha} = \frac{\gamma}{\gamma-1} \frac{R}{W_\alpha}, \quad (4.22)$$

where the subscript α corresponds to species α , W_α represents the molecular weight of species α , γ is the specific heat ratio, which has a value of 1.4 in this work.

The coupling between the FDS code and the HPDF code is mainly fulfilled using the ideal gas equation and the sensible enthalpy equation. For the coupling of the ideal gas equation, Equation (4.10) of the FDS code will be transformed as

$$T = \frac{\bar{P}}{\rho R_m} = \frac{\bar{P}\bar{W}}{\rho R} = \frac{\bar{P}}{\rho R \sum_{\alpha=0}^{N_s} (Y_{\alpha,\text{FDS}} / W_\alpha)} = \frac{\bar{P}}{\rho R \sum_{\alpha=0}^{N_s} (Y_{\alpha,\text{PDF}} / W_\alpha)}, \quad (4.23)$$

where the $Y_{\alpha,\text{FDS}}$ is the mass fraction of species α gets from the FDS code, $Y_{\alpha,\text{PDF}}$ represents the mass fraction of gas species α calculated from the transported PDF model.

For the sensible enthalpy equation's coupling, the sensible enthalpy calculation method needs to be consistent in the FDS code and transported PDF. The FDS code uses Equation (4.9) to do the calculation; the coupling method will become [79]

$$\left\{ \begin{array}{l} \frac{\partial u_i}{\partial x_i} = \frac{1}{\rho h_s} \left[-\frac{\partial \rho h_s}{\partial t} - u_i \frac{\partial \rho h_s}{\partial x_i} + \dot{q}_{\text{HPDF}}'' - \nabla \cdot \dot{\mathbf{q}}'' + 2\rho f_e \Omega_F (h_{s,\text{HPDF}} - h_s) \right] \\ f_e = 1.05, \quad \Omega_F = \frac{1}{8\Delta t} \\ \dot{\mathbf{q}}'' = -k\nabla T - \sum_{\alpha} h_{s,\alpha} \rho D_\alpha \nabla Y_{\alpha,\text{HPDF}} \end{array} \right., \quad (4.24)$$

where the original $D\bar{P}/Dt$ term becomes zero because the Mach number of this work is much smaller than 0.3, the subscript HPDF means results come from the HPDF code, and the $2\rho f_e \Omega_F (h_{s,\text{HPDF}} - h_s)$ term is the relaxation term for consistency between the FDS code and HPDF code.

In the coupled model, the thermal conductivity of the species is calculated based on the equations [80, 81] as

$$\begin{cases} K = a_1 + a_2 T + a_3 T^2 + a_4 T^3 + a_5 T^4 + a_6 T^5 + a_7 T^6 \\ \ln K = A \ln T + \frac{B}{T} + \frac{C}{T^2} + D \end{cases}, \quad (4.25)$$

where the coefficients of the polynomial are from the cited papers.

The thermal conductivity k for gas mixture is calculated by using a simplified method [82] with a 2% standard deviation

$$K = \frac{\sum K_\alpha X_\alpha (W_\alpha)^{\frac{1}{3}}}{\sum X_\alpha (W_\alpha)^{\frac{1}{3}}}, \quad (4.26)$$

where the X_α is the mole fraction of species α , W_α represents the molecular weight of gas species α .

In FDS code, values of specific heat capacity C_p and sensible enthalpy H_s are obtained from NIST-JANAF tables [83]; the coupling model uses the same method

$$\begin{cases} C_p = R(a_1 T^{-2} + a_2 T^{-1} + a_3 + a_4 T + a_5 T^2 + a_6 T^3 + a_7 T^4) \\ H_s = RT(-a_1 T^{-2} + a_2 \ln T / T + a_3 + a_4 T / 2 + a_5 T^2 / 3 + a_6 T^3 / 4 + a_7 T^4 / 5 + b_1 / T) \end{cases}. \quad (4.27)$$

4.5 Introduction of UMD line burner

Different types of burners have been used to test the methodology for investigating the pool fire experimentally. The UMD burner can introduce the characteristics of turbulence and buoyancy effects on the fire; it can also be used to test the suppression effects. The UMD burner will be used to investigate the fire simulations in this dissertation.

The UMD burner was built by White et al. [84, 85] in the turbulent line burner (TLB) experimental facility at the University of Maryland. The UMD burner is a slot burner that uses gaseous fuel; it can generate a low-strained turbulent diffusion flame that is dominated by buoyant.

The inlet flow is well characterized. All the boundary conditions are also well-controlled. The essential flame characteristics and the local experimental data can be measured using a series of non-invasive diagnostics.

The suppression effects of flames can be observed by using a nitrogen diluted oxidizer stream, and the water mist can also be added to the oxidizer [86, 87]. The combustion efficiency is used to monitor the fire performance, and its value is measured using calorimetry techniques based on species. With the additional nitrogen gas or the added water mist, the heat generated by the chemical reaction will quickly dissipate, and the peak flame temperature will decrease. When the flame temperature is decreased under a critical value, the chemical reactions can no more self-sustained, and the extinguished phenomenon will happen to the flame. The studies of flame local extinction and flame instabilities can be performed using these experimental data.

A schematic diagram of the burner is shown in Figure 4.1. The burner's fuel port is made of stainless steel, its width is 5 cm, and its length is 50 cm; the port's sidewalls have a thickness of 1.5 mm. A co-flowing oxidizer port surrounds the fuel port; its size is 50 cm in width and 75 cm in length. Under the oxidizer port, many flow control elements are used to ensure the oxidizer is thoroughly mixed. The oxidizer is discharged from the port with a uniform vertical speed by using a blower. The float flow meter lets the nitrogen gas, or the water vapor, come in as a diluent; a series of mist generators are used to send the water vapor to the flame.

The oxidizer and the fuel ports are not in a horizontal plane; the fuel port is 15 mm higher than the oxidizer port, and the fuel port is enclosed in the surrounding ceramic fiber slats; these strips have a height of 5mm and a width of 5mm. That makes the fiberboard 5 mm taller than the oxidizer port and 10 mm lower than the fuel port. The fiberboard is set higher than the oxidizer, so the velocity of the oxidizer can be reduced near the bottom of the burner. It can also reduce the generation of laminar structures, trigger buoyancy-driven turbulence near the fuel port, and promote the transition to a fully turbulent flame.

In the experimental study, the nominal CH₄ has a flow rate of 1.00 +/- 0.02 g/s. It comes out from the fuel port with a velocity of 6.0 cm/s, this kind of specified fuel flow rate can ensure that the fuel stream flow is purely laminar, and these fuels can generate roughly 50 KW total heat release rate. A uniform co-flow air stream surrounds the burner, and the oxidizer flow has a flow rate of 85 +/- 7 g/s and roughly 25 cm/s velocity. This flow rate ensures that the oxidizer flow can provide enough oxygen, which is five times than the requirements for the stoichiometric

combustion of the CH₄; it also minimizes the impact on the entrained structure of the flame from the surrounding air.

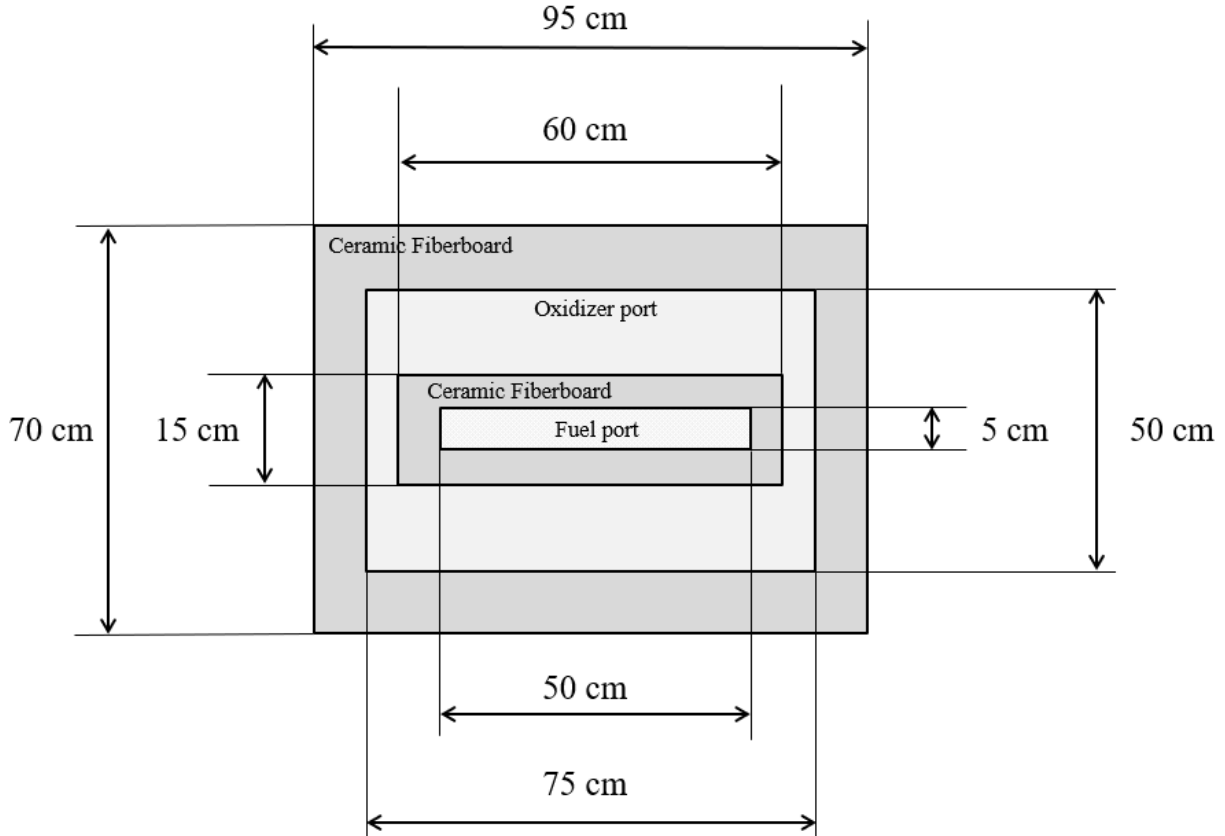


Figure 4.1. A plan-view schematic diagram of the experimental apparatus shows the burner's size and the fuel and oxidizer ports.

An O₂ anchor can be located along each side on the top of the ceramic fiberboard. The O₂ anchor can reduce the lift-off extinguishing in the current fire case and allow the study of significantly diminished flames. The O₂ anchor will be applied along the edges of the ceramic fiber slats. The O₂ flow will be injected into the flame at a 45° degree, and the anchor has a length of 50 cm and a width of 2 mm. Only the burner without an O₂ anchor will be considered and investigated in this study.

This dissertation will use experimental data to evaluate the coupled FDS-HPDF model and different mixing models and parameters. The time-averaged temperatures at several locations above the fuel port will be used to validate the coupled model. The measured temperatures were

extracted from selected elevations corresponding to z locations 12.5 cm and 25.0 cm above the fuel port. The measured combustion efficiency under the oxidizer's different oxygen depletion levels will be used to test the coupled model's predictions of fire extinction limits. The detailed investigations will be presented in Chapter 5.

4.6 Conclusions

In this chapter, the transported PDF model and its governing equations have been introduced. Three different mixing models, the IEM model, the Modified Curl model, and the EMST model, have been briefly discussed. The NIST Fire Dynamics Simulator (FDS) code and the coupling method between the FDS code and an in-house PDF code called HPDF have been introduced. A brief introduction of the University of Maryland line burner and its experimental setup has been made, and the experimental data of the UMD burner will be adopted as validation test cases.

5. INVESTIGATION OF UMD FIRE BY USING FDS AND HPDF

In this chapter, the UMD fire case will be instigated using the FDS code and the coupled FDS-HPDF model and adopted as a validation test case. The simulation results are validated by using the available experimental data of time-mean temperatures at selected elevations above the fuel port. The combustion efficiency under the different oxygen depletion levels in the oxidizer will be analyzed. The model's capability to capture this extinction limit is assessed by using the experimental data. Different mixing models and model parameters are examined, and their importance and further enhancement for predicting fire extinction will be discussed.

5.1 FDS results of UMD flame simulations

Firstly, a methane flame generated by the UMD burner is used for the investigations. As mentioned in Section 4.5, the experimental methane flow rate from the fuel port is 1.00 +/- 0.02 g/s (with a velocity of 6.0 cm/s); under the complete combustion condition, these fuels can generate a fire with a 50 KW heat release rate.

The nitrogen-dilution suppression experiment results are used for a preliminary comparison. A gaseous nitrogen flow is introduced into the oxidizer; the gas mixture's flow rate has a constant value of 85 +/- 7 g/s (with a velocity of 25 cm/s). A paramagnetic oxygen analyzer is used to measure the oxygen mole fraction, and the experimental data of diluted air with 18% oxygen is used.

The experiment uses a camera to measure the visible flame height, which is 50% intermittent flame height [55]. The radiative flame emissions and the root-mean-square (RMS) and time-averaged temperatures are recorded, and the mole concentrations of the combustion products are also collected.

The computational domain is shown on the left-hand side of Figure 5.1; its size is 85 cm, 2 m, and 1.5 m in x, y, and z directions. This domain size is large enough for the simulation; the excessive boundary-condition effects are suppressed using this grid and will not affect the flame's simulation. The calculation domain has two different sets of grid sizes, as shown on the right-hand side of Figure 3.2. A refinement mesh is used for the locations near the fuel and oxidizer ports; the mesh has a uniform grid size in each direction; the resolution is $\Delta x = \Delta y = \Delta z = 15$ mm. This

refinement mesh's outer region uses a coarse mesh with a uniform numerical grid size in each direction. The grid size is $\Delta x = 30$ mm, $\Delta y = 35$ mm, and $\Delta z = 37.5$ mm. The open and passive flow boundaries are used for the top side, and on all four sides around the calculation domain, the background gas of the simulation is set as ambient air. The initial condition for the whole interior calculation domain is set as a uniform composition of air. The fuel and oxidizer ports use the mass flow boundary conditions. The fuel and the co-flow oxidizer's mass flow rates are the same as in the experiment, which is 1.00 ± 0.02 g/s for the methane fuel and 85 ± 7 g/s for the diluted air with 18% oxygen. The fuel and oxidizers' temperatures are set as 273 K. Zero flow boundary conditions are applied for the ceramic fiber slab walls around the fuel and oxidizer port, and their temperatures are set as a constant at 273 K.

Another N_2 mass flux jet comes out from the oxidizer port to mix with air to get the diluted air with 18% oxygen. The un-diluted air with 21% oxygen is used at the beginning of the experiment and continues for about 20 seconds to achieve a steady condition for the flame and the flow fields. After that, the mole fraction of oxygen will decrease to 18% within 10 seconds; the final value of 18% will be held constant for the remaining 50 seconds. The total simulation time is 80 seconds; all the scalars of turbulent statistics will be collected after the 50s of the calculation's beginning to ensure the flame and flow are finally stationary. A total number of 24 processors are used for the calculation.

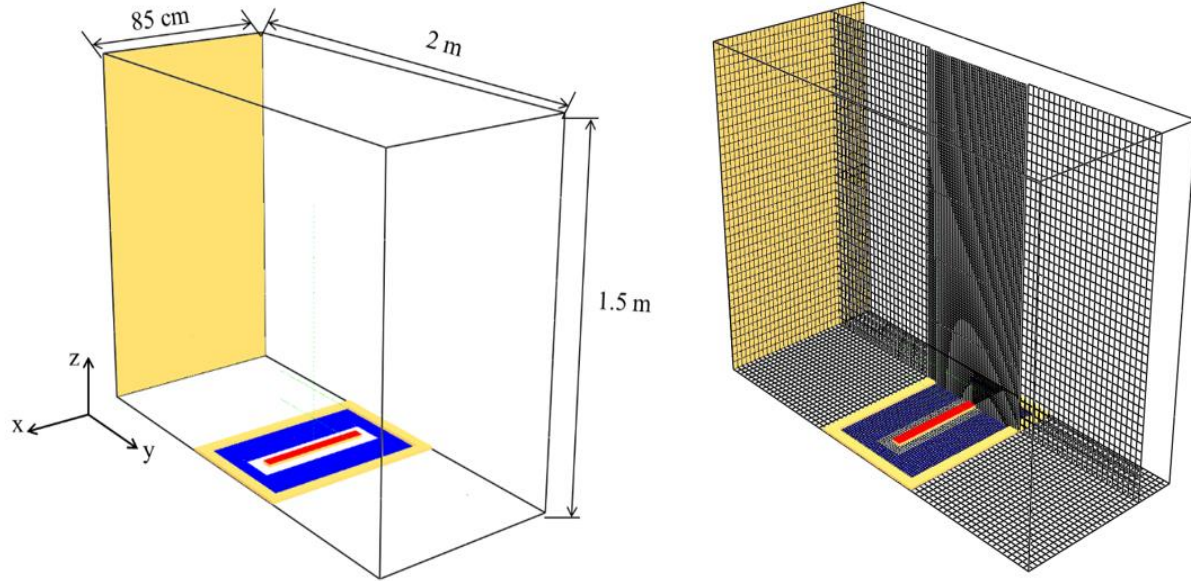


Figure 5.1. Schematic diagram of the numerical configuration; The coordinate of the calculation domain and its size are shown on the left plot. The grids of the inner refinement mesh and outside coarse mesh are shown on the right plot.

Simultaneous flame images showing the front and side view of the CH₄ flame are presented in Figure 5.2. The camera-taken images of the experiment shown on the figure's left-hand side are captured from White's paper [87]. The flame is centered above the fuel port with a co-flowing oxidizer using the diluted air with 18% oxygen; the ceramic fiberboard around the fuel port can be viewed in the experimental pictures. The enhanced buoyancy-driven turbulent near the flame base can be observed from the experimental images; almost all the fire flames are transferred to become turbulent, except for the small region near the fuel port. Because of the diluted air with 18% oxygen usage, the images can capture very significant flame weakening. The flame structure has remarkable changes, and extensive local extinctions happen.

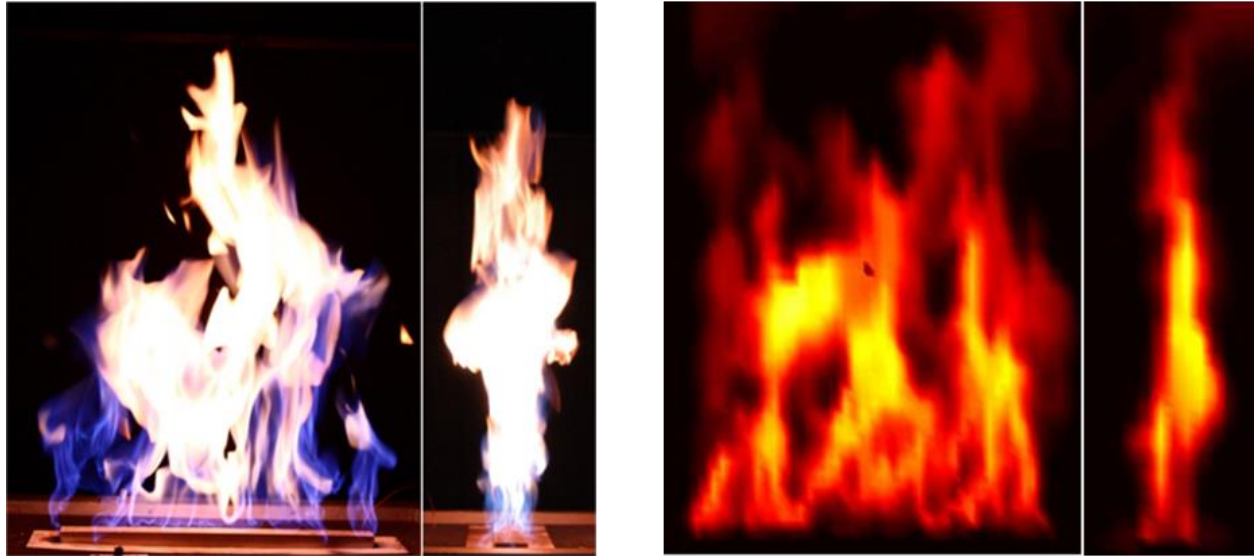


Figure 5.2. Camera-taken simultaneous photos from the front and side view of the methane flame using the diluted air with 18% oxygen are captured from White's paper [87] and shown on the left side. Simultaneous temperature contour plots of CH₄ flame from the simulation are shown on the right side; the temperature range is 300 K to 2200 K.

The simulations use the same boundary conditions as the experiment; the simultaneous temperature contour plots are shown on the right side of Figure 5.2. Many small, black-colored regions with low temperatures can be observed in the luminous orange flame region. These black zones may reveal the local quenching and extinction of the flame. The simulation temperature contour plots share similar flame structures as the experimental images. The drastic changes in the flame structure can be viewed from the plotted unsmoothed temperature distributions.

A quantitative comparison between the experiment and simulation is presented in Figure 5.3; the flame temperatures and the mole fractions of O₂ are used. The experimental data are measured at a series of y locations across the flame; the corresponding z locations are 12.5 cm and 25.0 cm above the fuel port. The experimental data only contains the time-averaged values at these two different elevations, and only the diluted air with an 18% oxygen case is measured. The simulation uses the same type of fuel and oxidizer and extracts data from the same location. As shown in Figure 5.3, the calculated temperature and O₂ concentration fit the experimental data reasonably well. The O₂ mole fraction exceeds 18% in the first plot because the ambient air acts as the background gas in the simulation for outside open boundaries. The calculated peak temperature is

lower than the experimental data in the third plot, but the differences are acceptable. The validation of the FDS model is approved from this case.

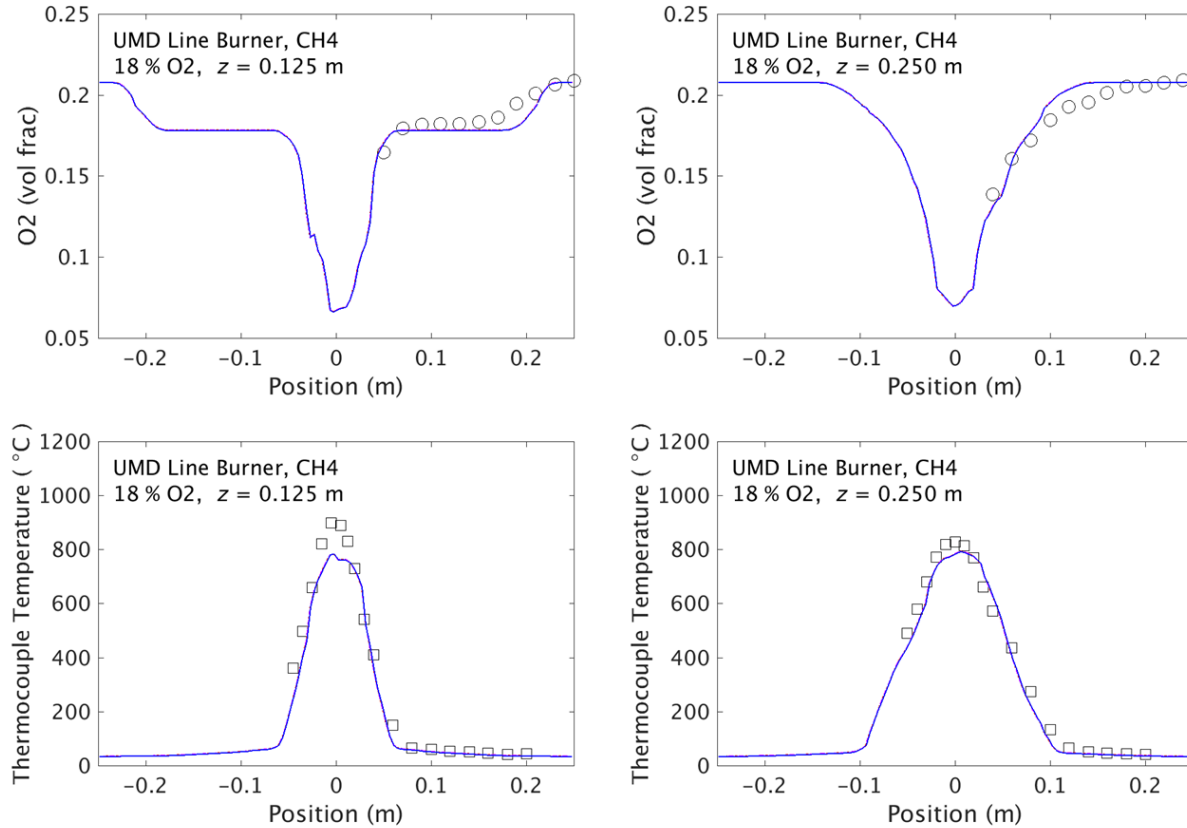


Figure 5.3. Calculated (blue line) and measured experimental data of the time-averaged temperature (squared dots) and O₂ mole fraction (circled dots) at different z locations above the fuel port; the oxidizer is the diluted air with 18% oxygen. The left plots are from z = 12.5 cm location, the right plots are at z = 25.0 cm.

5.2 Validation of CH₄/Air flame simulation using the coupled FDS-HPDF model

The method of coupling the FDS model and the HPDF model has already been introduced in Section 4.4. The coupled FDS-HPDF model is used to simulate CH₄/Air flame, and the diluted air with 18% oxygen is used as an oxidizer. The computational domain coordinate will change due to the HPDF model's features; a schematic diagram showing the new coordinate is plotted in Figure 5.4. In the simulation, the oxidizer and fuel port are settled on the same horizontal plane due to the HPDF model's characteristics. The ceramic fiberboards will be 15 mm higher than the

fuel and oxidizer ports. The computational boundary settings and initial conditions are the same as in previous calculations.

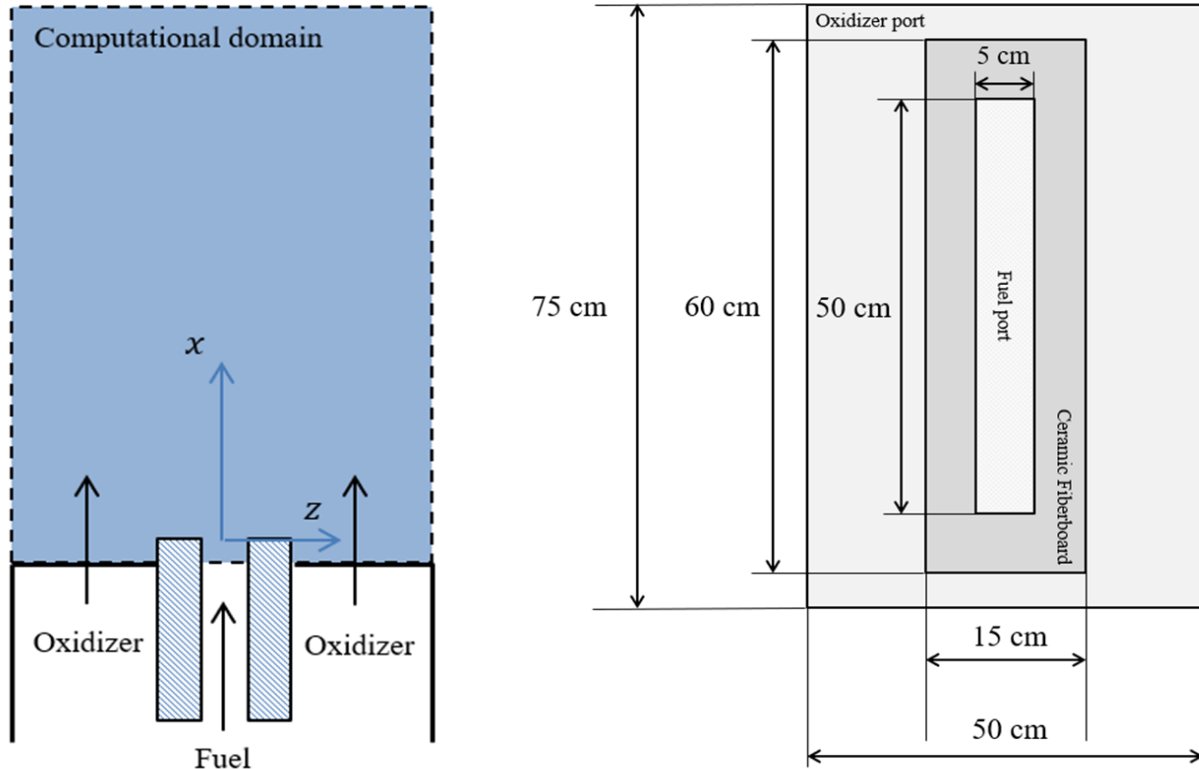


Figure 5.4. A schematic diagram of the simulation domain, the coordinate and boundary settings are shown on the left side; A plan-view of the fuel and oxidizer port surface is shown on the right side.

The HPDF model can only handle periodic boundary conditions with uniform grids in the y-direction. Thus, the left and right sides of the calculation domain are set as periodic boundaries; the other two sides and the top are set as open and passive flow boundaries. The sizes of the computational region will be changed, as shown in Figure 5.5. A mesh has a uniform numerical grid size in each direction with $\Delta x = \Delta z = 5$ mm, and $\Delta y = 25$ mm is used for this simulation to do a preliminary validation test. A relatively coarse uniform grid in the y-direction between the two periodic boundaries reduces the calculation cost.

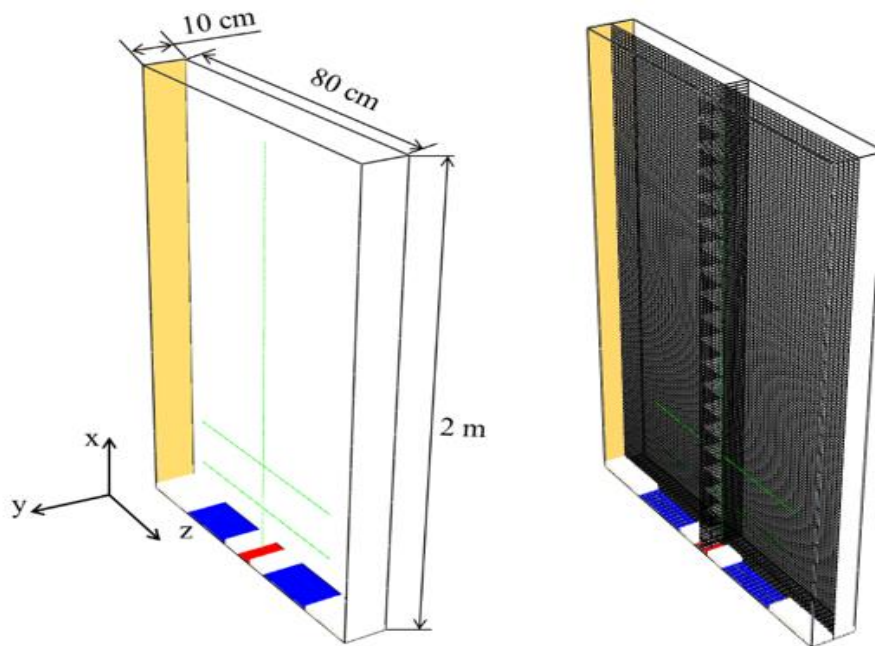


Figure 5.5. Schematic diagram of the numerical configuration; The coordinate of the calculation domain and its size are shown on the left plot. The grids of the mesh are shown on the right-hand side plot.

The grid sensitivity of the coupled FDS-HPDF model calculation of the velocity and temperature has been investigated to check the availability of this grid size for the HPDF calculation.

Two additional grid sizes with $\Delta x = 3.75$ mm, $\Delta y = 18.75$ mm, $\Delta z = 3.75$ mm, and $\Delta x = 2.5$ mm, $\Delta y = 12.5$ mm, $\Delta z = 2.5$ mm have been used for the analysis. As shown in Figure 5.6, the difference between the chosen grid size with $\Delta x = 5$ mm, $\Delta y = 25$ mm, $\Delta z = 5$ mm, and the other two grids are insignificant. The chosen grid can accurately capture the fire case's temperatures and local O₂ mole fractions and achieve a good balance between computational cost and accuracy.

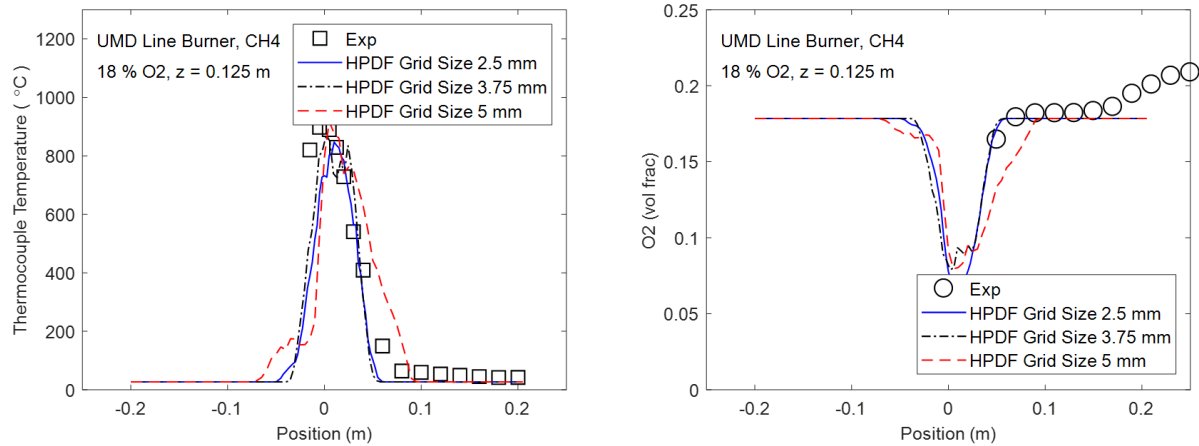


Figure 5.6. Calculated and measured experimental data of the time-averaged temperature (squared dots) and O₂ mole fraction (circled dots) above the fuel port; the oxidizer is the diluted air with 18% oxygen. The solid blue line represents a 2.5 mm grid, the black dash-dotted line represents a 3.75 mm grid, and the red dashed line represents a 5 mm grid.

As mentioned in Section 4.2, the choice of mixing models and C_ϕ values can significantly impact the simulation results. The C_ϕ values cannot significantly affect the flow and turbulence fields, but this value controls the mixing rate for the mixing model used in this section.

Only the EMST model will be used in this section to validate the coupled FDS-HPDF model. That is because the IEM model and the Modified Curl model lack accuracy when dealing with fire local extinction due to the non-locality in mixing and composition space. The UMD burner was used to assess the possible effect of each extinguishing and reignition treatment on the flame structure under partially suppressed conditions. However, for this particular validation case, only the partially-diluted oxidizer condition with 18% oxygen will be used; under this circumstance, the fire will lack local extinction. By using this kind of partially-diluted oxidizer, complete combustion of the fire case is still expected. The default value $C_\phi = 3.0$ will be used for the model validation due to the insignificant flame local extinction. The following section will provide a detailed comparison of different mixing models and C_ϕ values.

A mechanism called DRM19 [88] is used; it contains 19 species and 84 detailed chemical reactions. These chemical kinetics are a reduced version of the GRI-Mech 1.2 methane mechanism

[89]. The transport and thermodynamic properties are also obtained from the GRI databases. The particle number per cell for the HPDF model uses a constant number of 20.

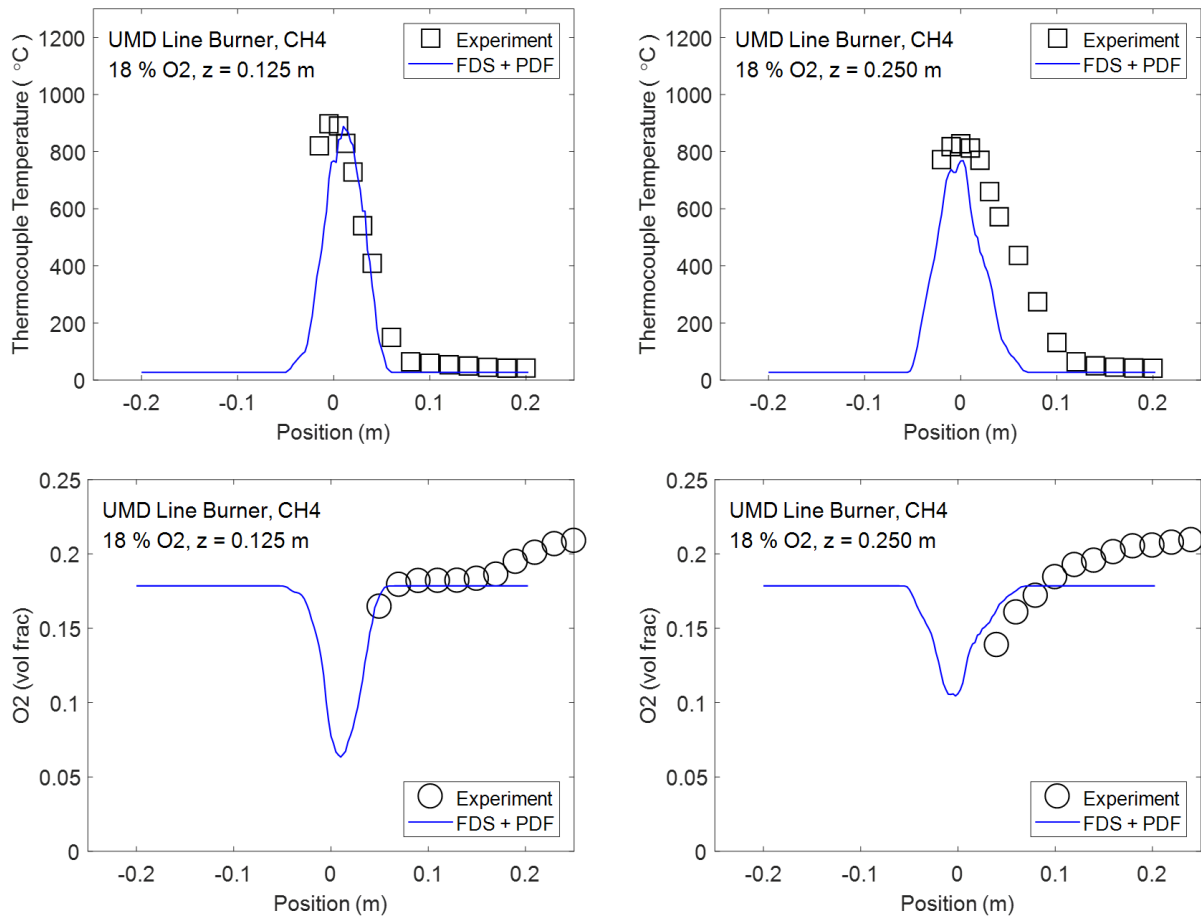


Figure 5.7. Calculated (blue line) and measured experimental data of the time-averaged temperature (squared dots) and O₂ mole fraction (circled dots) at different z locations above the fuel port; the oxidizer is the diluted air with 18% oxygen. The left plots are from z = 12.5 cm location, the right plots are at z = 25.0 cm.

Validation of the coupled FDS-HPDF model against experimental measurements is presented in Figure 5.7. The calculated and measured experimental data of the time-averaged temperature and O₂ mole fraction are extracted at two selected locations z = 12.5 cm and 25.0 cm above the fuel port; the oxidizer is the partially diluted air with 18% oxygen.

As shown in Figure 5.7, the calculation result of the coupled FDS-HPDF model is fairly consistent with the experimental data. Similar to the simulation results of the original FDS code, the peak simulated temperature at two selected locations z = 12.5 cm and 25.0 cm fits the measured

data pretty well. However, the flame temperature distribution area is slightly narrower than the experimental value.

These comparisons verify that the average temperature and mixing fields generated in each case are similar to those measured experimentally and confirm that the coupled FDS-HPDF model can correctly simulate the flame structure. The results also show that the EMST model and the default value $C_\phi = 3.0$ are suitable for fire case studies; the quenching and reignition phenomena are rarely in the calculated flame.

As mentioned previously, the HPDF model can only handle periodic boundary conditions with uniform grids in the y-direction, and $\Delta y = 25$ mm grid is used for this simulation. Due to the coarse mesh size in the simulation's y-direction, only the CH₄/Air flame's side views will be compared with the experimental camera-taken photos and coupled FDS-HPDF model simulation data from the experimenters. A series of temperature contour plots of the simulation is shown in Figure 5.8. The temperature range of the simulation results is from 297 K to 1815 K.

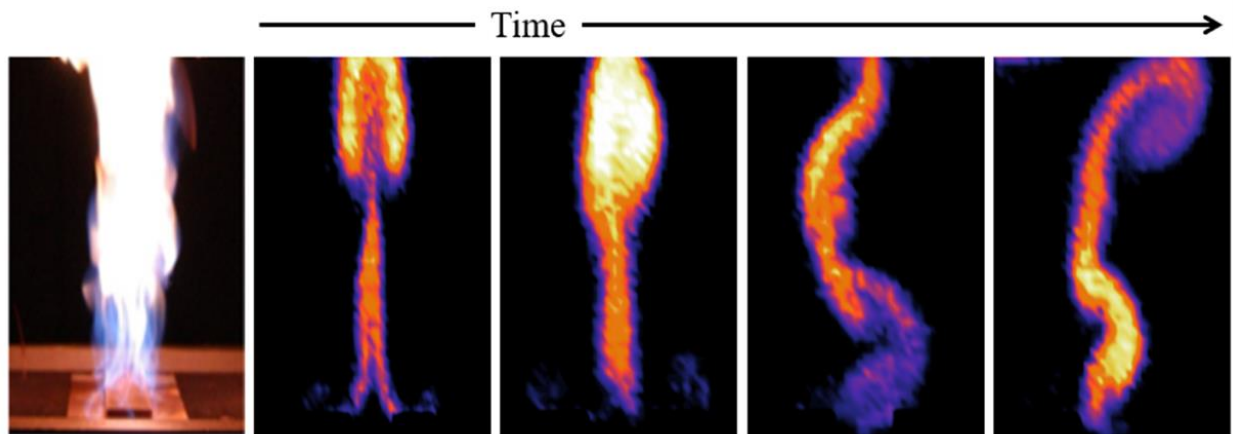


Figure 5.8. Camera-taken instantaneous distribution side-view of the experimental captured from White's paper [54] and temperature contour plots in the simulation's x-z plane. The camera-taken photo is on the left side, and a series of temperature contour plots generated by the coupled model are shown on the right side.

In Figure 5.8, the instantaneous temperature distributions of the experimental measurement and the simulation results are attached to the ceramic fiberboard around the fuel port with a shape like two anchors, and the buoyancy introduced turbulence can be observed from the plots; the steady flames are transferring to turbulent due to the buoyancy-driven upstream.

A flame flickering and oscillation phenomenon can be clearly seen in Figure 5.8; the methane flow comes out from the fuel port, and its velocity is 6.0 cm/s, and the diluted air with 18% oxygen comes out from the oxidizer port with a much higher velocity of 25 cm/s. A circulation zone will be generated near the bottom of the flame, the root of the flame will regularly sway back and forth between the walls of the fuel port, and the observed period of flame oscillation is approximately 1.0 seconds to 1.5 seconds from the simulation results. Since the experimental data only provide the flame height, temperatures, and O₂ mole fractions, comparing flame oscillation frequencies needs more detailed experimental data.

5.3 Investigation of combustion efficiency and fire extinction limits by using coupled FDS-HPDF model

From the experimental data, fire extinction limits were found to occur when the oxygen depletion level reduces to a certain level. In this section, the combustion efficiency under the different oxygen depletion levels in the oxidizer will be analyzed; the coupled model's capability to capture this extinction limit is assessed by using these experimental data. Different mixing models and model parameters will also be examined.

5.3.1 Calculation of heat release rate

When studying fires, the size, the fire spread speed, the material's flammability, and the yield of toxic species are all key components of the study. In order to derive various fire characteristics, the heat release rate is considered an essential and important parameter. It is often considered the most critical parameter in describing fire hazards [90]. The parameter combustion efficiency can be used as a dimensionless quantification of the normalized flame intensity. It can be considered an ideal metric for assessing fire suppression and local extinction performance. In the experimental measurements, the combustion efficiency can be expressed as

$$\eta_{comb} = \frac{\dot{Q}}{\dot{m}_{fuel} \Delta h_{comb}}, \quad (5.1)$$

where the \dot{Q} represents the heat release rate, it is not easy to get accurate measurements of heat release rate, and the cost is pretty high. The \dot{m}_{fuel} is the mass flow rate of CH₄, and the Δh_{comb} is the mass-specific enthalpy of combustion of CH₄. Although the heat release is very difficult to be

measured experimentally, the UMD fire case used species-based calorimetry to do the measurements.

For the numerical part, the combustion efficiency can be expressed as

$$\eta_{comb} = \frac{1}{\tau \dot{m}_{fuel} \Delta h_{comb}} \int_{\tau} \int_V \dot{Q}''' dV dt, \quad (5.2)$$

where the \dot{Q}''' is the local volumetric heat release rate in each computational cell, the τ represents the time average window. Specifically, when dealing with the total heat release rate in our coupled FDS-HPDF calculations, the combustion model used is based on reactions of lumped species. The lumped species are scalars of the reaction that can represent a mixture of species. The volumetric heat release rate from the combustion per unit volume can be given as

$$\dot{Q}''' = -\sum_k \dot{m}_k''' \Delta h_{f,k}^{\circ}, \quad (5.3)$$

where the \dot{m}_k''' is the volumetric mass reaction rate of the k th species in the reaction, and the $\Delta h_{f,k}^{\circ}$ represents the mass-specific standard enthalpy of formation for the k th species. After summing all the lumped species' mass production rates time the heat of formation, the heat release rate per unit volume is obtained. In the coupled FDS-HPDF model, the parameter δ_t controls the time step size, and at the end of each time step, the new mean mass fraction in a cell will be updated as

$$\tilde{Y}_{\alpha}(\delta_t) = \zeta(\delta_t) \tilde{Y}_{\alpha}^0 + (1 - \zeta(\delta_t)) \hat{Y}_{\alpha}(\delta_t), \quad (5.4)$$

where the \tilde{Y}_{α}^0 is the initially mean mass fraction of the cell and $\hat{Y}_{\alpha}(\delta_t)$ represents the change for the α th species concentration for all N_r reactions in the combustion system,

$$\hat{Y}_{\alpha}(\delta_t) = \tilde{Y}_{\alpha}^0 + \sum_{i=1}^{N_r} \left(\frac{\nu_{\alpha,i} W_{\alpha}}{\nu_{F,i} W_{F,i}} \right) \Delta \hat{Y}_{F,i}, \quad (5.5)$$

$\nu_{\alpha,i}$ means stoichiometric coefficient for the α th species, the W_{α} represents the molecular weight of the α th species.

Back to Equation (5.4), $\zeta(t)$ represents the unmixed fraction of the mass within a specific cell, and the unmixed fraction needs to satisfy the following ordinary differential equation (ODE)

$$\frac{d\zeta}{dt} = -\frac{\zeta}{\tau_{mix}}. \quad (5.6)$$

The τ_{mix} is the characteristic mixing time determines the conversion rate of reactant species to product species in a specific cell, and Equation (5.5) has a solution as

$$\zeta(t) = \zeta_0 e^{-t/\tau_{mix}}, \quad (5.7)$$

where the value of ζ_0 is set as 1 as a default assumption for this dissertation. Combining Equation (6.3) and Equation (6.4), the volumetric mass reaction rate can be expressed as

$$\dot{m}_\alpha''' = \rho \frac{d\tilde{Y}_\alpha}{dt} = \rho \left[\frac{\zeta}{\tau_{mix}} (\tilde{Y}_\alpha - \tilde{Y}_\alpha^0) + (1 - \zeta) \frac{d\hat{Y}_\alpha}{dt} \right], \quad (5.8)$$

and the volumetric heat release rate can be obtained as

$$\dot{q}''' = \rho \sum_\alpha (\tilde{Y}_\alpha(\delta t) - \tilde{Y}_\alpha^0) \Delta h_{f,\alpha}^0, \quad (5.9)$$

in this dissertation, the mass-specific standard enthalpy of formation for different species are $\Delta h_{CH_4}^0 = -4.67E+06$ J/kg , $\Delta h_{O_2}^0 = 0$ J/kg , $\Delta h_{CO_2}^0 = -8.94E+06$ J/kg , $\Delta h_{H_2O}^0 = -1.34E+07$ J/kg , $\Delta h_{CO}^0 = -3.95E+06$ J/kg , and $\Delta h_{N_2}^0 = 0$ J/kg .

5.3.2 Investigation of fire extinction limits prediction

In the experiment, different oxygen depletion levels in the oxidizer were used. The experimental system used an N2 suppression system to inject nitrogen flow into the oxidizer. After using the N2 diluted oxidizer, the O2 mole fraction $X_{O_2}^{ox}$ is reduced, and the stoichiometric O2 required for combustion cannot be satisfied. Then the local quenching and flame suppression will happen in the fire. The firing temperature will reduce as well, and a complete extinction will happen after the reduced temperature cannot sustain the combustion.

When the complete extinction happens, the current value of the O2 mole fraction $X_{O_2}^{ox}$ represents the extinction limit of the used fuel. This parameter is also called the limiting oxygen index (LOI) [91]. The LOI parameter has a relationship with the minimum extinguishing concentration (MEC) [92] as

$$LOI = X_{O_2}^{ox} (1 - MEC), \quad (5.10)$$

this dissertation defines it as the molar fraction of the O2 in the oxidizer at a global extinction.

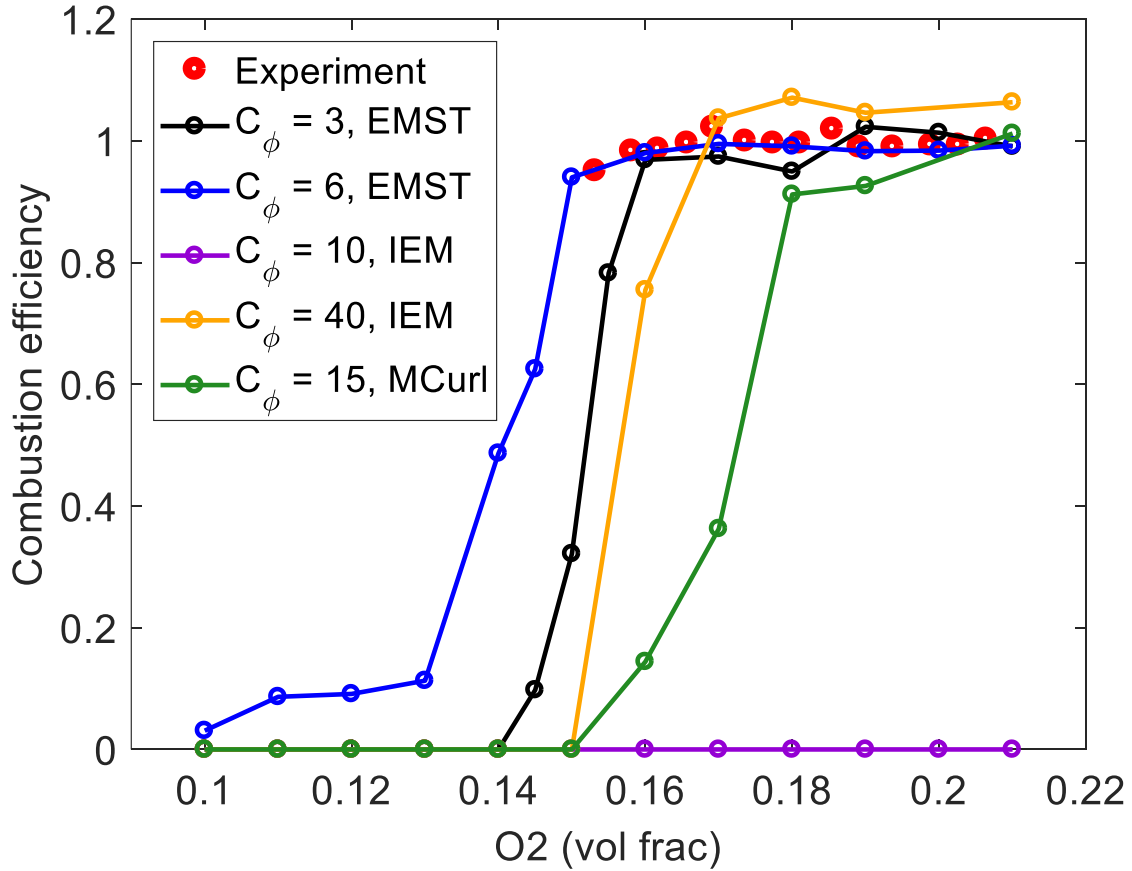


Figure 5.9. Calculated and measured experimental data of the combustion efficiency η_{comb} versus different oxygen levels $X_{O_2}^{ox}$ for the non-anchored flame; the oxidizer is the diluted air with oxygen from 10% to 21% in mole fraction. The black and blue lines are EMST model with C_ϕ equals 3.0 and 6.0; the purple and yellow lines are IEM model with C_ϕ equals 10 and 40; the green line is the Modified Curl Model with C_ϕ equals 15.

Figure 5.9 presents the calculated and measured combustion efficiency η_{comb} for different mixing models and different C_ϕ values versus different oxygen depletion levels and compares them against the experimental data. Each dot represents the time-averaged mean value of combustion efficiency obtained from 100 different time steps. The measured combustion efficiency is represented by using the red dots; the black and blue solid lines show the EMST

model calculated results with C_ϕ equals 3.0 and 6.0; the purple and yellow solid lines present the IEM model simulation results with C_ϕ equals 10 and 40, and the green line represents the calculation results of Modified Curl Mode.

The lowest C_ϕ values that can yield burning flames when using undiluted ambient air with 21% oxygen ($X_{O_2}^{ox} = 0.21$) for different mixing models are compared in Table 6.1.

Only the non-anchored flames are considered in this dissertation. The non-anchored flames will be extinguished and detached from the flame base and liftoff in the experiment when reducing the oxygen levels in the co-flow air; the flame extinction limit is determined if the flame becomes invisible from the recorded image. The final flame extinction limit for the non-anchored CH₄ flame is diluted air with 15.2% oxygen ($X_{O_2}^{ox} = 0.152$).

As shown in Figure 5.9, fire extinction occurs when oxygen depletion reduces to a certain level. The fire extinction limit is very sensitive to the different mixing models and parameters. Several observations can be made from Figure 5.9:

- It is clearly shown in Figure 5.9, within a wide range of $X_{O_2}^{ox}$ from 0.16 to 0.21, the combustion efficiency η_{comb} collected from the experiment is around 1, only a slight change of η_{comb} can be detected. The experimental combustion efficiency η_{comb} reduces to a value of about 0.95 before extinction.
- The EMST model was found can yield burning flames without any difficulty; when giving a default value of C_ϕ , the EMST model results can match the measured η_{comb} for $X_{O_2}^{ox} > 0.15$. For the region with $X_{O_2}^{ox} < 0.15$, the calculated η_{comb} will have higher value with higher C_ϕ value. That's because the C_ϕ value controls the rate of mixing; a higher value of C_ϕ can lead to more intense mixing in the calculation, resulting in a more intense degree of the chemical reaction and increasing the combustion efficiency significantly. The plotted curve of the EMST model will be shifted to the left with a higher value of C_ϕ , and the calculated combustion efficiency η_{comb} will gradually converge to 0 as the oxygen level $X_{O_2}^{ox}$ decreases.

- The IEM model could not yield a burning flame until increasing the value of C_ϕ reaches a very high value ($C_\phi \geq 40$). With the relatively low value of C_ϕ , the calculated flame cannot be attached to the base of the fuel port; it will easily liftoff from the burner and get extinction quickly; the calculated η_{comb} will be represented as a purple line with an equal value to 0 in Figure 5.9. The IEM model can get a burning case with C_ϕ value higher than 40. However, the result fails to follow the experimental trend for $X_{O_2}^{ox} < 0.17$, and the IEM model significantly underpredicts the combustion efficiency η_{comb} .
- The Modified Curl model was also not suitable for yielding a burning flame. The lowest C_ϕ value for a burning case is 15. This model will also underpredict the combustion efficiency η_{comb} and cannot match the experimental data for $X_{O_2}^{ox} < 0.18$.

Table 5.1. Lowest C_ϕ value to yield burning case for CH4 flames in undiluted ambient air.

Mixing Model	C_ϕ can yield burning flames	limiting oxygen index (LOI)
EMST	3	0.14
IEM	40	0.15
Modified Curl	15	0.15

After getting the lowest C_ϕ values to yield a burning case for CH4 flames in undiluted ambient air, these lowest C_ϕ values and their corresponding mixing models are used with coupled FDS-HPDF model to investigate further. The calculated and measured experimental data of the time-averaged temperature and O2 mole fraction are extracted at selected locations $z = 12.5$ cm; the oxidizer is the partially diluted air with 18% oxygen.

As shown in Figure 5.10, the calculation result of different mixing models with the lowest C_ϕ values can yield a burning case that agrees reasonably well with each other and the experimental data. The peak simulated temperature at selected locations $z = 12.5$ cm did not show significant differences between different models. The calculations of O2 mole fractions are similar

to each other. The performance differences between different mixing models are more on the prediction of the flame extinguishing limits; once yield a burning case, there are no significant differences between the calculation results of these mixing models.

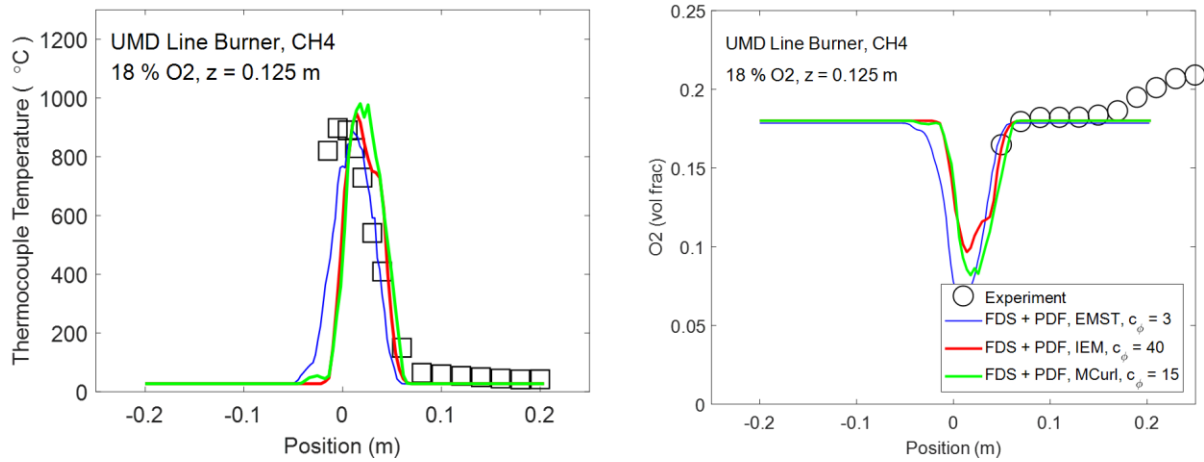


Figure 5.10. Calculated and measured experimental data of the time-averaged temperature (squared dots) and O₂ mole fraction (circled dots) above the fuel port; the oxidizer is the diluted air with 18% oxygen. The solid blue line represents the EMST model, the solid red line represents the IEM model, and the solid green line represents the modified Cur model.

5.4 Flame regime identification by using flame index

In the previous Section 5.3, it is found that the fire extinction limit is very sensitive to the different mixing models and mixing parameters. The level of sensitivity is even much higher than momentum-driven turbulent flames. From Figure 5.9, it is clearly shown that the EMST model has much better performance than the IEM model and Modified Curl model.

The EMST model can yield burning more easily and get much better combustion efficiency predictions. This kind of comparison suggests the importance of mixing modeling in fire simulations. In this section, the possible explanation for the performance difference between the EMST model, IEM model, and Modified Curl model will be proposed, and the definition of the flame index and flame regime will be discussed for the investigation.

From Equation (4.8), the model for the mixing frequency Ω has been developed, and this mixing model has been approved to perform pretty well for non-premixed turbulent combustion.

The non-premixed combustion is mainly controlled by large-scale turbulent eddies mixing. Thus a single conserved scalar can be used to parameterize the flame; usually, it can be represented by using the mixture fraction parameter. However, this model might encounter problems when dealing with turbulent premixed combustion phenomena. The premixed combustion is a propagation-driven flame. The coupling between turbulence and reaction wrinkles the flame front, thus enhancing mixing and making the premixed turbulent flame no longer a mixing-controlled flame but also be controlled by the reaction.

The performance difference between the IEM model, Modified Curl model, and the EMST model might be caused by non-premixed and premixed flames. The UMD line burner flame has a fuel jet that comes from the fuel port, and a co-flow oxidizer surrounds the fuel port, making it a typical non-premixed flame. However, the existing recirculation zone near the bottom of the flame may cause some local premixed regions; these can cause significant performance differences between different mixing models and make the IEM and Modified Curl model might not be suitable for the calculation.

Since the difference between the premixed and non-premixed flames can cause substantial performance differences between the mixing models, it is critical to identify a flame's combustion regime. One of the most effective and popular methods is called flame index or FI [93]. Yamashita et al. [93] first used this to investigate turbulent diffusion flames. The equation of flame index can be expressed as

$$FI = \frac{\nabla \tilde{Y}_O \cdot \nabla \tilde{Y}_F}{|\tilde{Y}_O| |\tilde{Y}_F| + \epsilon}, \quad (5.11)$$

where $\nabla \tilde{Y}_O$ represents the gradient of mass fractions of oxidizer, $\nabla \tilde{Y}_F$ is the gradient of mass fractions of fuel. The flame index is the dot product of the gradients normalized by the product of the magnitudes of the gradient. To prevent the denominator from being 0 in Equation (5.11), a very small value of ϵ will be added to Equation (5.11).

This equation can be used to identify the combustion regime in a flame. The normalized dot product of two vectors normalized by their magnitudes will have a value of +1 if these two vectors are pointing in the same direction. It will have a value of -1 if these two vectors point in opposite directions. As shown in Figure 5.11, the red solid vector represents the oxidizer gradient $\nabla \tilde{Y}_O$, and the solid purple vector represents the fuel gradient $\nabla \tilde{Y}_F$.

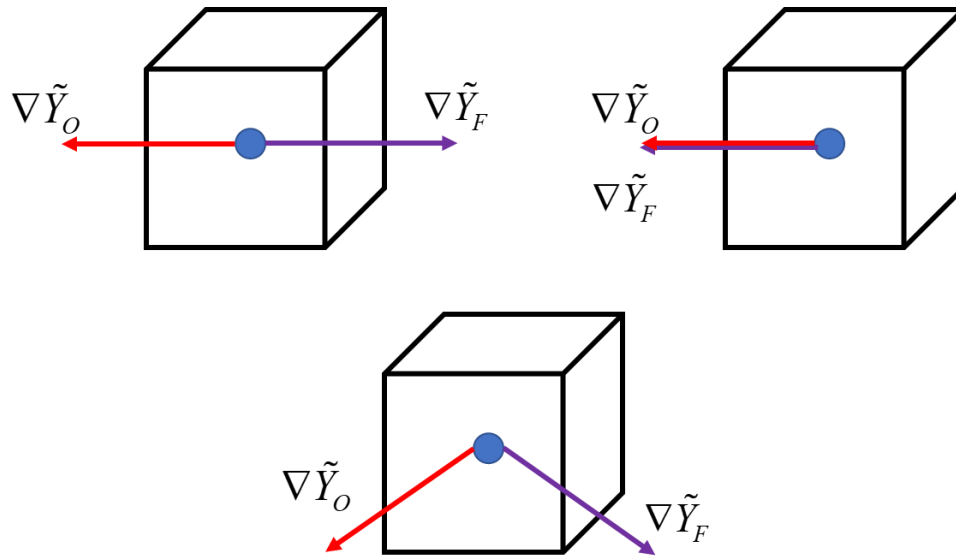


Figure 5.11. Schematic diagram of the flame index. The red solid vector represents the oxidizer gradient $\nabla \tilde{Y}_O$; the solid purple vector is the fuel gradient $\nabla \tilde{Y}_F$. The upper left plot shows the non-premixed mixing, the upper right plot demonstrates the premixed mixing, and the lower plot shows the partially premixed mixing phenomenon.

When these two vectors point in opposite directions, that means the fuel is on one side of the specific cell, and the oxidizer is on the other side of the cell, which is a typical non-premixed mixing phenomenon.

When these two vectors point in the same direction, that means the fuel and oxidizer are thoroughly mixed in this specific cell and make a premixed mixing phenomenon. The specific cell represents a partially premixed mixing phenomenon for other angles between these two vectors. The flame index can also be viewed as the cosine value of the angles between the two gradient vectors. The non-premixed mixing phenomenon has an angle of 180° , and the premixed mixing phenomenon will have an angle of 0° .

The definition of flame index shown in Equation (5.11) might encounter some problems when dealing with the PDF model. One typical issue is the possible false detection of the premixed region in a flame due to small gradient magnitudes. In Equation (5.11), when some region of the flame has tiny variations of mass fraction \tilde{Y}_O and \tilde{Y}_F , or has a minimal value of gradients

magnitude $\nabla \tilde{Y}_O$ and $\nabla \tilde{Y}_F$, the value of the flame index will be calculated as +1 even if the value of the dot product is relatively small.

A possible refinement of the flame index definition is to use a threshold to eliminate the region that contains the small value of gradients magnitudes and get a more accurate prediction of combustion regimes in a flame. For the region where the magnitudes of the two gradients $|\nabla \tilde{Y}_O|$ and $|\nabla \tilde{Y}_F|$ are smaller than a certain percentage of $\max(|\nabla \tilde{Y}_O|)$ and $\max(|\nabla \tilde{Y}_F|)$, the flame index value of this region will be set as 0 to eliminate the false prediction of premixed combustion, the Equation (5.11) can be modified as

$$FI = \begin{cases} 0 & (|\tilde{Y}_O| < \beta\%(\max|\tilde{Y}_O|), |\tilde{Y}_F| < \beta\%(\max|\tilde{Y}_F|)) \\ \frac{\nabla \tilde{Y}_O \cdot \tilde{Y}_F}{|\tilde{Y}_O| |\tilde{Y}_F|} & \end{cases}, \quad (5.12)$$

where $\beta\%$ is the threshold value, and $\beta=0.5$ has been approved as a suitable value for the prediction [94].

Table 5.1 and Figure 5.9 clearly show that the EMST model performs better than the IEM and Modified Curl model. Based on the above analysis, a possible explanation could be the existing premixed combustion near the bottom of the UMD fire burn causing the differences. The following part will provide a detailed investigation using the calculation data.

A UMD fire case mentioned in Section 5.2 will be used for detailed analysis. The fuel and the co-flow oxidizer's mass flow rates are the same as in the previous settings; the mass flow rate is 1.00 +/- 0.02 g/s for the methane fuel and 85 +/- 7 g/s for the diluted air with 18% oxygen. The fuel and oxidizers' temperatures are all set as 273 K.

Figure 5.12 presents the simultaneous contour plots of the CH4 flame. The temperature contour plot is shown on the upper left, the O2 mass fraction contour plot is shown on the upper right, the lower left contour plot represents the CH4 mass fraction, and the lower right is the flame index contour plot of the flame. These simultaneous contour plots are from the ignition stage for the CH4 flame, which is critical for fire extinction limit prediction of different mixing models and mixing parameters.

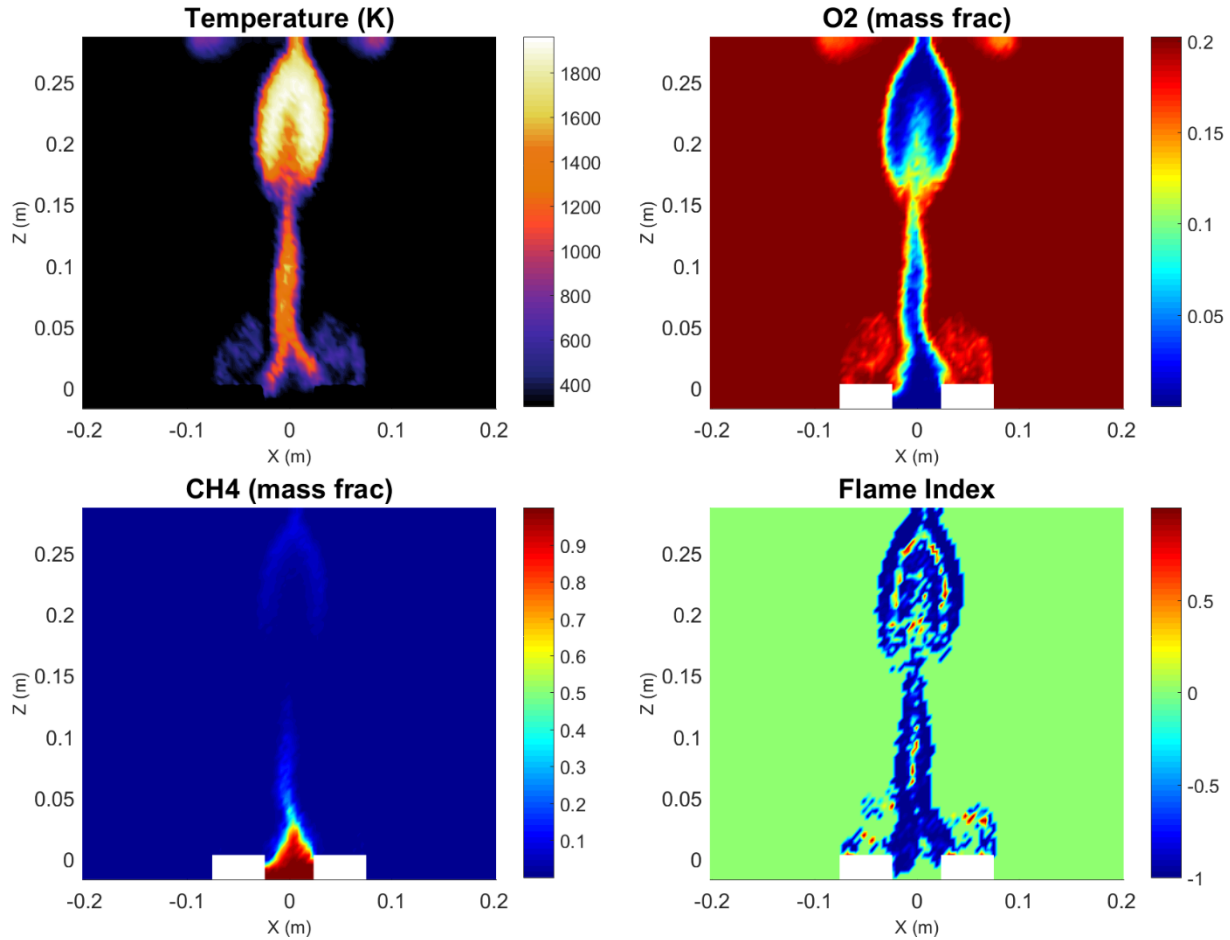


Figure 5.12. Simultaneous contour plot of CH₄ flame from the simulation; (upper left) temperature, (upper right) O₂ mass fraction, (lower left) CH₄ mass fraction, (lower right) flame index.

Figure 5.12 clearly shows that the fuel CH₄ is concentrated in the middle of the burner and surrounded by the oxidizer. From Equation (5.12) and Figure 5.11, it is known that the flame index values for the premixed combustion zone in the flame will be around +1. Thus the red region shown in the lower right contour plot of Figure 5.12 represents the possible premixed combustion zone. In contrast, the flame index values for non-premixed areas in the flame will be around -1, which means the blue region shown in the lower right contour plot of Figure 5.12 represents the non-premixed combustion zone.

The CH₄ flame of the UMD line burner is a typical non-premixed diffusion flame, which is why most of the flame area shown in the upper left contour plot of Figure 5.12 has blue color in the lower right contour plot of Figure 5.12. However, the small red-colored premixed combustion

areas shown in the lower right contour plot of Figure 5.12, at the bottom of the burner, near the ceramic fiberboard at the fuel outlet, attracted our interest. The premixed combustion zone located at the root of the flame is responsible for the performance differences between different mixing models and parameters. These tiny premixed combustion areas make it impossible for the flame to attach well to the ceramic fiberboard, making it easy for the flame to liftoff and extinction in the ignition phase. Figure 5.13 clearly shows one of the interesting zones that contain the value of flame index around +1, and its corresponding oxidizer gradient $\nabla \tilde{Y}_O$, and fuel gradient $\nabla \tilde{Y}_F$ are shown in Figure 5.14.

Interesting zone of flame index contour plot

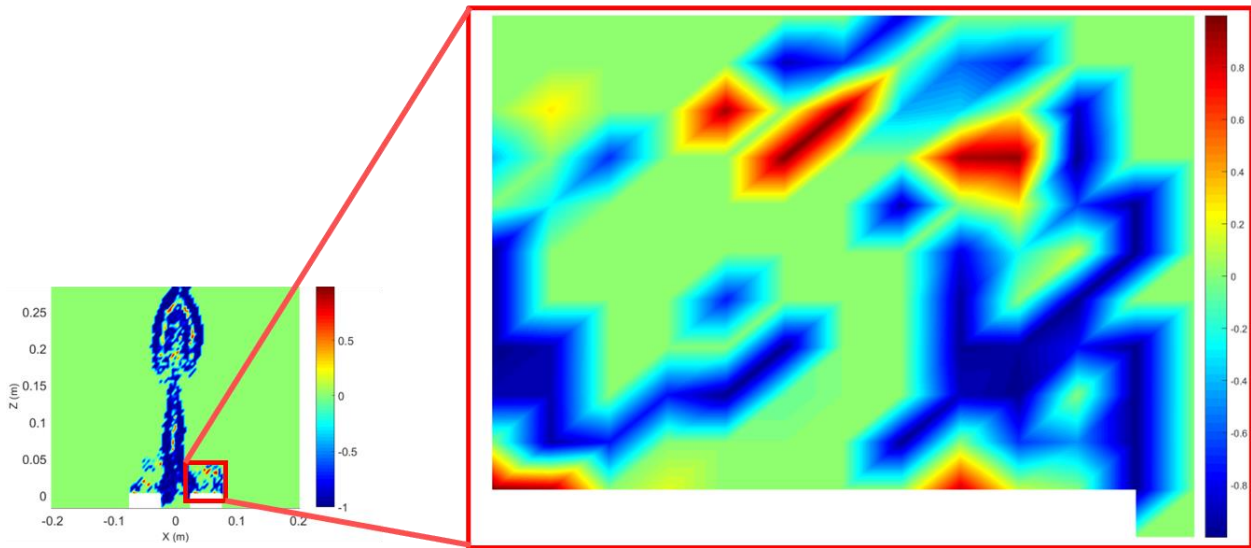


Figure 5.13. Interesting zone of flame index contour plot.

More detailed plots have been made in Figure 5.14; the upper contour plot is the mass fraction of CH₄ and the fuel gradient $\nabla \tilde{Y}_F$, the middle contour plot is the mass fraction of O₂ and the oxidizer gradient $\nabla \tilde{Y}_O$, and the lower plot is the flame index with fuel and oxidizer gradients.

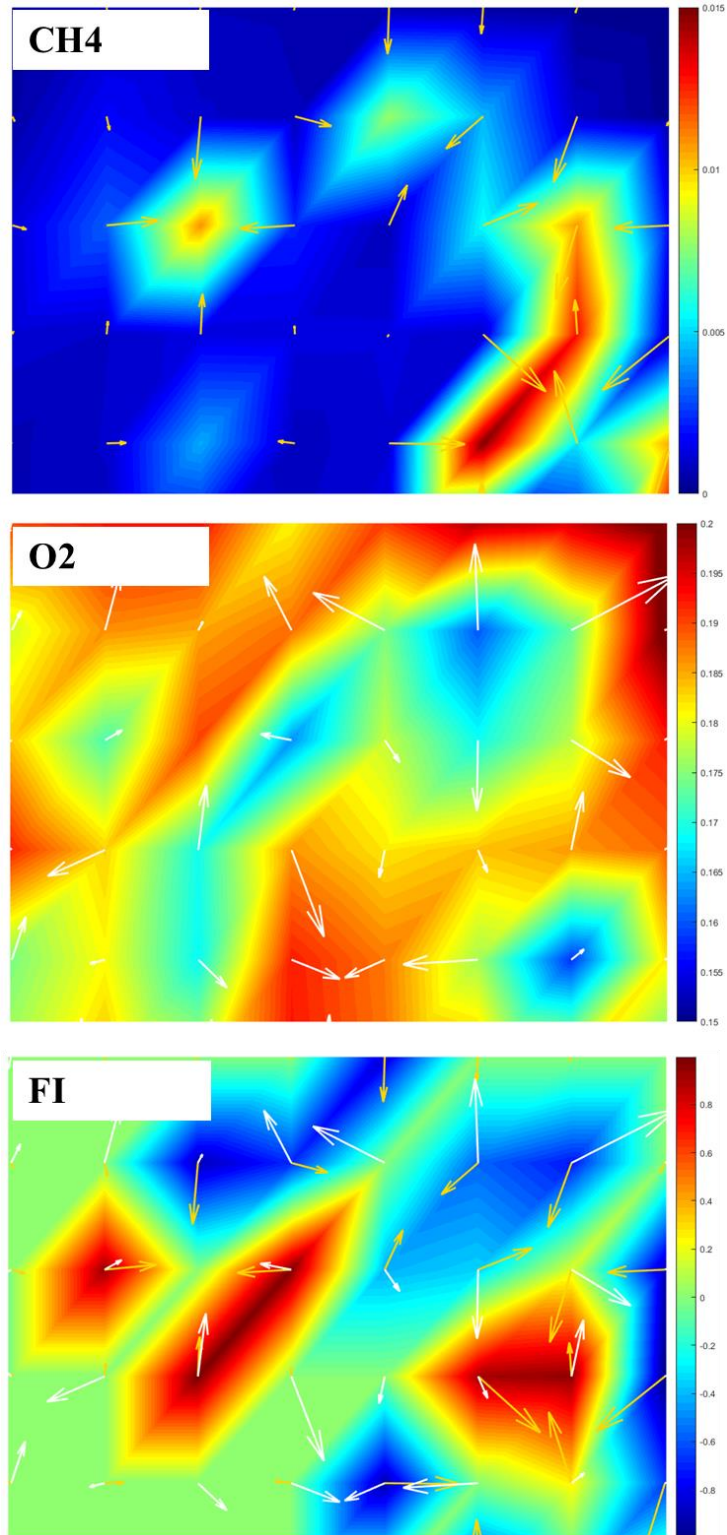


Figure 5.14. Contour plot of the interesting zone; (upper) mass fraction of CH₄ and the yellow line fuel gradient, (middle) mass fraction of O₂ and the white line oxidizer gradient, (lower) flame index, and both gradients.

It can be clearly seen from Figure 5.14 that the fuel and oxidant enrichment zones located in the upper left and lower right corners form a clear premixing zone. The gradients of the fuel and oxidizer point almost in the same direction, thus giving a value of +1 for the calculated flame index. These tiny areas of premixed flame are enriched in the root of the flame, resulting in different predictions of flame extinction limits by different mixing models and mixing parameters.

5.5 Summary

This chapter uses a methane flame generated by the UMD burner for the investigations. A quantitative comparison between the experiment and simulation temperatures and the mole fractions of O₂ are used to validate the original FDS code and the coupled FDS-HPDF model. The heat release rate and combustion efficiency have been calculated using different mixing models and parameters for predicting the flame extinction limits. It is found that the EMST model can easily yield burning flames, and its results can match the measured η_{comb} pretty well. The IEM and Modified Curl models could not yield a burning flame without a relatively large value of C_ϕ , and their results significantly underpredict the combustion efficiency η_{comb} . The concept of the flame index has been used to find a possible explanation for the performance differences between these models; the tiny areas of premixed flame that are enriched in the root of the flame may cause these differences. Since the fire extinction limit is very sensitive to the different mixing models and mixing parameters, the choice of mixing modeling in fire simulations is very critical. The existing mixing models need further enhancement to predict fire extinction.

6. CONCLUSION AND FUTURE WORK

In this dissertation, we focus on the combustion modeling of diffusion flames. Two different types of diffusion flames have been analyzed: the momentum-dominant jet flames and buoyancy-controlled pool fires.

For the studies of momentum-dominant jet flames, modeling differential molecular diffusion in turbulent non-premixed combustion remains a significant challenge for the flamelet models. The laminar flamelet is a key component of a flamelet model for turbulent combustion. However, the representativity of the laminar flamelet for the characteristics of differential molecular diffusion in turbulent combustion problems is still a significant challenge that has not been well addressed.

For the investigation of buoyancy-controlled pool fires, previous investigations used highly simplified chemical mechanisms or low-order turbulence and combustion models to do the analysis. Using a high ordering model to perform detailed investigations of the flame instabilities and capturing accurate predictions of extinction limits is critically important for developing predictive capabilities for fire.

The main work in this dissertation is centered on filling the gap between the existing knowledge of differential molecular diffusion in turbulent combustion and the practical applications, focusing on developing and enhancing accurate and effective flame extinction limits predictive models. The major conclusions and contributions are summarized as follows.

In Chapter 2, we first compare the differences between the calculation results considering and neglecting the differential molecular diffusion effect. We found that assuming equal molecular diffusivity or unit Lewis number is highly questionable and might cause inaccurate calculation results. Then we studied the two conceptual burner configurations, the opposed jet burner and the Tsuji burner, which were the classic tools for generating the laminar flamelets. These two burners are commonly viewed to be equivalent for the description of laminar flamelet structures. However, we first found their differences when using these burners to represent differential molecular diffusion. The traditionally opposed jet burner yields an almost fixed equal diffusion location in the mixture fraction space for the transport of different elements. The Tsuji burner can produce a continuous variation of the equal diffusion location in the mixture fraction space with a slight extension. Thus we think a single parameter strain rate cannot fully parameterize steady laminar

flamelet as previously thought; the second parameter, such as the velocity ratio between the fuel and oxidizer stream, is needed. We used the traditional unconstrained opposed jet burner to investigate further and found that a modification to the opposed jet burner can produce the desired result. The constrained opposed jet mixing layer successfully replicates the trend observed in the Tsuji burner case and hence provides a plausible explanation for the differences observed between these two burners.

In Chapter 3, the representativity of laminar flamelet is examined in practically relevant flows and flames. The Tsuji burner was found that has a significant advantage that can have a variation of the equal diffusion location. We proved that is an essential characteristic of turbulent non-premixed combustion by using a laminar jet mixing layer problem, a turbulent jet mixing layer problem, and a turbulent jet non-premixed flame. Thus we believe that the Tsuji burner is potentially a more suitable choice than the opposed jet burner for laminar flamelet generation that can be consequently used in flamelet modeling of differential molecular diffusion in turbulent non-premixed combustion. Additional considerations like the effect of unsteadiness and extinction are also found to be needed to accompany the Tsuji burner to produce a representative flamelet for the effect of DMD in the turbulent jet flame. These findings are essential to developing flamelet models that predict DMD in turbulent non-premixed flames.

In Chapter 4 and Chapter 5, we discovered the method that combines the NIST Fire Dynamics Simulator (FDS) code of LES and our in-house PDF code, HPDF. By doing this kind of combination, we can fully take advantage of the PDF model. The transported PDF model is a high ordering model and is suitable to solve the problems, especially for considering detailed chemical reactions and resolving chemical composition in reacting flows. We adopted the University of Maryland line burner as validation for testing the coupled FDS-HPDF model. After verifying the model's accuracy using quantitative comparisons, it has been used to investigate different mixing models and parameters.

The combustion efficiency and fire extinction limits have been used to test the performance of the IEM, Modified Curl, and EMST models. The EMST model can yield burning flames without difficulty and perfectly match the measured combustion efficiency. The IEM model and Modified Curl model need a high value of C_ϕ to yield burning and constantly underpredict the combustion efficiency. Finally, we applied the concept of the flame index. We found that many tiny areas of the premixed region are enriched in the flame's root, which could be the main reason behind the

mixing models' performance differences. During our studies of the fire case, it is found that the fire extinction limit is very sensitive to the different mixing models and mixing parameters. The level of sensitivity is higher than momentum-driven turbulent flames. That suggests the importance of mixing modeling in fire simulations. The existing mixing models need further enhancement for predicting fire extinction.

For combustion research, our consistent goal has been to enhance the understanding of combustion physics and, based on this, to improve and develop more accurate computational methods that can be applied to the prediction of actual combustion. There are some outstanding achievements in this dissertation for combustion research. At the same time, we need longer-term efforts. Based on the current dissertation work, we believe the following potential directions can be explored in-depth.

For the studies on the representative of differential molecular diffusion, we found that a single parameter strain rate cannot fully parameterize steady laminar flamelet, and we chose to use velocity ratio as a second parameter. Based on our knowledge, it is better to define a momentum ratio rather than using a velocity ratio. The critical challenge is finding a proper momentum ratio definition based on the Tsuji burner's physical structure. The other directions that could be studied include generating a flamelet table based on the current finding and testing that in practically relevant flows and flames.

We are currently using the coupled FDS-HPDF model for the studies on developing predictive capabilities for fire. Only the flame extinction limits and combustion efficiency have been used for modeling studies. Many more experimental data and fields can be used to study, such as the effects of radiation and flame local instabilities. More detailed particle analysis can be applied to the computational results, providing better support for understanding the physical combustion model and improving the model's predictive power.

REFERENCES

- [1] Renewables 2020 Global Status Report, <https://www.ren21.net/reports/global-status-report>, accessed 11/2020.
- [2] Kumar, C., KR, A. K., & Tripathi, A. A Unified 3D CFD Model for Jet and Pool Fires.
- [3] Pedersen, N. (2012). Modeling of jet and pool fires and validation of the fire model in the CFD code FLACS (Master's thesis, The University of Bergen).
- [4] <http://www.hrdp-idrm.in/e5783/e17327/e27015/e27713/>
- [5] Hamins, A., Kashiwagi, T., & Buch, R. R. (1996). Characteristics of pool fire burning. ASTM special technical publication, 1284, 15-41.
- [6] McCaffrey, B. J., & Flames, P. B. D. (1979). Some Experimental Results. Nbsir.
- [7] S.B. Pope. Turbulent Flows. UK: Cambridge University Press, August 2000
- [8] Williams, F. A. (1975). Recent advances in theoretical descriptions of turbulent diffusion flames. Turbulent mixing in nonreactive and reactive flows (pp. 189–208). Springer, Boston, MA.
- [9] Peters, N. (1983). Local quenching due to flame stretch and non-premixed turbulent combustion. Combustion Science and Technology, 30(1–6), 1–17.
- [10] N. Peters. Laminar diffusion flamelet models in non-premixed turbulent combustion. Progress in energy and combustion science, 10(3):319–339, 1984.
- [11] C.D. Pierce and P. Moin. Progress-variable approach for large-eddy simulation of non-premixed turbulent combustion. Journal of Fluid Mechanics, 504:73–97, 2004.
- [12] Haworth, D. C., & Pope, S. B. (2011). Transported probability density function methods for Reynolds-averaged and large-eddy simulations. In Turbulent combustion modeling (pp. 119-142). Springer, Dordrecht.
- [13] Wang, H., Juddoo, M., Starner, S. H., Masri, A. R., and Pope, S. B., “A novel transient turbulent jet flame for studying turbulent combustion,” Proceedings of the Combustion Institute, Vol. 34, No. 1, 2013, pp. 1251–1259.

- [14] Anand, M. S., & Pope, S. B. (1985). Diffusion behind a line source in grid turbulence. In *Turbulent Shear Flows 4* (pp. 46-61). Springer, Berlin, Heidelberg.
- [15] McDermott, R., & Pope, S. B. (2007). A particle formulation for treating differential diffusion in filtered density function methods. *Journal of Computational Physics*, 226(1), 947-993.
- [16] Zhang, P., & Wang, H. (2018). Variance consistent mean shift particle model for treating differential molecular diffusion in transported PDF methods for turbulent reactive flows. *Computers & Fluids*, 170, 53-76.
- [17] Pitsch, H., and N. Peters. "A consistent flamelet formulation for non-premixed combustion considering differential diffusion effects." *Combustion and flame* 114.1-2 (1998): 26-40.
- [18] Wang, H. (2016). Consistent flamelet modeling of differential molecular diffusion for turbulent non-premixed flames. *Physics of Fluids*, 28(3), 035102.
- [19] M. Ihme, H. Pitsch, Prediction of extinction and reignition in nonpremixed turbulent flames using a flamelet/progress variable model: 2. Application in LES of Sandia Flames D and E, *Combust. Flame* 155 (1) (2008b) 90–107, doi:10.1016/j.combustflame.2008.04.015
- [20] Ma, M. C., & Devaud, C. B. (2015). A Conditional Moment Closure (CMC) formulation including differential diffusion applied to a non-premixed hydrogen–air flame. *Combustion and Flame*, 162(1), 144-158.
- [21] Cuenot, B., & Poinso, T. (1994, January). Effects of curvature and unsteadiness in diffusion flames. Implications for turbulent diffusion combustion. In *Symposium (International) on Combustion* (Vol. 25, No. 1, pp. 1383-1390). Elsevier.
- [22] Bray, K.N.C. and Peters, N., Laminar flamelets in turbulent flames. In: Libby, P.A. and Williams, F.A. (eds), *Turbulent Reacting Flows*. Academic Press, London (1994) Chapter 2, pp. 63–113.
- [23] Tsuji, H. (1982). Counterflow diffusion flames. *Progress in energy and combustion science*, 8(2), 93-119.
- [24] Gokulakrishnan, Ponnuthurai, et al. "LES-PDF Modeling of Flame Instability and Blow-Out in Bluff-Body Stabilized Flames." 45th AIAA/ASME/SAE/ASEE Joint Propulsion Conference & Exhibit. 2009.

- [25] Smithells, A., & Ingle, H. (1892). XV.—The structure and chemistry of flames. *Journal of the Chemical Society, Transactions*, 61, 204-216.
- [26] Markstein, G. H. "Experimental studies of flame-front instability." *AGARDograph*. Vol. 75. Elsevier, 1964. 75-105.
- [27] Ishizuka, S., K. Miyasaka, and C. K. Law. "Effects of heat loss, preferential diffusion, and flame stretch on flame-front instability and extinction of propane/air mixtures." *Combustion and Flame* 45 (1982): 293-308.
- [28] Yule, AJ, Chigier, NA, Ralph, S., Boulderstone, R., and Ventura, J., *A/AA J.* 19:752 (1981)
- [29] Roquemore, W. M., et al. "The structure of jet diffusion flames." *Turbulent Reactive Flows*. Springer, New York, NY, 1989. 49-63.
- [30] Davis, R. W., et al. "Preliminary results of a numerical-experimental study of the dynamic structure of a buoyant jet diffusion flame." *Combustion and Flame* 83.3-4 (1991): 263-270.
- [31] Durao, DF and Whitelaw, J. H, "Instantaneous Velocity and Temperature Measurements in Oscillating Diffusion Flames", *Proc. R. Soc. Lond. A.*, 338,479-501, 1975
- [32] Katta, V. R., and W. M. Roquemore. "Role of inner and outer structures in transitional jet diffusion flame." *Combustion and Flame* 92.3 (1993): 274-282.
- [33] Shin, D. S., and J. H. Ferziger. "Linear stability of the reacting mixing layer." *AIAA journal* 29.10 (1991): 1634-1642.
- [34] Day, M. J., W. C. Reynolds, and N. N. Mansour. "The structure of the compressible reacting mixing layer: Insights from linear stability analysis." *Physics of Fluids* 10.4 (1998): 993-1007.
- [35] See, Yee Chee, and Matthias Ihme. "Effects of finite-rate chemistry and detailed transport on the instability of jet diffusion flames." *Journal of Fluid Mechanics* 745 (2014): 647-681.
- [36] Berlad, A. L., and C. H. Yang. "A theory of flame extinction limits." *Combustion and Flame* 4 (1960): 325-333.
- [37] Jarosinski, Jozef. "A survey of recent studies on flame extinction." *Progress in Energy and Combustion Science* 12.2 (1986): 81-116.

- [38] Kee, Robert J., et al. "A computational model of the structure and extinction of strained, opposed flow, premixed methane-air flames." Symposium (International) on Combustion. Vol. 22. No. 1. Elsevier, 1989.
- [39] Sun, Wenting, et al. "Kinetic effects of non-equilibrium plasma-assisted methane oxidation on diffusion flame extinction limits." *Combustion and Flame* 159.1 (2012): 221-229.
- [40] Mark, L., and F. R. Thomas. "DEVELOPMENT OF A STANDARD CUP-BURNER APPARATUS: NFPA AND ISO STANDARD METHODS." Halon Options Technical Working Conference. 1999.
- [41] Takahashi, Fumiaki, Gregory T. Linteris, and Viswanath R. Katta. "Extinguishment of methane diffusion flames by carbon dioxide in coflow air and oxygen-enriched microgravity environments." *Combustion and Flame* 155.1-2 (2008): 37-53.
- [42] Dennis, C. N., Satija, A., & Lucht, R. P. (2016). High dynamic range thermometry at 5 kHz in hydrogen–air diffusion flame using chirped-probe-pulse femtosecond coherent anti-stokes Raman scattering. *Journal of Raman Spectroscopy*, 47(2), 177-188.
- [43] Hilbert, R., & Thévenin, D. (2004). Influence of differential diffusion on maximum flame temperature in turbulent nonpremixed hydrogen/air flames. *Combustion and flame*, 138(1-2), 175-187.
- [44] Kee, R. J., M. E. Coltrin, and P. Glarborg. "Chemically Reacting Flow: Theory & Practice, 596 John Wiley & Sons." Inc., Hoboken, 597 (2003).
- [45] Tsuji, Hiroshi, and Ichiro Yamaoka. "The structure of counterflow diffusion flames in the forward stagnation region of a porous cylinder." Symposium (International) on Combustion. Vol. 12. No. 1. Elsevier, 1969.
- [46] Ansys fluent user's guide (version: 2020r1) (2021).
URL <https://www.ansys.com/products/fluids/ansys-fluent>
- [47] Frouzakis, Christos E., et al. "From diffusion to premixed flames in an H₂/air opposed-jet burner: the role of edge flames." *Combustion and Flame* 130.3 (2002): 171-184.
- [48] Ciani, A., et al. "Experimental investigation of the morphology and stability of diffusion and edge flames in an opposed jet burner." *Combustion and Flame* 150.3 (2007): 188-200.

- [49] Lutz, A. E., Kee, R. J., Grcar, J. F., & Rupley, F. M. (1997). OPPDIF: A Fortran program for computing opposed-flow diffusion flames (No. SAND-96-8243). Sandia National Labs., Livermore, CA (United States).
- [50] Smith, L. L., Dibble, R. W., Talbot, L., Barlow, R. S., & Carter, C. D. (1995). Laser Raman scattering measurements of differential molecular diffusion in nonreacting turbulent jets of H₂/CO₂ mixing with air. *Physics of Fluids*, 7(6), 1455-1466.
- [51] Smith, L. L., Dibble, R. W., Talbot, L., Barlow, R. S., & Carter, C. D. (1995). Laser Raman scattering measurements of differential molecular diffusion in turbulent nonpremixed jet flames of H₂CO₂ fuel. *Combustion and flame*, 100(1-2), 153-160.
- [52] Gregory P. Smith, David M. Golden, Michael Frenklach, Nigel W. Moriarty, Boris Eiteneer, Mikhail Goldenberg, C. Thomas Bowman, Ronald K. Hanson, Soonho Song, William C. Gardiner, Jr., Vitali V. Lissianski, and Zhiwei Qin http://www.me.berkeley.edu/gri_mech/.
- [53] Chelliah, H. K., et al. "An experimental and theoretical investigation of the dilution, pressure and flow-field effects on the extinction condition of methane-air-nitrogen diffusion flames." *Symposium (International) on Combustion*. Vol. 23. No. 1. Elsevier, 1991.
- [54] Millington, R. J. "Gas diffusion in porous media." *Science* 130.3367 (1959): 100-102.
- [55] Saxena, S. K., et al. "Effect of pore size on diffusion coefficients in porous media." *Soil Science* 117.2 (1974): 80-86.
- [56] Van Brakel, Jaap, and P. M. Heertjes. "Analysis of diffusion in macroporous media in terms of a porosity, a tortuosity and a constrictivity factor." *International Journal of Heat and Mass Transfer* 17.9 (1974): 1093-1103.
- [57] Bilger, R. W. "The structure of turbulent nonpremixed flames." *Symposium (International) on Combustion*. Vol. 22. No. 1. Elsevier, 1989.
- [58] Han, Chao, and Haifeng Wang. "Reynolds-number power-law scaling of differential molecular diffusion in turbulent nonpremixed combustion." *Physical Review Fluids* 3.10 (2018): 103201.

- [59] Han, Chao, and Haifeng Wang. "Effect of Unsteadiness and Scalar Dissipation Models on Flamelet Modeling of Differential Molecular Diffusion in Turbulent Non-Premixed DNS Flames." *Flow, Turbulence and Combustion* 108.4 (2022): 1017-1042.
- [60] Haifeng, Wang. (2010). Numerically Accurate Rans/Pdf And Les/Pdf Calculations Of Turbulent Flames (PhD). Cornell University.
- [61] M. Germano, U. Piomelli, P. Moin, and W.H. Cabot. A dynamic subgrid-scale eddy viscosity model. *Physics of Fluids A: Fluid Dynamics* (1989-1993),3(7):1760–1765, 1991.
- [62] C.K. Lu, T. and Law. Toward accommodating realistic fuel chemistry in large-scale computations. *Progress in Energy and Combustion Science*, 35(2):192–215,2009.
- [63] S. B. Pope, "Self-conditioned fields for large-eddy simulations of turbulent flows," *Journal of Fluid Mechanics*, vol. 652, pp. 139–169, 2010.
- [64] Pei, Zhang. (2019). Large eddy simulation/transported probability density function modeling of turbulent combustion: model advancement and applications (PhD). Purdue University.
- [65] Villermaux, J., & Devillon, J. C. (1972, May). Représentation de la coalescence et de la redispersion des domaines de ségrégation dans un fluide par un modèle d'interaction phénoménologique. In *Proceedings of the 2nd International symposium on chemical reaction engineering* (Vol. 26, pp. 1-13). Elsevier New York.
- [66] J. Janicka, W. Kolbe, W. Kollmann, Closure of the transport-equation for the probability density function of turbulent scalar fields, *J. Non-Equil. Thermodynam.* 4 (1979) 47-66.
- [67] S. Subramaniam, S.B. Pope, A mixing model for turbulent reactive flows based on Euclidean minimum spanning trees, *Combust. Flame* 115 (1998) 487-514.
- [68] S. B. Pope, "PDF methods for turbulent reactive flows," *Progress in Energy and Combustion Science*, vol. 11, no. 2, pp. 119–192, 1985.
- [69] Barlow, R. S., and J. H. Frank. "Effects of turbulence on species mass fractions in methane/air jet flames." *Symposium (International) on Combustion*. Vol. 27. No. 1. Elsevier, 1998.
- [70] Flagan, Richard C., and John P. Appleton. "A stochastic model of turbulent mixing with chemical reaction: Nitric oxide formation in a plug-flow burner." *Combustion and Flame* 23.2 (1974): 249-267.

- [71] Villermaux, J., and J. C. Devillon. "Représentation de la coalescence et de la redispersion des domaines de ségrégation dans un fluide par un modèle d'interaction phénoménologique." Proceedings of the 2nd International symposium on chemical reaction engineering. Vol. 26. Elsevier New York, 1972.
- [72] Cao, Renfeng Richard, Haifeng Wang, and Stephen B. Pope. "The effect of mixing models in PDF calculations of piloted jet flames." Proceedings of the combustion institute 31.1 (2007): 1543-1550.
- [73] Curl, Rane L. "Dispersed phase mixing: I. Theory and effects in simple reactors." AIChE journal 9.2 (1963): 175-181.
- [74] Janicka, J., W. Kolbe, and W. Kollmann. "Closure of the transport equation for the probability density function of turbulent scalar fields." (1979): 47-66.
- [75] Subramaniam, S., and S. B. Pope. "A mixing model for turbulent reactive flows based on Euclidean minimum spanning trees." Combustion and Flame 115.4 (1998): 487-514.
- [76] McGrattan, K. B. (2005). Fire dynamics simulator (version 4). Technical reference guide. NIST special publication 1018.
- [77] Fire Dynamics Simulator (FDS) and Smokeview (SMV), <https://pages.nist.gov/fds-smv/>, accessed 11/2020.
- [78] NUREG-1824, 2007. Verification & Validation of Selected Fire Models for Nuclear Power Plant Applications. U.S. Nuclear Regulatory Commission.
- [79] Muradoglu, M., Pope, S. B., & Caughey, D. A. (2001). The hybrid method for the PDF equations of turbulent reactive flows: consistency conditions and correction algorithms. Journal of Computational Physics, 172(2), 841-878.
- [80] Andrews, J. R., & Biblarz, O. (1981). Temperature dependence of gas properties in polynomial form. Monterey, California. Naval Postgraduate School.
- [81] McBride, B. J., Gordon, S., & Reno, M. A. (1993). NASA technical memorandum 4513-coefficients for calculating thermodynamic and transport properties of individual species. National Aeronautics and Space Administration.

- [82] Bird, R. B., Stewart, W. E., Lightfoot, E. N., & Klingenberg, D. J. (2015). Introductory transport phenomena. Wiley Global Education.
- [83] McBride, B. J. (2002). NASA Glenn coefficients for calculating thermodynamic properties of individual species. National Aeronautics and Space Administration, John H. Glenn Research Center at Lewis Field.
- [84] J. P. White, E. D. Link, A. C. Trouve, P. B. Sunderland, A. W. Marshall, J. A. Sheffel, M. L. Corn, M. B. Colket, M. Chaos, H. Z. Yu, Radiative emissions measurements from a buoyant, turbulent line flame under oxidizer-dilution quenching conditions, *Fire Safety Journal* 76 (2015) pp. 74-84.
- [85] J. P. White, E. D. Link, A. C. Trouve, P. B. Sunderland, A. W. Marshall, A general calorimetry framework for measurement of combustion efficiency in a suppressed turbulent line fire, *Fire Safety Journal* (2016).
- [86] J.P. White, S. Verma, E. Keller, A. Hao, A. Trouvé, A.W. Marshall, Water mist suppression of a turbulent line fire, *Fire Safety Journal* 91:705-713, 2017.
- [87] J.P. White, Measurement and simulation of suppression effects in a buoyant turbulent line fire, Ph.D. thesis, University of Maryland, College Park, 2016.
- [88] A. Kazakov and M. Frenklach, <http://www.me.berkeley.edu/drm/>
- [89] M. Frenklach, H. Wang, C.-L. Yu, M. Goldenberg, C.T. Bowman, R.K. Hanson, D.F. Davidson, E.J. Chang, G.P. Smith, D.M. Golden, W.C. Gardiner and V. Lissianski, http://www.me.berkeley.edu/gri_mech/; and Gas Research Institute Topical Report: M. Frenklach, H. Wang, M. Goldenberg, G.P. Smith, D.M. Golden, C.T. Bowman, R.K. Hanson, W.C. Gardiner and V. Lissianski, 'GRI-Mech---An Optimized Detailed Chemical Reaction Mechanism for Methane Combustion,' Report No. GRI-95/0058, November 1, 1995.
- [90] Vilfayeau, S., White, J. P., Sunderland, P. B., Marshall, A. W., & Trouvé, A. (2016). Large eddy simulation of flame extinction in a turbulent line fire exposed to air-nitrogen co-flow. *Fire Safety Journal*, 86, 16-31.

- [91] Willard, John J., and Richard E. Wondra. "Quantitative evaluation of flame-retardant cotton finishes by the limiting-oxygen index (LOI) technique." *Textile Research Journal* 40.3 (1970): 203-210.
- [92] Senecal, Joseph A. "Flame extinguishing in the cup-burner by inert gases." *Fire Safety Journal* 40.6 (2005): 579-591.
- [93] Yamashita, H., M. Shimada, and T. Takeno. "A numerical study on flame stability at the transition point of jet diffusion flames." *Symposium (International) on Combustion*. Vol. 26. No. 1. Elsevier, 1996.
- [94] Kashyap, Shashank Satyanarayana. *Multi-regime Turbulent Combustion Modeling using Large Eddy Simulation/Probability Density Function*. Diss. Purdue University Graduate School, 2019.